5-2017

Morphological and Photoelectrochemical Characterization of Membrane Reconstituted Photosystem I (PSI)

Seyedeh Hanieh Niroomand
University of Tennessee, Knoxville, snirooma@vols.utk.edu

To the Graduate Council:

I am submitting herewith a dissertation written by Seyedeh Hanieh Niroomand entitled "Morphological and Photoelectrochemical Characterization of Membrane Reconstituted Photosystem I (PSI)." I have examined the final electronic copy of this dissertation for form and content and recommend that it be accepted in partial fulfillment of the requirements for the degree of Doctor of Philosophy, with a major in Chemical Engineering.

Bamin Khomami, Major Professor

We have read this dissertation and recommend its acceptance:

Dibyendu Mukherjee, Pat Collier, Paul Frymier

Accepted for the Council:

Dixie L. Thompson

Vice Provost and Dean of the Graduate School

(Original signatures are on file with official student records.)

Morphological and Photoelectrochemical Characterization of Membrane Reconstituted Photosystem I (PSI)

A Dissertation Presented for the

Doctor of Philosophy

Degree

The University of Tennessee, Knoxville

Seyedeh Hanieh Niroomand

May 2017

DEDICATION

This thesis is dedicated to my wonderful family.

To the loving memory of my parents, who left fingerprints of grace on my life and shall not be forgotten. To my grandparents, who raised me, taught me unconditional love and supported me in all my endeavors. To khalejoon Fatemeh, who taught me to be kind yet strong, courageous and ambitious. To my uncles, who have been my brothers, friends and heroes. To my sister, Hoorieh, whose love embraces me everywhere regardless of the distance between us. To my cousins, who make life fun and to my best friend, Majid, who supported me at each step of this dissertation with his encouragement.

ACKNOWLEDGEMENTS

ABSTRACT

The robust structural and photoactive electrochemical properties of Photosystem I (PSI), a transmembrane photosynthetic protein complex, make it an ideal candidate for incorporation into solid state bioelectronic or hybrid photovoltaic devices. However, the first step towards the successful fabrication of such devices requires systematic assembly of oriented and functional PSI onto desired bio-abio interfaces via suitable protein scaffoldings. Hence, this dissertation focuses on utilizing the cyanobacterial PSI for integration into organic/inorganic interfaces that mediate photo-electrochemical energy conversions for electricity and/or solar fuel production. To this end, in this study the effect of systematic incorporation of PSI complexes into synthetic membrane-bound structures that mimic the natural thylakoid membrane housing of PSI quantifies via its performance and photocurrent response is demonstrated. Therefore, the surfactant-induced membrane solubilization of three phospholipids, namely DPhPC (1,2-diphytanoyl-sn-glycero-3-phosphocholine), DPPG (1,2-dipalmitoyl-sn-glycero-3-phospho-(1'-rac-glycerol)), and DPhPG (1,2-diphytanoyl-sn-glycero-3-phospho-(1'-rac-glycerol)) with the motivation of creating biomimetic reconstructs of PSI reconstitution in these liposomes are studied via isothermal titration calorimetry, turbidity measurements, dynamic light scattering and cryo-transmission electron microscopy imaging. The results indicate the typical three-stage solubilization process during lamellar-to-micellar transitions for liposomes is dictated by the critical detergent/phospholipid ratios. Considering that most successful protein incorporation occurs during the second stage of solublization, these studies set the backdrop for ideal concentration ratios for successful protein insertion in this stage. Furthermore, a facile yet elegant method for incorporation of PSI trimeric complexes into DPhPG bilayer membranes is introduced. The efficacy of this method is demonstrated via absorption and fluorescence spectroscopy measurements as well as direct visualization using atomic force microscopy. This study also provides direct evidence that PSI confinements in synthetic lipid scaffolds can be used for tuning the photoexcitation characteristics of PSI. Finally, detailed chronoamperometry measurements were conducted on PSI-proteoliposomes made from PSI incorporated within biomimetic membrane scaffolds and supported on suitable SAM substrates to investigate the enhancement in photocurrent responses arising from such confinement. The significant observation here is that the photo currents generated from PSI complexes under liposome confinements produce photocurrents

four times higher than that produced from dense monolayer of individual PSI on SAM substrates using an equivalent concentration of PSI.

TABLE OF CONTENTS

LIST OF TABLES

LIST OF FIGURES

CHAPTER 1

INTRODUCTION

Oxygenic photosynthesis in plants, algae and cyanobacteria have evolved over billions of years to capture and harvest solar energy in the form of chemical energy with nearly 100% quantum efficiency.[1] This energy storage in the form of carbohydrates for photosynthetic organisms has enabled the evolution of aerobic life forms on earth since the beginning of life. In turn, the carbohydrates from these organisms has become the source of earth's fossil fuel reserves. But, the ever-increasing global consumption of fossil fuels (oil, coal and natural gas) by most industrialized and developing countries have placed a tremendous demand on the access to these reserves that has taken a toll on nature and the environment. Firstly, access to these natural resources is limited and non-renewable, and secondly, the burning of fossil fuels has resulted in excess of CO_2 production that has been increasingly attributed to the imbalance in atmospheric carbon fixation processes and thereby, believed to be contributing to global warming, climate change and environmental pollution. Thus, the quest for renewable green energy has sparked considerable interest in Photosystem I (PSI), the photosynthetic protein complex, that is akin to a nano-scale biological photodiode and enables light-activated charge separation to facilitate unidirectional electron flow.[1]

This dissertation focuses on utilizing the cyanobacterial PSI from Thermosynechocoocus Elongatus for integration into organic/inorganic interfaces in bio-hybrid devices that mediate photo-electrochemical energy conversions for electricity and/or solar fuel production.

This introductory chapter illustrates the photosynthesis process from a functional point of view and in particular the structures associated with cyanobacterial photosynthetic membrane proteins, the function of thylakoid membrane and photactivated properties of PSI. Finally, the research efforts that inspired the work presented in this dissertation and the techniques employed to investigate the PSI functionality in solution and on self-assembled monolayer (SAM) surfaces is discussed.

1.1 PHOTOSYNTHESIS FROM A FUNCTIONAL POINT OF VIEW

Photosynthesis is the fundamental biological process through which light energy is captured and converted into chemically useful carbohydrate forms such as sugars, starch and other metabolites. The reactions of light absorption in photosynthetic organisms can be either oxygenic or non-oxygenic, depending on the electron source used. Non-oxygenic photosynthesis in purple and green bacteria uses H_2S or organic molecules as the source of electrons[2], which will not be

discussed here. Oxygenic photosynthesis, which uses H_2O as a source of electrons, is our main interest.

A simplified overview of oxygenic photosynthesis process that occurs in the cells of plants, algae, cyanobacteria[3] is given by:

$$nCO_2 \ + \ nH_2O \ \xrightarrow{light} \ n\,(CH_2O) \ + \ nO_2$$
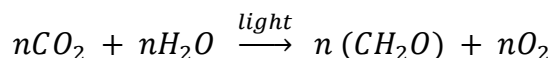
During this process, atmospheric CO_2 is converted into the organic compound (CH_2O) using the electrons harvested from solar water splitting (water oxidation using sunlight). This process could be broken up into two stages[4]:

$$2H_2O \ \xrightarrow{light} \ 4H^+ + \ 4e^- + \ 2O$$
$$CO_2 + 4H^+ + 4e^- \ \longrightarrow \ (CH_2O) \ + \ H_2O$$
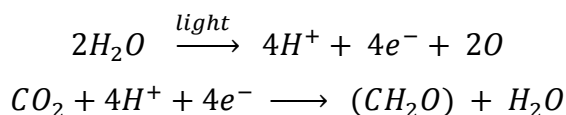
where the first reaction, light reaction, also called photochemical reaction, requires solar energy to split water. However, the other reaction, CO_2 consumption, don't explicitly require light. This is usually referred to as the dark or biochemical reaction.

1.2 STRUCTURES ESSENTIAL TO THE CYANOBACTERIAL PHOTOSYNTHETIC APPARATUS

In plant leaves and algae, chloroplasts located at the cells are the responsible organelles for photosynthesis. Chloroplasts contain an aqueous fluid called the stroma, and a membrane-bound structure embedded in the stroma called the thylakoid. Light-driven photochemical reactions in the process of photosynthesis occur in the thylakoids while the dark reactions occur in the stroma of the chloroplasts to complete the chemical changes.

Cyanobacteria are highly evolved photosynthetic bacteria, which have minimal nutrient requirements. Cyanobacteria are photosynthetic and aquatic and often called "blue-green algae". The thylakoid membranes of cyanobacteria, which is the layer that surrounds the thylakoid, do not contain membrane-bound organelles and thus no chloroplasts. In cyanobacteria, the thylakoid lies free within the cell interior with various arrangements.[5,6]

1.3 THE FUNCTION OF THYLAKOID MEMBRANE

The thylakoid of plants and cyanobacteria contains chlorophyll, which is the light-collecting pigment. The thylakoid membrane houses the transmembrane protein components responsible for the light activated water splitting and the photosynthetic electron transfer chain. There are four basic components densely packed within the thylakoid membrane, two types of photosystems named photosystem I (PSI) and photosystem II (PSII), cytochrome b_6f complexes (pivotal for photosynthetic electron transport) and ATP synthase complexes.

The two light-harvesting systems, PSI and PSII, contain specialized pigment-protein complexes called the reaction centers. These photosynthetic reaction centers (RC) comprise slightly different chlorophyll pigments that allow for different kinds of light absorption. The reaction center in PSI contains a chlorophyll dimer (P_{700}) whereas PSII has a reaction center called P_{680} (refer to Figure 1.1).
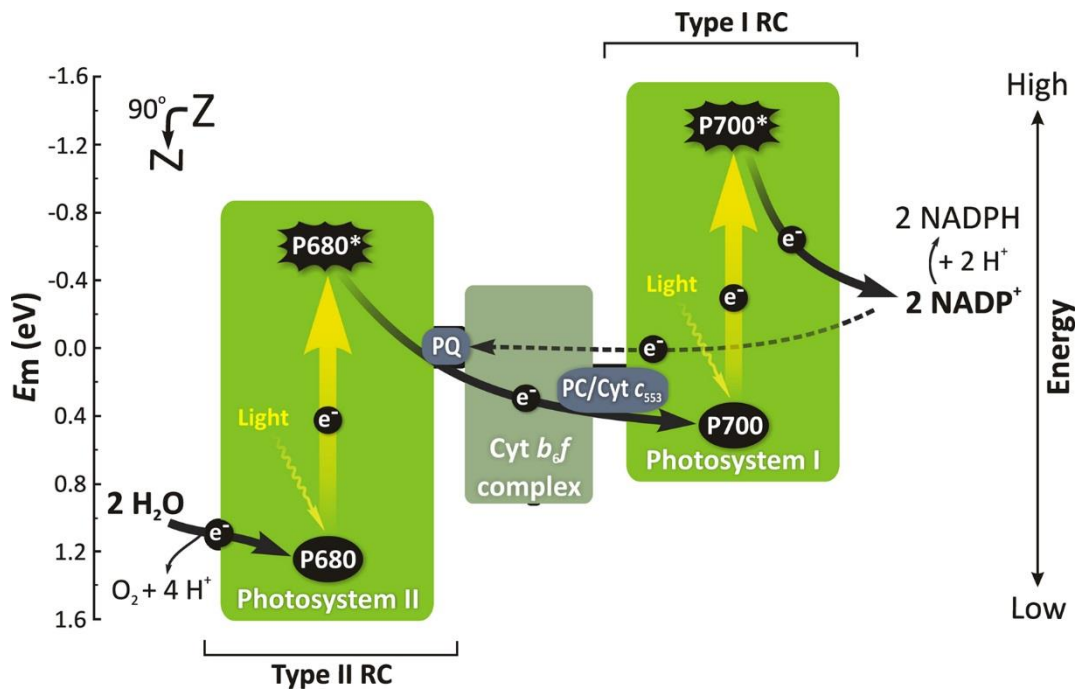
Figure 1.1 The light photochemical reaction that occurs in the thylakoid membranes, which is described by the so-called z-scheme.[2]

During light activation, once a photon is absorbed by a PSI/PSII, it is funneled to the RC chlorophyll. The RC in PSI and PSII absorbs wavelengths of light up to 700 nm and 680 nm, respectively. If light is absorbed by a chlorophyll molecule in the vicinity of PSII, the excitation

energy from an exciton generation transports between the chlorophyll molecules until it reaches P_{680} with nearly 100% quantum efficiency.[7] The solar photon absorbed by chlorophylls or by exciton transfer from antennae results in a redox (oxidation-reduction potential) energy. This energy initiates the redox pathway with a potential barrier that is stabilized in the RC to prevent wasteful recombination reactions. Thus, the photoactivated electron goes down the energy barrier along the redox pathway thereby facilitating the electron transfer from the specialized donor molecule(s) (P700) to the terminal acceptor in PSI. Secondary and tertiary electron transfers further increase the distance between the donor and acceptor which in turn stabilizes the generated radical, providing sufficiently long lifetime (milliseconds) to permit electrons to be extracted from the system.

1.4 PHOTOSYSTEM I (PSI) FROM A FUNCTIONAL POINT OF VIEW

Photosystem I (PSI) is the light-driven plastocyanin-ferredoxin oxidoreductase in the thylakoid membranes of cyanobacteria that catalyzes the light-driven electron transport from reduced plastocyanin (or cytochrome *c6*) located in the lumen side of the membrane to soluble ferredoxin (or flavodoxin) on the stromal side by a chain of electron carriers. The X-ray structural analysis at 2.5A° of PSI from Thermosynechococcus elongatus [8] has revealed the stepwise electron transfer pathway, from exited $P_{700}{}^*$ (a dimer of Chlorophyll *a* molecules) (E_m = -1.3 V vs. SHE) to a primary acceptor, A_0 (also a Chlorophyll *a* molecule) and then to a series of secondary electron acceptors, A_1 (a phylloquinone molecule) and three [4Fe–4S] clusters, named F_X, F_A and F_B that interface with the ferredoxin (or flavodoxin) on the stromal side. Once the electron reaches the terminal iron-sulfur cluster F_B (E_m = -520 mV/-580 mV vs. SHE), it reduces the soluble redox protein ferredoxin (or flavodoxin) (E_m = -440 mV vs. SHE). Then the soluble electron acceptor ferredoxin (or flavodoxin) transports the electron to the subsequent steps of photosynthesis. On the lumenal side of PSI, the vacant "hole" at the P_{700} is filled with an electron from soluble plastocyanin (or cytochrome *c6*). Hence, oxidized reaction center, $P_{700}{}^+$ (Em ≈ 490 mV vs. SHE) is then reduced back to P_{700} (Em = 430 mV vs. SHE) after absorbing one electron from the reducing reagent.[9-11]

The aforementioned photochemical charge separation is an extremely fast process (from excited P_{700} via A_0 to A_1 within picosecond time scale and the transfer from A_1 via F_X to F_A and F_B within nanosecond time scale).[11] In fact, the reaction time of electron transfer through the PSI

complex, transfer of electrons from P_{700} to ferredoxin and electron transfer chain and ATP synthesis, is picoseconds (10^{-12}), nanoseconds (10^{-9}) and microseconds (10^{-6}), respectively.[12] The robust structural and photoactive electrochemical properties of PSI, a transmembrane protein, makes it an ideal candidate for incorporation into solid state bioelectronic or hybrid photovoltaic devices.[13] But the first step towards rational design of such bio-hybrid deices require systematic integration of PSI into organic/inorganic frameworks that can be interfaced with donor/acceptor electrodes in solid-state devices in a facile and yet efficient manner.

To this end, a flurry of research in recent years have focused their attention on many strategies toward immobilizing PSI onto conductive substrates or materials (gold, titanium oxide, silicon, graphene, or gallium (III) arsenide (GaAs), carbon nanotubes or other nanoparticles, and redox polymers).[14-23] The original work pioneered by Greenbaum (1985) utilized platinized chloroplasts for photo-catalyzed hydrogen production, wherein PSI photo-reduced catalytic platinum on the surface of the chloroplast and produced hydrogen upon further illumination.[24]

In 1989, Greenbaum further isolated PSI complexes from the chloroplasts, chemically modified the surface of PSI with platinum and immobilized PSIs on fiberglass filter paper.[25] This work, demonstrated that the thylakoid-platinum combination in contact with metal electrodes was capable of generating a sustained flow of current under illumination. Motivated by this work, several groups have used platinized PSI as a photoactive material for hydrogen production. [26-28] Furthermore energy production has been investigated for systems fabricated by 2D array of platinized PSI particles welded onto metal surface [29] and oriented multilayers of genetically modified platinized PSI.[30]

In 1997, Greenbaum and co-workers reported the use of scanning tunneling spectroscopy to perform current-voltage (I-V) measurements on individual PSI proteins indicated that PSI complexes immobilized on gold function as individual photodiodes. This work also provided a qualitative insight into the orientation of the electron transport vector of PSI on the electrode surface based on the changes in the shape of the I-V scan.[31] Following this work, Kievit et al. obtained the electrochemical signal of P_{700} from solubilized PSI via square wave voltammetry in addition to cyclic voltammetry.[32] Such fundamental electrochemistry studies of PSI were further enhanced by Rusling and co-workers who reported direct electron transfer measurements between the P_{700} reaction center and the F_A/F_B iron-sulfur clusters of PSI in a lipid film on an electrode surface by using cyclic voltammetry.[33] Soon thereafter, the photocatalytic capabilities of PSI

complexes in solution were established via investigation into the light-induced electron transfer between PSI and various redox couples present in the system by using cyclic voltammetry.[34]

The integration of PSI into a solid-state photovoltaic device eventually evolved as late as 2004. Electronic integration of the devices was achieved by self-assembling an oriented monolayer of PSI, stabilized with surfactant peptides, and coated with a protective organic semiconductor.[35] Since then, several research groups worldwide have worked to further illustrate the fundamentals of electron transfer within PSI complexes, improve incorporation and assembly of oriented PSIs in the bio-hybrid photovoltaics and enhance the artificial electron transfer to and from PSI in such devices. The most significant of these studies include the work by Terasaki and coworkers who achieved photocurrent enhancement via fabrication of a high-surface area electrode consisting of gold nanoparticles decorated with PSI. By using gold nanoparticle, this methodology produced larger catalytic currents than planar electrodes.[14] To this end, efforts were also directed toward the genetic mutation of PSI to enable direct wiring of PSI to electrodes in order to fabricate efficient PSI-based biohyrbrid photosensors.[36-38]

Later, Carmelli and coworkers have measured the photoactivity of an oriented monolayer of PSI on a conducting metal surface via Kelvin force probe microscopy to generate electric potential maps. Electric potential images represented the change in surface voltage of PSI film in response to irradiation. This solid state system was constructed by inserting cysteine mutants on the lumenal side of PSI, that provided direct thiol coupling to the gold surface.[39] Later on, they produced oriented PSI multilayer films by reducing platinum ions on the reducing stromal side of the protein to allow for Pt-sulfide bonds above the initial monolayer[30] in an effort to integrate PSI into a field effect transistors.[21] In recent years, the Carmelli group had also measured the photocurrent generated by a single PSI by using scanning near-field optical microscopy. In their set-up one side of the protein is anchored to a gold surface via cysteine groups and the other is contacted by a glass tip metallized by a thin gold film. The tip served as both counter electrode and light source and PSI was optically excited with a laser from the back of the tip. Photocurrent measurement was done following covalent bonding of a gold-covered glass tip to an individual PSI.[15] The use of specifically terminated alkanthiols as SAM layers for anchoring PS onto electrodes was effectively implemented by Cliffel, Jennings and coworkers in integrating PSI with various electrode surfaces. Their work started by adsorbing PSI films onto substrates modified with self-assembled monolayers (SAMs) with various ω-terminated alkanethiols [40] and investigating the role of

7

alkanethiol on PSI monolayer ordering. In 2006, they demonstrated PSI entrapment within films comprised of long-chain alkanethiols using a backfilling technique.[41] By using scanning electrochemical microscopy, they revealed the selective deposition of PSI onto pre-patterned surfaces.[42] Their photocurrent measurements of a sparse layer of PSI physically adsorbed on an electrode [43] was followed by creating covalent attachments between PSI and the electrode materials [44], wherein enhanced photocurrent production via improved electronic interactions and higher coverage of PSI was achieved. Furthermore, their work demonstrated enhanced light absorption by increasing the surface area of their underlying electrode [16] and utilizing thick multilayer films of PSI.[45,46] In 2014, by utilizing a semiconducting electrode substrate, they demonstrated dramatically improved photocurrent density.[17] With the aim of improving the photoactivity of their PSI-modified electrodes, they investigated the extent and effect of electrochemical mediator and the underlying electrode material [17,47,48] and established the feasibility of conjoining carbon-based materials, such as graphene with PSI as potential constructs in next-generation photovoltaic devices.[19,20] Moreover, they investigated the ability for these electrodes to generate hydrogen fuel after photoreduction of catalytic platinum on the surface of the PSI film.[18] In continuation with these efforts in anchoring PSI to inorganic substrates via chemical linkers, Frymier, Boder and coworkers employed sortase-mediated ligation of PsaE-modified PSI to a conductive surface to obtain preferentially orientate PSI monolayers on gold and demonstrated photocurrent improvement with this attachment technique.[49]

In spite of the large volume of work highlighted in the aforementioned literature review, on the various chemical and inorganic routes to attach PSI to electrode substrates, much of these works relied on the use of some form of SAMs of organothiol-based compounds to immobilize PSI films onto metal surfaces (mostly gold). The origin of using SAMs on electrodes began with the work done by Lee et al. that tested SAMs terminated with –OH, –COOH, and –SH groups to attempt oriented immobilization of PSI, yielding 70% useful orientation when using an organic compound terminated with an –OH group due to the anticipated weak hydrogen bonding of the OH-terminations with the stromal side of the PSI. [31] It needs to be pointed out that although such hypotheses are scientifically plausible, the rigorous verification of PSI density with orientations that achieve directional alignment of PSI electron vectors on SAM monolayers remain challenging. Thus, rigorous studies by Manocchi et al. had resulted in detailed investigation of the influence of various surface modifications on electrophoretic deposition of PSI onto gold substrates that

were functionalized with – CH$_3$ (hexanethiol), –CH2-NH2 (aminohexanethiol), –CH2-OH (mercaptohexanol), and –COOH (mercaptohexanoic acid) terminated SAMs. By conducting photochronoamperometry measurements, they demonstrated that the surface charge of the SAM can control the quantity of bound PSI.[50]

In more recent years, our group had also begun fundamental investigations of systematic immobilization of PSI monolayer films onto substrates modified by SAMs of OH terminated alkanethiol as a means to fabricate bio-abio interfaced electrodes for incorporation into bio-hybrid photovoltaic and photoelectrochemical cells.[51] Through our preliminary studies on the colloidal chemistry of solution-phase PSI, uniform and dense monolayers of PSI on the SAM substrates were self-assembled by tuning the PSI and detergent concentration during gravity-driven deposition. Furthermore, the effect of electrophoretic depositions in controlling the morphology of PSI assembly on thiolated surfaces were also studied to achieve directed assembly of PSI on SAM substrates under externally applied electric field. Subsequently, various experimental protocols for the assembly of PSI-SAM/gold systems were investigated by studying the effects of temperature, monomeric or trimeric forms of PSI, the type/concentration of detergents used, and assembly mechanism on the adsorption of PSI to the surface through the use of isotropic fluorescent antibody attachments on PSI to detect their orientations on substrates.[52] Added to this, the role of detergents in tuning PSI-PSI interactions through PSI-detergent colloidal chemistry were carefully studied to monitor their solution phase aggregations and hence, tailor the morphology of surface immobilized PSI thin films.[53] In a recent study elucidating the role of dissolved O$_2$ in mediating photoactivated electron transport pathway from surface immobilized PSI in electrolyte solutions, we have recently reported the detailed electrochemical investigations on uniform PSI monolayer systems assembled on alkanethiolate SAM/gold surfaces in the presence of methyl viologen (MV^{2+}) as the redox mediator.[54]

Although such efforts are commendable, a significant knowledge gap still exists in the reliable verification of the orientation and long-term functionality of photoactive PSI to enable photo-excited charge transfer with near unity quantum efficiency on these SAM-based assemblies outside of its natural thylakoid membrane housing. Although the aforementioned efforts in our group have been largely effective in depositing dense monolayers or multilayers of PSI with some success toward preferential orientation of PSI, the relatively low levels of photocurrent generation from these systems have increasingly drawn our attention towards the role of the natural membrane

9

scaffoldings in PSI trimeric complex in enhancing the efficiency and lifetimes of its photochemistry. The efficient electron transfer between oxidized and reduced redox partners of PSI occurs on opposite sides of the thylakoid membrane, while the specific protein confirmation within the thylakoid membrane ensures the optimal stereochemistry for the inter-chromophore excitation energy transfer pathways.[11] Hence, the first step towards the successful fabrication of bio-hybrid devices capable of high photocurrent generation call for systematic assembly of oriented and functional PSI onto desired bio-abio interfaces via suitable protein scaffoldings. To this end, one must address the obvious question regarding the role of the natural thylakoid membrane housing of PSI trimeric complex in providing the required structural and functional scaffold to the protein. This had led to a growing interest in membrane reconstitution of PSI complexes to form stable proteoliposomes as the final product. Reconstituted proteoliposomes serve as experimental systems for the study of membrane enzymes [55] and small helical membrane proteins, providing a sample environment that accurately mimics the native membrane environment and properties such as hydrophobic thickness, water concentration gradient and lipid order parameter gradient.[56,57]

A recent work by Saboe et al. had reconstituted PSI into a two-dimensional crystal with tethered bilayer lipid membrane support that indicated a 4-fold photocurrent enhancement through the incorporation of conjugated oligoelectrolytes (COEs) units in this device.[58] COEs have been utilized in several studies conducted by this group, where their membrane disrupting properties, structural modifications [59,60] and their effect on membrane permeabilization [61] have been investigated. Specifically, more recently Bazan and coworkers have also investigated the photo-bioelectrochemical impact of a series of COEs directly incorporated into thylakoid bioanodes and reported up to 2.3-fold improvement in amperometric photocurrent density generation.[62] Furthermore, such studies were also extended to the stabilization of PSI in and on a block copolymer support assembled on SAM/gold electrodes that were characterized via pump-probe optical spectroscopy and photochronoamperometry measurements[63] to demonstrate enhanced photocurrent in the presence of COEs. In line with these works, there have also been recent efforts in constructing three-dimensional architectures comprising of the redox protein cytochrome c (cyt c) as a molecular scaffold for PSI as the photo-functional matrix element aided by DNA molecules as further building blocks.[64] This study, in turn, resulted in the fabrication of 3D architectures consisting of transparent mesoporous indium tin oxide (μITO) electrodes in

combination with PSI and cyt *c* that had reported an internal quantum efficiency (IQE) of ~39% that is considered one of the highest values for PSI assemblies on inorganic electrodes. One of the interesting aspects of the study is that they possibly attribute such high IQE to the high protein loading and efficient electron pathways inside 3D transparent conducting oxides.[65] The aforementioned studies indicate significant photocurrent enhancements due to the incorporation and possibly, the confinement of PSI in biomimetic scaffolds. Such promising as well as intriguing results shed light on the photocurrent enhancements arising from the high packing density and orientation of PSI in these complexly tailored biomimetic scaffolds. Yet, the exact role of the specific membrane scaffolds and microenvironment alterations in driving the enhanced photoactive functionality and near unity quantum efficiency in PSI owing to the conformational changes in its native membrane bound form remains elusive. In turn, these studies leave us with an unanswered question regarding the biophysical role of membrane confinements in driving the optoelectronic dynamics and charge transfer properties within PSI. Our main motivation in the present study stems from the desire to attain systematic incorporation of PSI complexes into synthetic membrane-bound structures that mimic the natural thylakoid membrane housing of PSI. The central hypothesis behind this motivation is that PSI confinements in biomimetic membrane frameworks will allow us to tune inter-chromophore electronic coupling within the protein complex by many orders of magnitude through the optimization of chromophore separation and orientation, thereby promoting highly enhanced photocurrents with quantum efficiencies analogous to the natural thylakoid membrane-bound PSI trimers. To this end, as the first step towards our continual effort to investigate the optoelectronic behaviors of PSI confined under different bio-abio interfaces, the current thesis work focusses on a fast and elegant approach to achieve high density PSI encapsulation in synthetic lipid bilayer membranes to constitute PSI-proteoliposomes followed by their incorporation into biohybrid electrodes for investigating their photocurrent enhancements arising from the confinements.

Building from our earlier results, the studies presented in this work further elucidate the photocatalytic behavior of PSI complexes in electrochemical systems. Specifically, this dissertation is focused on:

1) Establishing a comprehensive understanding of the lipid-detergent phase transition during detergent mediated liposome solubilization as the first step for detergent-mediated membrane protein reconstitution and successful PSI-proteoliposome formation (Chapter 2).[66]

2) Identifying an efficient route for detergent mediated reconstitution of Photosystem I-Proteoliposomes (Chapter 3).[67]

3) Investigating the ability of biohybrid electrodes made from biomimetic incorporation of Photosystem I to generate enhanced photocurrent and improved electrode stability by providing effective electron pathways (Chapter 4).[54]

CHAPTER 2

LIPID-DETERGENT PHASE TRANSITIONS DURING DETERGENT MEDIATED LIPOSOME SOLUBILIZATION

This Chapter is based on the published paper.

"Lipid-detergent phase transitions during detergent mediated liposome solubilization," Hanieh Niroomand, Guru A. Venkatesan, Stephen A. Sarles, Dibyendu Mukherjee and Bamin Khomami, Journal of Membrane Biology (2016) 249, 523-538.[66]

2.1 INTRODUCTION

Membranes play a critical role in defining the structure and function of all prokaryotic and eukaryotic cells in plants and animals. Membranes define compartments, and their structures determine the nature of all communication between the inside and outside of cellular regions. Proteins and lipids constitute the major components of membranes. Phospholipids, either in the form of bimolecular leaflets or in micellar arrangements, constitute the foundations of membrane structure.[68] The relative amount of proteins and lipids vary significantly, ranging from about 20% (dry weight) protein (myelin) to 80% protein (mitochondria).[69] A fundamental understanding of the solution phase morphologies during membrane-surfactant (detergent) interactions is critical for successful isolation, purification, reconstitution, and crystallization of membrane proteins.[70-76] Such morphological characterization is also important for understanding the formation mechanism of complex structures by membrane proteins and detergents when reconstituted into artificial lipid membranes – a critical research area for the development of new drugs.[77-81]

The present study is motivated by the need for incorporation and assembly of individually oriented Photosystem I (PSI), a trimeric photosynthetic transmembrane protein complex of relatively large size (~ 1000 kDa), into membrane-bound structures that mimic the natural thylakoid membrane housing of PSI. Such membrane-bound assembly of PSI complexes finds wide applications from membrane protein crystallization to our research interests in designing bio-hybrid opto-electronic devices. Specifically, the lipid content of a thylakoid membrane predominantly consists of two kinds of phospholipid, phosphatidylcholine (PC), and phosphatidylglycerol (PG), along with other glycolipids, such as monogalactosyl diacylglycerol (MGDG), digalactosyl diacylglycerol (DGDG), and sulfoquinovosyl diacylglycerol (SQDG).[82-85]

To this end, we focus our attention on the potential use of PC and PG lipid membranes to mimic bilayer systems that provide bio-mimetic housing for PSI extracted from *Thermosynechococcus elongatus* (*T. elongatus*). Four basic strategies can be used for the insertion

of membrane proteins into liposomes. These include sonication, freeze-thawing, organic solvents, and detergents. The first three methods have limitations in efficient proteoliposome reconstitution including possible local probe heating during sonication that leads to degradation and denaturation of many membrane proteins. Similarly, organic solvents denature most amphiphilic membrane proteins even though reverse-phase evaporation and solvent injection using organic solvents enable efficient liposome preparations.[77,79] However, since membrane protein purification regularly requires the use of detergents, detergent mediated solublization has become a preferred route for proteoliposome preparations.[86] Furthermore, our recent studies reveal that two prototypical non-ionic detergents: *n-dodecyl-β-D-maltoside* (DDM) and Triton X-100 (TX-100) with low critical micellar concentrations (CMC) can be systematically used for PSI solubilization without denaturing the protein.[51-53]

Membrane solubilization typically comprises of a three-stage process represented by the structural transitions that occur as detergents interact with lipid membranes.[70,73,74,87] These transitions are typically analyzed qualitatively by turbidity measurements.[86] As a function of increasing detergent concentrations, the abovementioned stages are: (I) a stage containing detergent monomers and vesicles wherein detergent monomers start getting incorporated into vesicles; (II) a stage where detergent monomers, mixed vesicles, and mixed micelles coexist (detergent being incorporated into vesicles); and (III) a stage that consists purely of micelles at varying detergent/lipid ratios and detergent monomers. In the first stage, detergent molecules incorporate into the lipid bilayer without disrupting the membrane, and the vesicle remains intact. This detergent insertion induces an initial swelling of the liposomes[88] that leads to the critical detergent concentration, R_{sat}, marking the onset of solubilization in typical optical density measurement data (shown by the cartoon in Figure 2.1a Further increase in detergent concentration yields higher detergent insertion (stage II), which causes some of the vesicles to break into lipid micelles that can coexist with detergent-saturated vesicles and detergent micelles. This process is linked with bilayer flip-flop (detergent flip over from outer monolayer into the inner monolayer of the bilayer) where, based on the choice of detergents and lipids, different mechanisms of membrane solubilizations can be initiated.[74,89] Typically, turbidity measurements show a decreasing trend during this stage up to the point marked as R_{sol}, where the optical density reaches its minimum indicating a complete solubilization of liposomes by detergent molecules. Finally, all membrane components are fully solubilized into mixed micelles (stage III) once the detergent

concentration in the bilayer exceeds R_{sol}, and the suspension becomes optically transparent.[90] It should be mentioned here that earlier works on detergent-mediated membrane protein reconstitution mostly report a window of detergent concentrations between the saturation and solubilization point as the suitable point for protein insertion. Yet, very little is known regarding the optimal morphology of the lipid-detergent mixed bilayer systems that promote the interfacial chemistry for membrane protein assembly.

Few prior studies have systematically investigated the detailed role of lipid-detergent interactions during detergent-mediated protein reconstitution in liposomes. In the past, most studies on the solubilization of phosphatidylcholine lipids with TX-100[73,91] and DDM[92] involve PC lipids from egg, plant or *E. coli*. More recently, synthetic lipids are also used in lipid-detergent interaction studies.[93-97] In an effort to achieve lipid compositions that both mimic natural thylakoid membrane systems and provide robust bio-mimetic housings for PSI, we study purely synthetic lipids with saturated fatty acids, which eliminate the complexity of natural phospholipids due to different acyl-chains. Past studies have mostly focused on detergent mediated transport protein reconstitutions in liposomes prepared from PC plus phosphatidic acid (PA) with detergents such as TX-100, n-octyl ß-D-glucopyranoside (octylglucoside), octaethylene glycol monododecyl ether (C12E8), sodium cholate or sodium deoxycholate.[80,98] Similar studies with transport proteins have also been performed in liposomes prepared from *E. coli*, and *E. coli* plus egg PC with DDM and TX-100 as detergents.[88,92,99]

However, few studies have been conducted for small membrane proteins with molecular weights of $\sim$ 30-80 kDa.[100-103] And, only a handful of attempts have been made to date to reconstitute large membrane proteins into liposomes. To this end, fluorescence quenching measurements have been used to monitor detergent mediated incorporation of monomeric PSI reaction centers (extracted from *Synechocystic sp* PCC6803), in liposomes prepared from egg PC and PA lipids.[104] Protein activity has also been monitored for PSI particles from spinach incorporated into PG lipid complex[105], but both of the aforementioned works lack imaging techniques. However, recent AFM measurements of three membrane proteins from the bacterial photosynthetic apparatus reconstituted into a planar lipid bilayer[106], leave room for a clear elucidation of the structural and morphological arrangements in the proteoliposome formation.
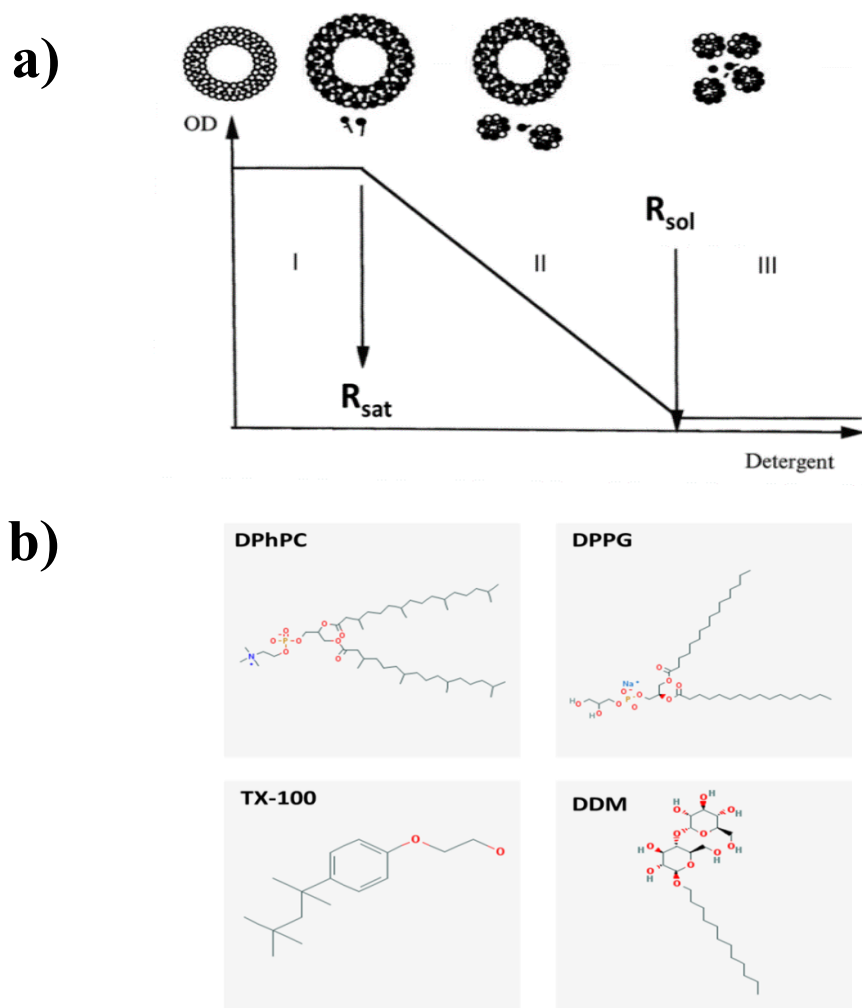
Figure 2.1 (a) Graphical representation of different stages during the lamellar-to-micellar transition; (b) Molecular structure of lipids (DPhPC, DPPG) and detergents (TX-100, DDM). DPhPC and DPPG are molecules with two hydrocarbon chains of 16 carbons with total lipid molecule length of $\sim 2-3$ nm. TX-100 molecule length is $\sim 3.75-4.0$ nm and DDM molecule length is $\sim 2.75-3.0$ nm. Detergent molecule sizes given are based on half of the micellar hydrodynamic diameter.[20]

To address these knowledge gaps, the first rational step requires systematic and detailed morphological characterizations of the phase transitions during detergent mediated liposome solubilization. Specifically, we investigate the morphological variations induced by the detergent mediated solubilization of 1,2-diphytanoyl-*sn*-glycero-3-phosphocholine (DPhPC) and 1,2-dipalmitoyl-*sn*-glycero-3-phospho-(1'-*rac*-glycerol) (DPPG) liposomes by the two non-ionic detergents, DDM and TX-100 by means of turbidity measurements, dynamic light scattering, negative-staining electron microscopy (NS-EM), and cryo-transmission electron microscopy (cryo-TEM). Each of the aforementioned measurements is systematically conducted during different stages of stepwise solubilization of preformed liposomes with varying detergent concentrations.

For ease of visualization and understanding, Figure 2.1b represents the structural details of lipids (DPhPC and DPPG) and detergents (DDM and TX-100). Because of their branched hydrophobic side chains (as shown in Figure 2.1b earlier), DPhPC membranes exhibit greater mechanical stability and lower permeation to ions and water than unbranched phospholipids.[107] While not native to plants or animals, DPhPC has been a good choice of phospholipid for the study of reconstituted channel-forming proteins [108,109], crystallization of proton channel peptides [110], and ion-conducting measurements.[111] Other forms of artificial lipid membranes such as black lipid membranes (BLMs), supported lipid membranes (SLBs), giant unilamellar vesicles (GUVs), and droplet interface bilayers (DIBs) have also utilized DPhPC to form highly stable membrane models.[112-114] In addition, the methylated side chains of DPhPC enable it to exhibit high chemical stability over a wide pH range and cause it to exist in a fluid-like thermotropic state across a wide temperature range (at least from -20°C to 70°C) without any detectable gel-to-liquid crystalline phase transition, perhaps owning to steric interference of the methyl groups in the ordered packing of the isoprenoid residues.[113,115] On the other hand, DPPG, is an anionic phospholipid with gel-to-liquid crystalline transition temperature at ~ 41°C and devoid of any methyl branches (see Figure 2.1b earlier).[116] DPPG is frequently used as mimetics of bacterial membranes in biophysical studies on the effect of antimicrobial peptides.[117,118]

The results presented in this work shed light on the suitability of DDM or TX-100 as the detergent of choice for the solubilization of both DPhPC and DPPG lipids. Our observations indicate that, depending on the detergents (DDM or TX-100) and the lipids (DPhPC and DPPG) used, two possible pathways can result in the well-known, three-stage solublization process or a

phase transition into networks of complex structural arrangements. The present study uses the aforementioned characterizations to reveal the mechanism by which membrane bilayers undergo complex structural arrangements during different stages of their solubilization process. In turn, such studies pave the path for determining the specific morphological arrangements of lipid bilayer membranes constructed from DPhPC and DPPG that are suitable for detergent-mediated membrane protein reconstitution and successful PSI-proteoliposome formation.

2.2 EXPERIMENTAL SECTION

2.2.1 Materials.

Dibasic (Na_2HPO_4) and monobasic (NaH_2PO_4) sodium phosphate with >99% assay were purchased from Fisher Scientific to prepare the aqueous buffer solutions of 200 mM Na-Phosphate with pH = 7.0. All aqueous buffer solutions of 200 mM Na-Phosphate were prepared in ultrapure de-ionized (D.I.) water with a resistivity of 18.2 MΩ.cm at 25°C (Millipore, Billerica, MA). *n*-Dodecyl-β-D-Maltoside (DDM) was purchased from Gold Biotechnology whereas Triton X-100 (10% w/v aqueous solution) was obtained from Anatrace. 1,2-diphytanoyl-*sn*-glycero-3-phosphocholine (DPhPC) and 1,2-dipalmitoyl-*sn*-glycero-3-phospho-(1'-*rac*-glycerol) (DPPG) were purchased as lyophilized powders from Avanti Polar Lipids, Inc. Polycarbonate filters were also purchased from Avanti Polar Lipids, Inc. Phosphotungstic acid hydrate (PTA) was purchased from Electron Microscopy sciences. Potassium hydroxide pellets (KOH) with >99% assay were purchased from Fisher Scientific. Carbon coated (400 mesh) copper grids and lacy carbon coated (200 mesh) copper grids were purchased from SPI Supplies, USA.

2.2.2 Methods.

2.2.2.1 Liposome Preparation.

4 mg ml^{-1} lipid suspensions were prepared in 200 mM Na-phosphate (pH = 7.0) buffer, followed by 3-4 freeze-thaw cycles to form multilamellar liposomes. These suspensions were then extruded through 100 nm pore sized filter using a mini-extruder (Avanti Polar Lipids) to form unilamellar vesicles at room temperature for DPhPC suspension and at 50°C for DPPG (i.e., above the transition temperature of DPPG at 41°C). The large unilamellar vesicle size of ~100 nm was

confirmed from dynamic light scattering measurements. Further details regarding the lipid vesicle preparations can be found in previous literature.[119]

2.2.2.2 Titrations of Liposomes with Detergent.

Liposome suspensions of 4 mg ml^{-1} titrated by stepwise addition of several aliquots of 10% wt vol^{-1} of TX-100 or DDM to 5 ml of the diluted liposome suspension. Detailed technical specifications regarding the physical properties of DDM and TX-100 are provided in Table 2.1.[78,92,120] The effect of detergent on the liposomes was monitored by measuring the optical density at 540 nm (optimal wavelength for liposome adsorptions) with a hybrid multi-mode microplate reader (Make: Biotek; Model: Synergy H1). All turbidity data were averaged over four experimental runs.

Table 2.1 Physical properties of the detergents, TX-100 and DDM[53]

	MW	Aggregation Number	Micellar Weight (KD)	CMC (mM)
Triton X-100	625	73-140	46-90	0.21
DDM	511	98-140	50-71	0.16

2.2.2.3 Dynamic Light Scattering (DLS).

To analyze the liposome size alterations induced by the interaction with the detergent molecules, dynamic light scattering measurements were carried out using a 632.8nm-wavelength Zetasizer (Malvern Instruments). All DLS data were collected using a 178° backward scattering and averaged over four experimental runs each of which were summed up over 12 time correlograms fitted by the Zetasizer software. Due to the presence of bimodal or multimodal size distributions in some phase stages of the solubilization process, the DLS data are represented by more than one curve. All reported sizes are in terms of equivalent spherical hydrodynamic radius as estimated from Stokes–Einstein relation, and all DLS analyses are represented in terms of number distribution or volume distribution. The data analysis was carried out using the effective thermo-physical properties of 200 mM Na-Phosphate aqueous buffer solutions with pH = 7.0. Previous kinetic studies of the interactions of DDM with preformed liposomes indicate a delay

time of ~ 2–3 h to achieve equilibration for constant light-scattering data. Hence, to ascertain complete detergent equilibration, DLS and turbidity measurement of DDM interactions with liposomes were performed 4 h after detergent-lipid suspension preparation.

2.2.2.4 Scanning Transmission Electron Microscopy (STEM).

Negative staining embeds and supports the thin layer of biological sample by a dried layer of heavy metal-containing salt, thereby increasing the contrast of biological material with their surroundings without causing structural alteration.[121,122] A sequential two-droplet method was used for negative staining. Aliquots (~ 5 µl) of the lipid/detergent in buffer suspensions were adhered to thin carbon-coated 400-mesh copper grids that were glow-discharged for 20s to render them hydrophilic. The suspension was incubated for 1 min at room temperature. Excess sample solution was removed by blotting with a filter paper touched to the edge of the grid. After removing the excess fluid, the grid was stained with 2% (w/v) potassium phosphotungstate (KPTA) at pH = 7.0 for 60s. Then the grid was dried at room temperature. Negatively stained specimens were examined with the Zeiss Auriga FIB-SEM microscope operated at 30 kV in STEM mode.

2.2.2.5 Cryo- Transmission Electron Microscopy (Cryo-TEM).

Cryo-TEM allows direct investigation of samples in their vitrified state at low temperature. The sample preparation for cryo-TEM technique was carried out on 200-mesh carbon coated holey grids. Before the sample application, a glow discharge was performed in order to hydrophilize the grid for optimal spreading of the aqueous sample.[123] The suspension was then drop cast onto TEM grids following which the excess sample was absorbed using a filter paper, leaving a thin film of sample in the holes of the grid. Then, the grid was mounted in a Gatan cryo-plunge 3 device and immediately frozen by plunging in liquid ethane cooled by liquid nitrogen. After vitrification, the frozen-hydrated specimen was inserted to the Gatan cryo-transfer system and transferred into the TEM system. The imaging was carried out by a Zeiss Libra 200 MC TEM equipped with a model Gatan 915 cryo-specimen holder, at an acceleration voltage of 200 kV, and a temperature of about -170 °C under strict low dose conditions (<15 e $A^{°-2}$). Images were recorded with a Gatan UltraScan 1000XP. Quantitative analysis of n>30 particles was used to measure the size of particles at each stage of solubilization.

2.3 RESULTS AND DISCUSSION

2.3.1 Surfactant Induced DPhPC Solubilization.

2.3.1.1 TX-100 Interaction with DPhPC.

The three stages of detergent-liposome interactions are identified as a function of increasing detergent concentrations (TX-100) from turbidity measurements on large unilamellar vesicles of DPhPC (see Figure 2.2a). In stage I, detergent molecules associated with the membrane bilayer without any structural alteration of the vesicles. Initial swelling of the liposomes caused by the detergent insertion into the bilayer corresponds to the onset of solubilization. At this stage, the concentration of free detergents remains below the CMC of the pure detergent up to R_{sat}[73] as indicated in Figure 2.2a. Further increase of detergent concentration results in bilayer saturation and consequently mixed micelle formations (stage II in Figure 2.2a). Beyond this stage, detergent addition results in more mixed micelle formation, which is indicated by the corresponding decrease in absorbance in the turbidity measurements. This decrease in the optical density data reaches a minimum at $R_{sol,}$ which marks the onset of solubilization (stage III in Figure 2.2a).

The different phase transitions of DPhPC liposomes observed from the abovementioned optical density measurements show excellent agreement with DLS data, (see Figure 2.2b, left panel). The three stages of the effect of TX-100 concentration (C_{Trit}) on DPhPC liposomes are represented by the three consecutive plots marked I, II, and III, respectively. These plots indicate that starting with intact liposomes with no TX-100, the particle size distribution (PSD in terms of number distribution, %) has a peak hydrodynamic diameter of $\sim$ 90 nm. With the addition of TX-100 in the concentration ranges $C_{Trit} \sim$ 0 - 2.9 mM, the peak size broadens and shifts to $\sim$ 160 nm as seen from the absorbance data in Figure 2.2a indicating a swelling of the mixed detergent-vesicles at the detergent concentration corresponding to R_{sat}. Beyond this point, increased detergent concentration results in a shift in the peak size (stage II in Figure 2.2b, left panel) from $\sim$ 160 nm (C_{Trit} = 2.3 mM) to $\sim$ 15 nm (C_{Trit} = 6.0 mM) that corresponds to the stage II in Figure 2.2a. Here we note that the co-existence of the second peaks at $\sim$ 100 – 150 nm indicate presence of mixed micelles with vesicles. The aforementioned shift into a smaller hydrodynamic diameter is due to the appearance of more mixed micelles as the concentration of detergent starts approaching R_{sol} ($C_{Trit} \sim$ 9.2 mM). Finally, the peak size of $\sim$ 13 nm at very high detergent concentration of C_{Trit} =

8.5 mM in Figure 2.2b, left panel (stage III) is consistent with turbidity measurements indicating the minimum optical density in stage III of Figure 2.2a due to the emergence of mixed micelles.

Morphological variations corresponding to the aforementioned solubilization stages are elucidated with cryo-TEM images of liposome structures in their vitrified states that correlate very well with the different stages indicated by our turbidity and DLS measurements. Starting with intact DPhPC liposomes after extrusion through 100 nm filters, regularly shaped unilamellar liposomes with delineated 4–5 nm lipid bilayer walls are observed (stage I in Figure 2.2b, right panel). Cryo-TEM images for stage I of DPhPC liposome solubilization with detergent concentrations below R_{sat} indicate the retention of the vesicular structures along with enlargement in the liposome diameter due to detergent incorporation within the membrane bilayers (refer to appendix I). Stage II of Figure 2.2b (right panel) indicates the appearance of lipid-detergent mixed micelles (~ 20 nm in sizes), along with stable open vesicular structures [89,94](~ 150 - 200 nm) at C_{Trit} ~ 6.2 mM. This bilayer opening is associated with the rapid solubilization of bilayers by detergents with relatively small polar moiety as in the case of TX-100. Such rapid solubilization is achieved due to detergent molecules acting from both sides of the phospholipid bilayer (transbilayer solubilization) that ultimately makes the permeable and disintegrate into mixed micelles.[89,91,94,95] Our observations in the present study indicates that addition of TX-100 to multilamellar DPhPC vesicles mimic the *trans*-membrane solubilization mechanism (refer to appendix I). The abovementioned mixed micelle formation due to detergent association is also supported by stained TEM images (refer to appendix II). Finally, at C_{Trit} ~ 8.4 mM, stage III of Figure 2.2b (right panel) represents the transition of the whole bilayer to spherical mixed micelles that also corresponds to stage III in Figure 2.2a and Figure 2.2b (left panel).

2.3.1.2 DDM Interaction with DPhPC.

The turbidity measurements for DPhPC with DDM indicate the familiar three-stage solubilization curve as also observed for the TX-100 case except that the maximum absorbance value at R_{sat} is much higher for the DDM case. Specifically, the peak absorbance value at R_{sat} for the DDM case in Figure 2.3a indicates a ~ 14 fold increase from the initial values for intact liposomes as compared to the corresponding ~ 3 fold increase for the TX-100 case. A stable turbidity level is reached almost instantaneously upon addition of TX-100 above R_{sat}, where for the DDM case, more than 2 hours is needed to reach a stable turbidity level.

23

Figure 2.2 Solubilization stages of preformed DPhPC liposomes at 4 mg ml^{-1} concentration induced by stepwise increase of TX-100 concentration (mM), as observed with: (a) turbidity measurements optimized for liposome adsorption at 540 nm; (b, left panel) number distribution from dynamic light scattering (DLS) and (b, right panel) corresponding cryo-TEM micrographs of each stage, indicating: (I) intact liposomes in absence of detergent; (II) liposome treated with detergent concentration above R_{sat} (C_{Trit} = 6.2 mM). The arrows indicate the open bilayer fragments, and (III) lipid-TX-100 micelles above R_{sol} (C_{Trit} = 8.4 mM). The arrow indicates the spherical mixed micelles.

Such differences in the turbidity behavior between DDM and TX-100 can be attributed to the two distinct vesicle-to-micelle transition mechanisms for these two detergents, as also reported in an earlier work of Stuart et al.[44]

The saturation and solubilization points for the DPhPC-DDM systems are identified as R_{sat} at $C_{DDM} \sim 4.7$ mM and R_{sol} at $C_{DDM} \sim 12.0$ mM respectively along with the solubilization stages I, II and III as marked in Figure 2.3a DLS data also confirm these stages, where stage I for the PSD in Figure 2.3b (left panel) represents the shift from peak size of ~ 90 nm for pure lipid suspension to the peak size of ~ 160 nm at $C_{DDM} \sim 3.2$ mM. Absorbance measurements in Figure 2.3a shows a systematic increase for DDM concentrations up to $C_{DDM} = 4.7$ mM. Beyond this point, increases in DDM concentrations are accompanied by a marked decrease in the relative absorbance (Figure 2.3a), which is in agreement with DLS measurements indicating a reduction in peak sizes scattered over $\sim 20 - 85$ nm at $C_{DDM} \sim 7.5$mM. This corresponds to the region of coexisting mixed micelle-mixed vesicle systems (stage II in Figure 2.3b, left panel). Finally, at $C_{DDM} = 11.0$ mM, which is close to the solubilization concentration (R_{sol}) in Figure 2.3a, the absorbance levels off to the minimum value, while the PSD indicates a peak size ~ 12 nm corresponding to only mixed micelle formation (stage III in Figure 2.3b, left panel). In comparison to the TX-100 mediated solubilization of DPhPC, the solubilization process with DDM indicates a broader stage II that persists up until $C_{DDM} > 10$ mM, as seen from Figure 2.3a.

Cryo-TEM images in Figure 2.3b (right panel), corresponding to the DLS data in Figure 2.3b (left panel) for each of the 3 stages, confirm the vesicle-micelle transitions for DPhPC treated with DDM. Intact vesicular structures of liposomes at $C_{DDM} \sim 4.3$ mM (vesicle diameter ~ 80 to 170 nm) are observed in stage I (right panel). Swelled yet, closed vesicles co-exist with mixed micelle structures at $C_{DDM} \sim 7.0$ mM (size distributions $\sim 150 - 180$ and 20 nm) in stage II (right panel), where liposome disintegration into small worm-like mixed micelles at $C_{DDM} \sim 9.5$ mM (micelle diameter ~ 12 nm) are seen in stage III (right panel). These images correlate extremely well with earlier absorbance data (Figure 2.3a) and PSD peaks (Figure 2.3b, left panel). A few closed liposome structures are observed even at stage III of solubilization, (see Figure 2.3b, right panel). Closed vesicle to micelle transition has been attributed to the larger and polar head groups of DDM initiating a slow detergent solubilization of the bilayers. Such solubilization involves the micelles getting pinched off from outer monolayer of the vesicles. Thus, in the second stage of solubilization, (stage II) small worm like mixed micelles coexist with closed vesicle. This

mechanism is known as micellar solubilization.[89,94] Previous studies on egg PC treated with DDM have revealed the formation of long string-like structures during stage II and appearance of transitional "gel-like" state at the end of stage II.[90,92] But, in our present studies with DPhPC, we only observe worm-like micelles at stage II and stage III that are below 20 nm in size. The aforementioned observations are further validated through STEM images of the solubilization stages II and III (refer to appendix III).

2.3.2 Surfactant Induced DPPG Solubilization.

2.3.2.1 TX-100 Interaction with DPPG.

In the case of solubilization of DPPG liposomes with TX-100, the optical density curve in Figure 2.4a peaks over a narrow range of TX-100 concentrations that correspond to R_{sat}. Moreover, unlike all the previous cases reported here, the peak absorbance is scattered over a range of TX-100 concentrations rather than a single peak value that finally equilibrates to a minimum at $C_{Trit} > 2.0$ -3.0 mM. In concert with turbidity measurements, the DLS data for number and volume distributions (%), as shown in Figure 2.4b (left and right panels respectively), provide information about possible arrangements of DPPG bilayer in association with TX-100. The PSD, in terms of number distribution (%), indicates a single uniform peak corresponding to a hydrodynamic diameter of ~ 98 nm at $C_{Trit} = 0.3$ mM (stage I in Figure 2.4b, left panel). As the detergent concentration is increased to $C_{Trit} = 0.6$ mM, the peak size for the PSD decreases to ~ 88 nm. This can be interpreted as the onset of the formation of mixed micelles–vesicle system which would affect the number-averaged particle size. A further increase in TX-100 concentration to $C_{Trit} = 0.8$ mM leads to the appearance of two peak sizes at ~ 12 and 54 nm (stage II in Figure 2.4b, left panel). Finally, even at very high detergent concentrations ($C_{Trit} = 3.2$ mM), the PSD in Figure 2.4b (left panel) indicates two size peaks at ~ 16 and 50 nm (stage III)).

These observations contradict the existence of only mixed lipid-detergent micelles commonly observed at high detergent concentration regimes for the DPhPC systems studied earlier. To investigate these observations in detail, PSDs in volume distributions (%), in stage I of Figure 2.4b (right panel) reveal the appearance of broader peak sizes spread over ~ 100 - 260 nm at $C_{Trit} = 0.6$ mM.

a)
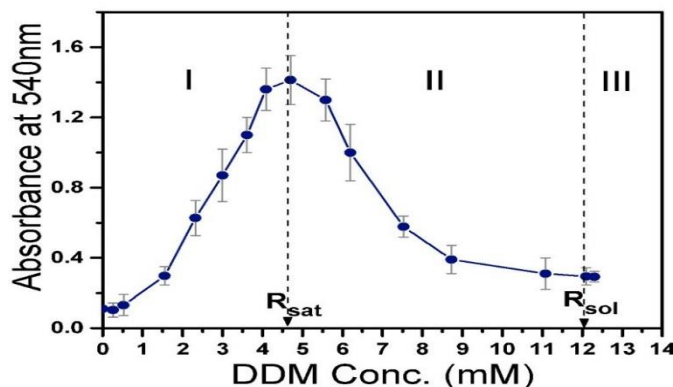
b)

Figure 2.3 Solubilization stages of preformed DPhPC liposomes at 4 mg ml^{-1} concentrations induced by stepwise increase of DDM concentration (mM) as observed with: (a) turbidity measurement; (b, left panel) number distribution from dynamic light scattering (DLS) and (b, right panel) corresponding cryo-TEM micrographs of each stage, indicating: (I) intact liposomes treated with detergent concentration below R_{sat} (C_{DDM} = 4.3 mM); (II) mixed micelle -mixed vesicle structures above R_{sat} (C_{DDM} = 7.0 mM) and, (III) full solubilization of liposomes by detergent molecules and mixed micelle formation around R_{sol} (C_{DDM} = 9.5 mM).

Furthermore, at C_{Trit} = 0.8 mM (stage II in Figure 2.4b, right panel), a large secondary peak appears at ∼ 3850 nm in addition to the peaks at ∼12 and 54 nm seen in Figure 2.4b (stage II, left panel). These large micron-sized peaks persist even at C_{Trit} = 3.2 mM concentration where the absorbance in Figure 2.4a plateaus out. It should be highlighted that these large peak sizes are only observed in volume weighted size distributions and not in the number weighted size distributions, thereby indicating the presence of a relatively small population of larger structures in the abovementioned cases since the number-average particle size are mainly influenced by the larger population of smaller particles. Here, our hypothesis is that the vesicular DPPG liposomes, when solubilized with TX-100, are thermodynamically favored to undergo structural disruption and phase transition into extremely large and more complex network of structures. The increasing formation of these structures is also possibly indicated by the increase in the absorbance value beyond ∼ 3.5 mM that subsequently levels off beyond 4 mM concentration possibly due to the attainment of equilibrium structures.

The aforementioned hypothesis is verified with the aid of cryo-TEM images to understand this anomalous behavior of the process that might be leading to the proposed larger structures with complex morphology. Our results indicate that the regular spherical shaped vesicular liposome structures, with an approximate diameter of ∼ 100 nm in the absence of TX-100 (Figure 2.5a), undergo structural rearrangements upon addition of TX-100 to form a network of complex structures. Here, twisted, dendritic structures with 200–500 nm length are observed (seen from Figure 2.5b) at (C_{Trit} = 0.61 mM). This structural change also agrees well with the peak broadening in the PSD in stage I of Figure 2.4b (right panel).

Upon further increase of detergent concentration (C_{Trit} ∼ 0.75 - 0.8 mM), these twisted dendritic structures unravel to form micron sized cylinders, as seen from Figure 2.5c, that corresponds to the dominant micron sized peak in stage II of Figure 2.4b (right panel). These open cylindrical structures persist even at higher concentration, thereby explaining the existence of the micron-sized peaks in stage III of Figure 2.4b (right panel). To validate the proposed explanation for the abovementioned phenomenon, the vesicle solubilization process is further analyzed using the STEM technique that indeed shows the loss of vesicle structures to twisted tubular structures with inner helical pitch of ∼ 100 nm along with twist interval of ∼ 1150 nm and a diameter of ∼ 180 nm at C_{Trit} = 0.61 mM (Figure 2.5b, inset).
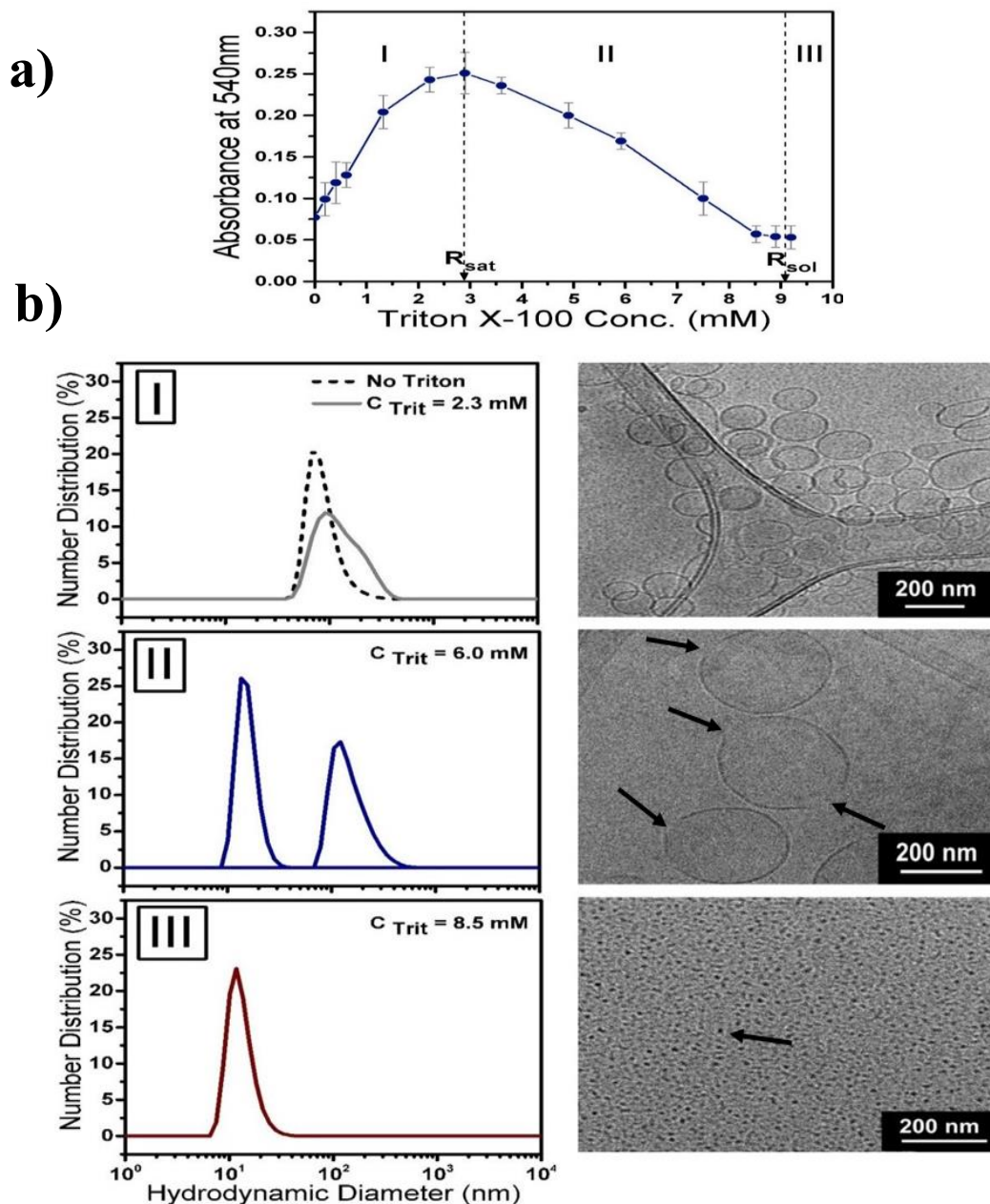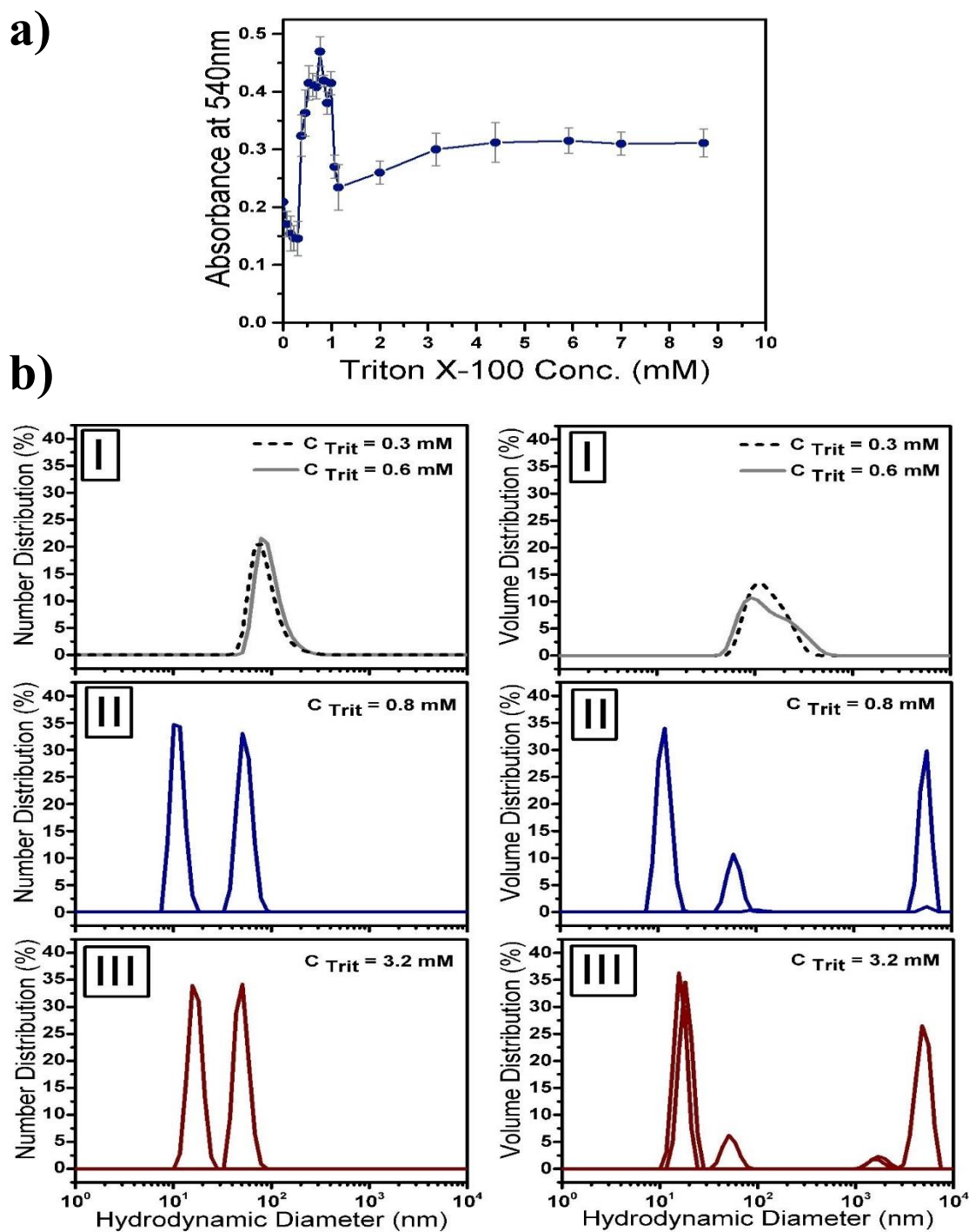
Figure 2.4 Solubilization stages of preformed DPPG liposomes at 4 mg ml^{-1} concentrations induced by stepwise increase of TX-100 concentration (mM) as observed with: (a) turbidity measurement optimized; (b) number distribution (left panel) and volume distribution (right panel) (%) from dynamic light scattering (DLS) measurements for the stages I, II and III.

29

Finally, a further addition of TX-100 (C_{Trit} = 0.8 mM) induces bifurcation of these lipid tubules into long dendritic, helical structures (pitch ∼ 480 nm and diameter ∼ 120 nm) with a filament radius of ∼ 40 nm (Figure 2.5c, inset), which corroborates our cryo-TEM images.

It is noted that the DPPG/ TX-100 interactions at room temperature led to the aforementioned complex structures (as observed via TEM micrograms). In order to investigate the role of kinetics and/or thermodynamics in the formation of these structures, the structural arrangements in the solution were studied at 50°C, above the transition temperature of DPPG at 41°C. DLS data and cryo-TEM images show shift of micron-size structure found at 25°C to smaller structures (17 – 210 nm) at 50°C (refer to appendix IV). Our hypothesis here is that although we started with DPPG lipid in the fluid state, addition of TX-100 causes the system to undergo a phase change and become kinetically trapped at room temperature (25°C), where the complex micron-sized structures formed are not equilibrium structures. Reaction kinetics is partially a function of the stability of the intermediate species (and transition states). To this end, the pathway of a chemical reaction *en route* to its final products has to overcome the transition states. If these intermediates are highly unstable (i.e., highly energetic) relative to the initial reactants, then the initial barrier of activation energy that must be surpassed to set the reaction in motion will be relatively high, and the reaction will tend to proceed slowly (if at all).

In such a scenario, the onward reaction rates for the formation of the final products would be highly retarded, thereby kinetically trapping the intermediate (transition) state. These complex tubular structures represent the transition states and were observed to persist even after 2 weeks (data not shown here). To this end, increasing the temperature to 50°C provides the activation energy required for the vesicle- micelle transition.

It needs to be highlighted here that previous studies on the solubilization of gel phase membranes have identified two distinct situations for solubilizations above and below the transition temperature. Above transition temperature, the various lipids behave similarly, and the respective solubilization data follow the three stage transition model. However, below transition temperature, two scenarios can be detected: 1) when temperature is relatively close to the transition temperature of the pure lipid, were found to be solubilized by TX-100.[124] In fact, these lipids are solubilized by a lower concentration of TX-100 as compared to the bilayers in fluid phase.[125,126] This is due to the co-existance of two phases: a fluid phase and a gel phase.
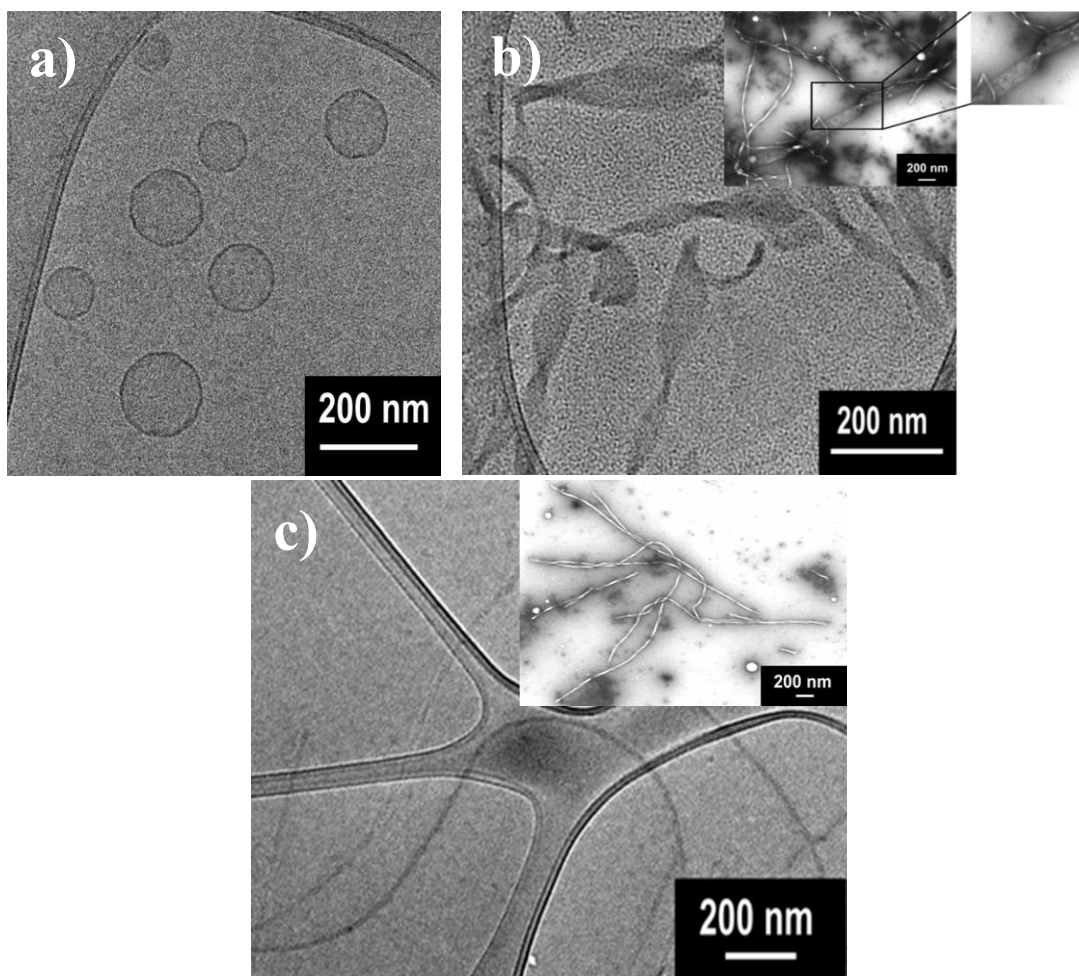
Figure 2.5 Cryo-TEM micrographs along with stained-TEM images (Insets) representing solubilization of preformed DPPG liposomes with TX-100 indicating: (a) intact liposomes in the absence of detergents; (b) transition from vesicular structures to twisted, tubular (ribbon like) structures at C_{Trit} = 0.61 mM, and (c) bifurcation of lipid tubes into long dendritic, helical (or, spiral) structure at C_{Trit} = 0.8 mM.

This mixed phase (liquid-ordered phase) explains many of the unusual material properties of two-phase membranes; 2) when temperatures are well below the transition temperature, lipids in the gel state cannot be solubilized by the detergent.[124,127] Our current results for DDPG/TX-100 system also corroborate these observations wherein, for the same concentration of TX-100, DPPG vesicles were found to be soluble in TX-100 in the fluid state (at ~ 50°C), but were insoluble in the gel state (at 25°C) (refer to Figure appendix IV).

2.3.2.2 DDM Interaction with DPPG.

In continuation with the aforementioned study, the optical density measurements for DPPG, treated with different concentrations of DDM also indicate the familiar three-stage solubilization curve with R_{sat} at C_{DDM} = 0.6 mM and R_{sol} at C_{DDM} = 1.2 mM (stages I, II and III as shown in Figure 2.6a). DLS data also confirm these stages, where the PSD at C_{DDM} = 0.3 mM show a peak size of ~ 85 nm, representing the intact DPPG vesicle size that increase to ~ 100 nm upon addition of DDM (C_{DDM} = 0.6 mM corresponding to R_{sat} in stage I of Figure 2.6a) indicating swelling of the DPPG vesicles (stage I in Figure 2.6b, left panel). In the coexistence region (stage II in Figure 2.6a), the PSDs exhibit a scatter over a size range of < 7 nm (DDM micelle size ~ 5.5 - 6 nm) up to > 45 nm (stage II in Figure 2.6b, left panel). This can be attributed to the mixed vesicle–mixed micelle inter-conversions. Finally, at detergent concentrations above R_{sol} in Figure 2.6a (C_{DDM} = 1.4 mM), the PSD represents peaks ranging from < 2 nm up to > 11 nm, which corresponds to mixed micelle formation (stage III in Figure 2.6b, left panel).

Cryo-TEM images of DPPG solubilization with DDM are found to be in agreement with aforementioned results, where general structure of liposomes remains intact during stage I and II of solubilization as seen from Figure 2.6b (right panel). These images demonstrate a sharp contrast to the results obtained with liposomes titrated with TX-100. During the solubilization, DDM associate with the DPPG bilayer and a general structure of liposomes remain intact at stage I of solublization (see Figure 2.6b, right panel). Bifurcation of lipid and helical or spiral structure arrangement has not been seen at DDM concentrations that are far beyond R_{sat}, (see stage II, right panel) and, even at relatively high detergent/lipid ratios, the lipids still tended to form liposomal structures despite the relatively high concentration of DDM in the bilayers (see stage III, right panel). Mixed micelles are formed upon further increase of detergent concentration beyond R_{sol}, where neither liposomes nor any dendritic structures are observed any longer.
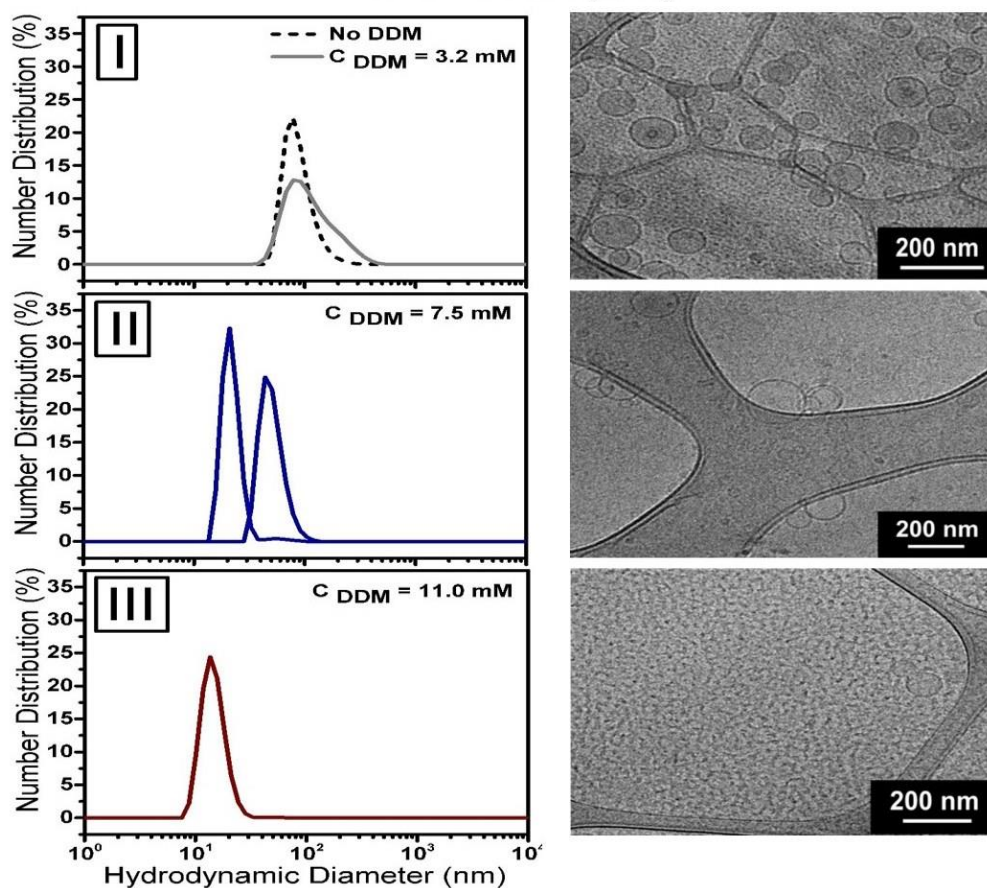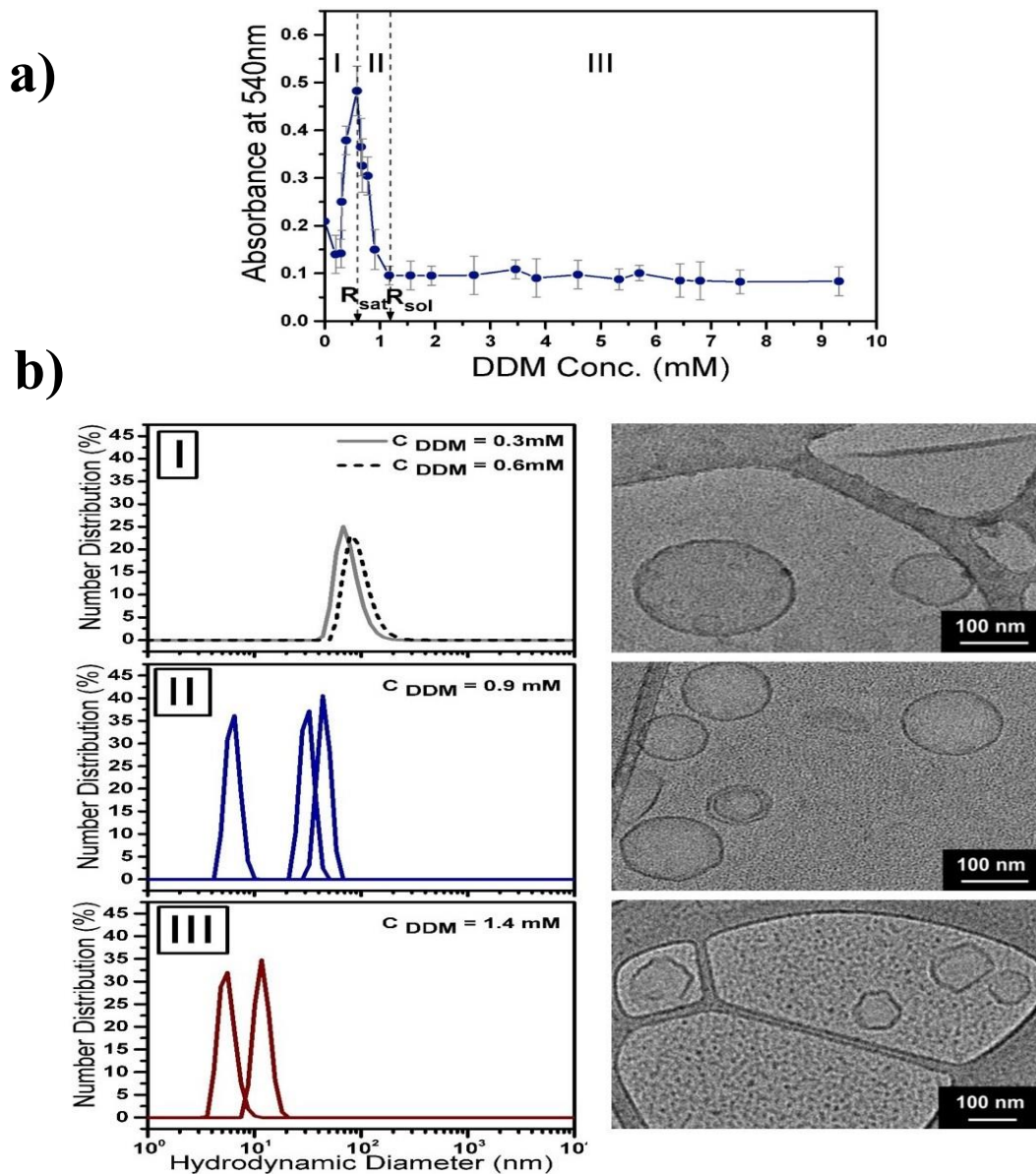
Figure 2.6 Solubilization stages of preformed DPPG liposomes at 4 mg ml^{-1} concentrations induced by stepwise increase of DDM concentration (mM) as observed with: (a) turbidity measurement; (b, left panel) number distribution (%) from dynamic light scattering (DLS) measurements, and (b, right panel) corresponding cryo-TEM micrographs of each stage, indicating: (I) liposome treated with detergent concentration below R_{sat} ($C_{DDM} = 0.4$ mM), where liposome structure remains intact; (II) coexistence stage of solubilization ($C_{DDM} = 0.8$ mM); (III) high population of mixed micelles and smaller liposomes close to R_{sol} ($C_{DDM} = 1.2$ mM).

The faceted morphologies that we see in the TEM images, were reproducible and attributed to the incorporation of detergents into the liposomes in a way that alters their local bending rigidity and curvature. It has been shown that membrane domains enriched in saturated sphingolipids and cholesterol (lipid rafts) show membrane deformation due to the fact that cholesterol induces profound changes in the mechanical properties and conformational states of some types of lipid bilayers.[128,129] This observation is also consistent with studies on solubilization of giant unilamellar vesicles (GUVs) which have shown that some detergents mechanically destabilize the membrane through curvature stress, resulting in curvature-induced instability.[95,130]

2.3.3 Discussion on the Choice of Detergents and Liposomes for Proteoliposome Preparation

The aforementioned characterizations need to be contextualized in the framework of our motivations for the present study, namely the efficacy of membrane protein reconstitution into suitable biomimetic lipid membrane systems. The choices of the lipids studied here are based on: 1) the predominant presence of PG in thylakoid membrane of PSI, and 2) the thermal and structural stability of DPhPC that makes it suitable as highly stable and leak free membranes in membrane-based assemblies.[107] In an effort to explain the rationale behind our choices of the specific lipid membranes, namely DPhPC and DPPG, we dedicate this section to discussing some of the structural and phase characteristics of the aforementioned lipids that, in turn, provides fundamental insight into the interpretation of our results presented here.

The differences in the specific behaviors of how TX-100 partitions into DPhPC and DPPG bilayers can be explained on the basis of the structural differences, as well as the role of electrostatic charge and the thermotropic state of the lipid relative to the transition temperature. To this end, the mismatch between the lateral areas of the headgroups and the hydrocarbon chains of the two lipids under study can provide a plausible explanation to the differences in their solubilization behaviors. While DPhPC has a larger headgroup (volume 319 $Å^3$) than DPPG (volume 257 $Å^3$), the tail groups of both lipids have 16-carbon long hydrocarbon chains that are methyl-branched in the case of DPhPC but has no methyl branches in the case of DPPG. Such branched-chain structures affect the structures of the lipid membranes formed such that DPhPC monolayers exhibit a lateral area per lipid of ~ 80$Å^2$ at 25°C while lipids with similar chain lengths, but devoid of methyl groups, exhibit lower molecular areas (e.g., dipalmitoyl phosphatidylcholinem with 47.4$Å^2$ and dipalmitoleoyl phosphatidylcholine with 65.8$Å^2$) even at

the tightest packing conditions.[131] In contrast, the area/lipid for DPPG in the gel phase (46.7 Å^2 at 25°C) is smaller than that reported for DPhPC.[132] DPPG molecules are able to tightly pack with the tails arranged in a hexagonal fashion at high surface pressure, unlike the DPhPC molecules that are not able to do so due to the head-tail mismatch, causing their tailgroups to be tilted even at high surface pressures.[127,133] Such tightly packed structures for DPPG molecules can possibly explain the inability of TX-100 molecules to effectively solubilize the DPPG lipid bilayers thereby resulting in the complex ribbon-like structures (as seen earlier in Figure 2.5b and Figure 2.5c).

Moreover the electrostatic charge might play a significant role in the differences observed. Recent work of Ahyayauch et al.[134] on solubilzation of dipalmitoylphosphatidylcholine (DPPC) membranes with TX-100 above and below lipid transition temperature shows that TX-100 can solubilize the DPPC bilayers in the gel phase (at 20°C) as well as in fluid phase (at 50°C). Furthermore, these lipid bilayers at gel phase were solubilized by a lower concentration of TX-100 as compared to the bilayers in fluid phase. DPPC, analogous to DPPG, has a 16-carbon long hydrocarbon chain that has no methyl branches. DPPC is also tilted and arranged in a hexagonal lattice in the gel phase, and also has its gel-to-liquid crystalline transition temperature at ~ 41°C. However our results for DPPG/TX-100 system appear to contradict this scenario, where, DPPG vesicles were soluble in TX-100 in the fluid phase but were insoluble in the gel phase. Considering that DPPC has the same head group as DPhPC, the only differences between the two remain in DPPC being a non-ionic lipid while DPPG is an anionic lipid. Hence, the aforementioned differences in solubilization behavior can possibly be attributed to the different electrostatic charge interactions of the two lipids.

Finally, the temperature effects, while influencing the thermal motion of the molecules, are also responsible for the gel-fluid thermotropic transitions in the case of DPPG. Thus, the stable fluid state of DPhPC over wide temperature ranges and the gel-to-fluid phase transitions for DPPG at ~ 41°C might be critical in explaining the variations in the interactions of TX-100 with DPPG above and below the transition temperatures. It needs to be mentioned here that despite the larger and more polar headgroups of DDM molecules as compared to those for TX-100, DDM appears to effectively solubilize the DPPG lipid bilayers. In contrast, TX-100 seems to promote a tighter packing of the lipids that appears to result in a kinetically trapped system not in thermal equilibrium. Our current hypothesis is that the addition of TX-100 to the DPPG vesicle suspensions

may alter the balance between headgroup and hydrocarbon chain interactions to create a transition state of DPPG. In such transition states, the lipids can undergo a denser packing owing to possible tilting of the DPPG headgroups out of the bilayer plane in response to the increasing fluctuation pressure from the hydrocarbon chains.[125,133] In future, a detailed validation of this hypothesis would require a molecular level investigation into the structural arrangements of these systems.

In regards to most membrane protein reconstitutions, the success rates are proven to be low at detergent concentrations below the saturation point R_{sat} where the liposomes are not fully saturated with the detergent molecules [71,92] or above the solubilization point R_{sol}, where protein reconstitution most often results in a greater amount of protein-association with detergent micelles and less reproducible orientation in lipid vesicles [92]. Past literature has reported that protein incorporation in the membrane is highest at stage II (refer to Fig. 1), where detergents disrupt lipid-lipid interactions and enhance the bilayer permeability.[88,90,92,135]

The significant findings from our solubilization studies of DPhPC and DPPG with DDM and TX-100 are summarized in Table 2.2. It highlights the critical morphological characteristics of the liposome structures that indicate the suitable phase windows for protein insertion. Considering that most successful protein incorporations occur in stage II, the aforementioned observations suggest that DDM-destabilized DPhPC liposomes provide the widest detergent concentration range over stage II for protein insertion. The DPhPC/TX-100 system follows it closely as a possible candidate for protein insertions.

Table 2.2 Highlights of the overall significant findings

		R_{sat} (mM)	R_{sol} (mM)	Observed Structure	Possible Window of Protein Insertion
DPhPC	TX-100	2.9	Above 8.0	Regular 3 stage transition	wide window at stage II
DPhPC	DDM	4.7	Above11.0	Regular 3 stage transition	Wider window at stage II
DPPG	TX-100	--------	--------	Irregular structures, kinetically trapped (tubular, helical and spiral)	Inapplicable
DPPG	DDM	0.6	1.2	Regular III stage transition	Narrow window at stage II

The stage II of solubilization with TX-100 is limited between C_{Trit} ~ 2.9 – above 8.0 mM, where the same with DDM extends over C_{DDM} ~ 4.7 mM – above 11.0 mM. Such effects are also observed for solubilizations with different lipid concentrations (refer to appendix V). While the wider insertion window for DDM might be helpful in the easier implementation of proteoliposome preparation, the slightly lower detergent requirements for TX-100 might make the process more efficient and economically viable. Furthermore, the highly irregular structural arrangements arising out of kinetically trapped TX-100/DPPG system at room temperature indicate their uncertainty for successful protein insertion. It needs to be pointed out here that the charges carried by the lipid head groups (DPPG is negatively charged and DPhPC is zwitterionic) cannot substantiate the unique lipid-detergent solubilization behavior for DPPG/TX-100 system. To this end, in spite of both TX-100 and DDM being nonionic detergents, the solubilization of DPPG with DDM does not show the complex structures as observed for the TX-100 case. Studies are currently underway to further investigate the implications of these complex structures in terms of PSI encapsulation process. Finally, our results show that DDM-destabilized DPPG liposomes exhibit a narrower window of detergent concentrations (C_{DDM} ~ 0.6 mM – 1.2 mM) for protein insertion in stage II of the solubilization process.

2.4 CONCLUSIONS

In this article, an in-depth investigation of surfactant-induced membrane solubilization of two phospholipids (DPhPC and DPPG) by two detergents (DDM and TX100) commonly used for protein solubilization is presented. Our results from the current study indicate that DPhPC liposomes maintain their vesicular structures intact at the initial stages of detergent addition. Furthermore, when solubilized with both TX-100 and DDM, the vesicles undergo the typical three-stage transition to the final micellar stages via mixed vesicles-micelles state. Vesicular structure formation is a result of hydration and steric forces upon amphiphiles' head groups. These forces result in a high rotational degree of freedom for the monomers and low aspect ratios during the head group interactions[136], as also observed in the case of the solubilization of DPhPC liposomes. On the other hand, the stereochemistry and molecular structure of amphiphiles might result in the formation of organized supramolecular nanostructures with high aspect ratios. It has been demonstrated that some amphiphiles self-assemble into high aspect ratio structures due to the

presence of one or more chiral carbons and moieties suitable for intermolecular directional interactions, such as hydrogen bonds (often secondary amide groups).[136] Thus, our investigations indicate that although DPPG liposomes self-assemble in vesicular arrangements upon extrusion, the introduction of detergent, specifically TX-100, can cause structural deformation that re-organizes the vesicles into complex network of micro- and nano-structural arrangements of lipid bilayers. These structures are found to be kinetically trapped that can be energetically driven to form mixed micelles upon heating the system above the transition temperature of DPPG ($\sim 41^{\circ}$C). Previous crystallographic structural studies of PSI at 2.5 A° resolution have identified four lipids consisting of three phosphatidylglycerol (PG) molecules and one monogalactosyldiacylglycerol (MDGD) molecule that are largely responsible for the long-term stability and functionality of PSI.[9] In light of the larger PG content in PSI lipid structures, our results for the surfactant-induced membrane solubilization of DPPG lipids provide valuable insight for our future work on developing rational and robust approaches for large membrane protein reconstitution that can lead to successful PSI-proteoliposome formation.

CHAPTER 3

TUNING THE PHOTOEXCITATION RESPONSE OF CYANOBACTERIAL PHOTOSYSTEM I VIA RECONSTITUTION INTO PROTEOLIPOSOMES

This Chapter is based on the submitted paper.

"Tuning the photoexcitation response of cyanobacterial Photosystem I via reconstitution into Proteoliposomes," Hanieh Niroomand, Dibyendu Mukherjee and Bamin Khomami, Scientific Reports, Revision submitted on 9-Dec-2016.[67]

3.1 INTRODUCTION

The quest for green energy has sparked considerable interest in Photosystem I (PSI), the photosynthetic protein complex, that is akin to a nano-scale biological photodiode and enables light-activated charge separation (with nearly 100% quantum efficiency) to facilitate unidirectional electron flow.[1] The robust structural and photoactive electrochemical properties of PSI, a transmembrane protein, makes it an ideal candidate for incorporation into solid state bioelectronic or hybrid photovoltaic devices.[13] But the first step towards the successful fabrication of such bio-hybrid devices call for systematic assembly of oriented and functional PSI onto desired bio-abio interfaces via suitable protein scaffoldings. To this end, one must address the obvious question regarding the role of the natural thylakoid membrane housing of PSI trimeric complex in providing the required structural and functional scaffold to the protein. This had led to a growing interest in membrane reconstitution of PSI complexes to form stable proteoliposomes as the final product. Reconstituted proteoliposomes serve as experimental systems for the study of membrane enzymes[55] and small helical membrane proteins, providing a sample environment that accurately mimics the native membrane environment and properties such as hydrophobic thickness, water concentration gradient and lipid order parameter gradient.[56,57] Hence, our motivation for the present study stems from the desire to attain systematic incorporation of PSI complexes into synthetic membrane-bound structures that mimic the natural thylakoid membrane housing of PSI.

Three dimensional (3D) structures of several membrane proteins such as bacteriorhodopsin,[137] aquaporin,[138] EmrE[139] have been determined using electron crystallography. However, both interactions within the protein as well as between the protein and its environment, influence the protein structure.[140] Thus, synthetic lipid bilayers have been employed as biomimetic environments to enable the structural characterizations of several membrane proteins such as, Gramicidin A,[141] M2 protein from the influenza A virus,[142,143] trimeric structures from membrane-bound proteins involved with eicosanoid and glutathione metabolism,[144,145] and the mercury

transporter MerF.[146] Crystallographic studies of PSI at 2.5 A˚ resolution have identified four lipids consisting of three phosphatidylglycerol (PG) molecules and one monogalactosyl diacylglycerol (MGDG) molecule to be the integral cofactors of the transmembrane parts of PSI.[147] These lipids are considered to be largely responsible for the long-term stability and functionality of PSI.[9] In light of the large negatively charged PG content in PSI lipid structures, it becomes pertinent to design bio-mimetic membranes with high PG lipid contents that can be used for large membrane protein reconstitution.

In the past, our research group has performed successful photocurrent measurements on colloidal chemistry-driven and directed assembly of detergent-bound PSI monolayers on self-assembled monolayer (SAM) substrates.[13,51,53,148] In spite of these efforts, the relatively low levels of photocurrent generation from these systems has increasingly drawn our attention towards the role of natural membrane scaffoldings in PSI trimeric complex in enhancing the efficiency, lifetime and tuning of its photochemistry. Recently, Saboe et al. reconstituted two dimensional (2D) PSI crystals on a tethered bilayer lipid membrane support with intercalated conjugated oligoelectrolyte (COE) units.[58] In another work, Stieger et al. constructed 3D architectures consisting of the redox protein cytochrome c as a molecular scaffold for PSI as the photo-functional matrix element aided by DNA molecules as further building blocks.[64] Both of these studies show significant photocurrent enhancements due to the incorporation and possibly, the confinement of PSI in a biomimetic scaffold. These promising results shed light on the photocurrent enhancements arising from the high packing density and orientation of PSI in these complexly tailored biomimetic scaffolds. Yet, the exact role of the specific membrane scaffolds in driving the enhanced photoactive functionality and near unity quantum efficiency in PSI owing to the conformational changes in its native membrane bound form remains elusive. In our continual effort to investigate the optoelectronic behaviors of PSI confined under different bio-abio interfaces, this study presents a fast and elegant approach to achieve high density PSI encapsulation in synthetic lipid bilayer membranes to constitute PSI-proteoliposomes..

We recently investigated the phase transitions during detergent mediated solubilization of negatively charged 1,2-dipalmitoyl-*sn*-glycero-3-phospho-(1'-*rac*-glycerol) (DPPG) liposomes, a member of the PG lipid family. The highly irregular structural arrangements that arise in this system at room temperature indicates its unsuitability for successful protein insertion.[24] Furthermore, this study unveiled the possibility of 1,2-diphytanoyl-*sn*-glycero-3-phosphocholine

(DPhPC) as a promising lipid candidate for protein insertions.[66] It should be noted that DPhPC is a branched phosphatidylcholine (PC) lipid with high thermal and structural stability.[107]

A significant amount of data has been amassed regarding the binary[149,150] and ternary lipid mixtures[150,151] including the miscibility phase diagrams for several of these systems. However, the majority of these studies have been performed for systems that contain only uncharged lipids. Miscibility studies on lipid mixtures containing charged lipids, in particular binary[152,153] and ternary mixtures of PC with PG[154] have shown that membranes containing charged PG lipids indicate similar phase behavior as membranes containing only uncharged PC lipids. Considering the predominant presence of PG in the natural thylakoid membrane of PSI, we introduce a PG-based lipid as our choice for the study of reconstituted PSI proteins. To this end, in the present study we have chosen to work with DPhPG (1,2-diphytanoyl-*sn*-glycero-3-phospho-(1'-*rac*-glycerol)), a lipid with similar structure and thermotropic state that corresponds to the transition temperature of DPhPC. DPhPG is an anionic lipid with 16-carbon long hydrocarbon chains that are methyl-branched, stable and in fluid state over wide temperature ranges.

The current work involves the systematic incorporation of proteins into DPhPG liposomes. Four basic strategies can be used for the insertion of membrane proteins into liposomes. These include sonication, freeze-thawing, organic solvents, and detergents. The first three methods have significant limitations in efficient proteoliposome reconstitutions that include possible local probe heating during sonication that leads to degradation and denaturation of many membrane proteins. Similarly, organic solvents denature most amphiphilic membrane proteins even though reverse-phase evaporation and solvent injection using organic solvents enable efficient liposome preparations.[77,79] However, since detergents are regularly employed during membrane protein purification processes; hence, detergent mediated solublization has become a preferred route for proteoliposome preparations.[86] To this end, fundamental understanding of the solution phase morphology of membranes during their interactions with detergent that determines the all-important membrane-detergent phase diagrams becomes critical for successful isolation, purification, reconstitution and crystallization of membrane proteins.[72,74,76] Thus, we first investigated the surfactant-induced membrane solubilization of DPhPG by a prototypical non-ionic detergent Triton X-100 (TX-100). Here, for ease of visualization and understanding, we have shown the structural details of both DPhPG and the detergent TX-100 in Figure 3.1.
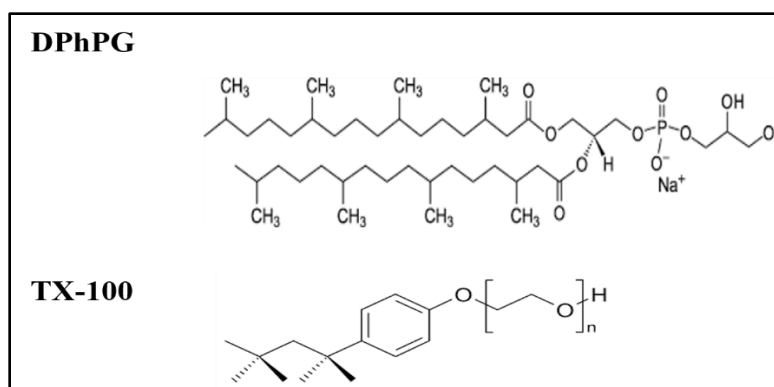
Figure 3.1 Molecular structure of lipid (DPhPG) and detergent (TX-100). DPhPG contains two hydrocarbon chains of 16 carbons with total lipid molecule length of ∼ 2 – 3 nm. TX-100 molecule length is ∼ 3.75 – 4.0 nm.

Isothermal titration calorimetry (ITC) has been classically used as a robust analytical technique for various application such as measuring binding affinities of ligands to membrane proteins,[155] optimizing inhibitor binding in drug discovery,[156] and accessing the partitioning of surfactants into electrically neutral lipid bilayer membranes.[157] In general, ITC is the preferred method for studying interactions between a bioactive molecule (surfactant/peptide/protein) and model lipid membranes.[158-162] In the present work, we have utilized ITC measurements for detecting composition-dependent transitions in lipid-detergent systems. Furthermore, dynamic light scattering (DLS) and cryo-transmission electron microscopy (cryo-TEM) imaging techniques are used to monitor the different stages of stepwise solubilization of liposomes with varying detergent concentrations. Specifically, the composition-dependent equilibrium transitions (phase diagram) of lipid/detergent mixtures is elucidated. Based on previous studies that indicate the occurrence of most successful protein incorporations during the second stage of detergent-mediated solubilization,[88,90,92,135] our prior studies set the backdrop for ideal detergent/lipid concentration ratios for successful protein insertions.

The latter part of our studies will utilize the aforementioned phase diagrams to achieve systematic incorporation of PSI into detergent-destabilized preformed-liposomes at the second stage of solubilization upon subsequent adsorption of detergents using polystyrene beads.[140,150,155] Size-exclusion chromatography (SEC) using high resolution fractionation based on size differences of various complexes has been employed to assure the partitioning of proteoliposomes from individual proteins and/or, excess detergents. Finally, we will confirm the PSI-

43

proteoliposome formation via absorption and fluorescence spectroscopy measurements as well as high-resolution AFM imaging to directly visualize the proteoliposomes supported on gold substrates.

3.2 EXPERIMENTAL SECTION

3.2.1 Materials.

Dibasic (Na_2HPO_4) and monobasic (NaH_2PO_4) sodium phosphate with >99 % assay were purchased from Fisher Scientific, were used to prepare the aqueous buffer solutions of 200 mM Na-Phosphate with pH = 7.0. All aqueous buffer solutions of 200 mM Na-Phosphate were prepared in ultrapure de-ionized (D.I.) water with a resistivity of 18.2 MΩ cm at 25 °C (Millipore, Billerica, MA). Triton X-100 (10 % w/v aqueous solution) was obtained from Anatrace. DPhPG (1,2-diphytanoyl-*sn*-glycero-3-phospho-(1'-*rac*-glycerol)) was purchased as lyophilized powders from Avanti Polar Lipids, Inc. Polycarbonate filters were also purchased from Avanti Polar Lipids, Inc. Lacey carbon-coated (200 mesh) copper grids were purchased from SPI supplies, USA.

3.2.2 Methods.

Growth of *T. elongatus* and preparation of Photosystem I.

The thermophilic cyanobacterium *T. elongatus* BP-1 was grown in 2L airlift fermenters (Bethesda Research Labs, Bethesda MD) in NTA media.[163] The details for the extraction and purification of the trimeric PSI complex from the grown *T. elongatus* cells are provided elsewhere.[51] Based on spectrophotometer measured chlorophyll concentrations, the concentration of the extracted PSI trimers was estimated to be around 1.0×10^{-6} mol L^{-1}. PSI trimers were stored in aliquots of 1.5 mL at -80°C for future use.

3.2.2.1 Liposome Preparation.

4 mg ml^{-1} lipid suspensions were prepared in 200 mM Na-phosphate (pH = 7.0) buffer, followed by 3–4 freeze–thaw cycles to form multilamellar liposomes. These suspensions were then extruded through 100 nm pore sized filter using a mini-extruder (Avanti Polar Lipids) to form unilamellar vesicles at room temperature. The large unilamellar vesicle size of ∼100 nm was confirmed from

dynamic light scattering measurements. Further details regarding the lipid vesicle preparations can be found in previous literature.[164]

3.2.2.2 Titrations of Liposomes with Detergent.

Liposomes suspensions of 4 mg ml^{-1} were titrated by stepwise addition of several aliquots of 10% wt vol^{-1} of TX-100 to the liposome suspension. Detailed technical specifications regarding the physical properties of TX-100 are provided in Table 2.1.[78,92,120] The effect of detergent on the liposomes was monitored using isothermal titration calorimetry.

3.2.2.3 Isothermal Titration Calorimetry (ITC).

A VP-ITC instrument produced by MicroCal Inc. (Northampton, MA) was used. The cell (volume 1.4 ml) was filled with 1 mM or 4 mM DPhPG vesicle suspension. The injection syringe was filled with 300 μl of 77 mM or 154 mM detergent solution, and a series of different volumes of injections were made at 30 min intervals. During each injection, surfactant was incorporated into the lipid membranes, leading to a characteristic heat signal. Integration of the signal yielded the heat change for each injection. The detailed ITC procedure of TX100-mediated solubilization of DPhPG is provided in appendix VI.

3.2.2.4 Dynamic Light Scattering (DLS).

To analyze the liposome size alterations induced by the interaction with the detergent molecules, dynamic light scattering measurements (DLS) were carried out using a 632.8 nm-wavelength Zetasizer (Malvern Instruments). All DLS data were collected using a 178° backward scattering and averaged over four experimental runs each of which were summed up over 12 time correlograms fitted by the Zetasizer software. Due to the presence of bimodal or multimodal size distributions in some phase stages of the solubilization process, the DLS data are represented by more than one curve. All reported sizes are in terms of equivalent spherical hydrodynamic radius as estimated from Stokes–Einstein relation, and all DLS analyses are represented in terms of number distribution. The data analysis was carried out using the effective thermo-physical properties of 200 mM Na-Phosphate aqueous buffer solutions with pH = 7.0.

3.2.2.5 Cryo-Transmission Electron Microscopy (Cryo-TEM).

Cryo-TEM allows direct investigation of samples in their vitrified state at low temperature. The sample preparation for cryo-TEM technique was carried out on 200-mesh carbon-coated holey grids. Before the sample application, a glow discharge was performed in order to hydrophilize the

grid for optimal spreading of the aqueous sample.[123] The suspension was then drop cast onto TEM grids following which the excess sample was absorbed using a filter paper, leaving a thin film of sample in the holes of the grid. Then, the grid was mounted in a Gatan cryo-plunge 3 device and immediately frozen by plunging it in liquid ethane cooled by liquid nitrogen. After vitrification, the frozen-hydrated specimen was inserted into the Gatan cryo-transfer system and transferred into the TEM system. The imaging was carried out by a Zeiss Libra 200 MC TEM equipped with a model Gatan 915 cryo-specimen holder, at an acceleration voltage of 200 kV, and a temperature of about −170 °C under strict low dose conditions (<15 e Å^{-2}). Images were recorded with a Gatan UltraScan 1000XP. Quantitative analyses on more than $n > 30$ particles were used to measure the particle size at each stage of solubilization.

3.2.2.6 Reconstitution of PSI.

Based on ITC measurements and phase diagram appropriate amounts of TX-100 were calculated to solubilize the DPhPG within stage II of solubilization. Subsequently, detergent-mediated protein reconstitution was performed by addition of TX-100 to preformed liposomes (4 mg mL^{-1}). The solution was equilibrated for 60 min, mixed with the solubilized protein in 200 mM Na-Phosphate buffer (pH 7.0), and afterward, the mixture was incubated for 30 min at room temperature under gentle agitation. The final protein-to-lipid weight ratios used for all our studies here (marked as wPLR in all our discussions here) were 0.26, 0.53 and 1.2. For PSI reconstitution, TX-100 was removed by a slow removal procedure in two successive steps, namely, additions of 15 mg Bio-Beads per milligram of TX-100 for 1 h at room temperature and 12 h at 4 °C, followed by an addition of 15 mg Bio-Beads per milligram of TX-100 at room temperature to ensure full detergent removal.[88]

3.2.2.7 Size-Exclusion Chromatography (SEC).

SEC separations were carried out using a Sephacryl S-400 column attached to an AKTA purifier (GE). A total of 200 µl of sample were loaded at a flow rate of 0.5 ml min^{-1}. The sample elution was monitored by optimal wavelengths for liposome and PSI absorbance at 540 and 680 nm, thereby enabling the detection of both PSI and lipids.

3.2.2.8 Absorption Spectroscopy Measurements.

Absorption spectra were recorded at room temperature with a hybrid multi-mode microplate reader (Make: Biotek; Model: Synergy H1). The incubation media contained 200 mM Na-Phosphate at

pH 7.0. Absorption spectra for PSI and proteoliposome suspensions were specifically monitored at ~ 540 and 680 nm (details discussed in Results section).

3.2.2.9 Fluorescence Measurements.

Room temperature fluorescence spectra of the samples were obtained using a multi-mode microplate reader (Make: Biotek; Model: Synergy H1) with 440 nm as the excitation wavelength. The fluorescence emission spectra were measured between 600 and 700 nm.

3.2.2.10 Atomic Force Microscopy (AFM)

AFM topographical characterization for PSI-proteoliposome Au substrates was carried out on commercial gold coated silicon wafers, Au thickness ~ 100 nm (purchased from Platypus Technologies). Gold wafers were cleaned by immersion in isopropanol (99.99% v/v) and de-ionized water for 10 min, and drying in an N_2 stream. Surface immobilization of PSI-proteoliposomes was carried out by drop casting a few microliters of PSI-proteoliposome suspension after size exclusion chromatography on the Au wafers. The monolayer-covered gold wafer was allowed to dry for 1h at 158F and 1h at room temperature and then rinsed in de-ionized water and dried in an N_2 stream. Surface topography images were collected on an AFM instrument (NT-MDT) in the tapping mode using a silicon cantilever compatible with softer biological materials (NT-MDT; Model: NSG03). The tip had a force constant of 0.35–6.1 N m^{-1} along with a resonant frequency of 47-150 kHz.

3.3 RESULTS AND DISCUSSION

This section details our major results for the PSI-proteoliposome formation with the DPhPG/TX-100/PSI system, which can be briefly summarized as follows: 1) Phase diagrams of surfactant induced DPhPG solubilization and 2) Reconstitution of PSI trimers in DPhPG liposomes analyzed with the aid of absorption spectroscopy, fluorescence measurements and atomic force microscopy imaging.

3.3.1 Surfactant Induced DPhPG Solubilization.

Membrane solubilization typically comprises a three-stage process represented by the structural transitions that occur as detergents interact with lipid membranes.[70,73,74,87] As a function of increasing detergent concentrations, the aforementioned stages are: (I) the stage containing

detergent monomers and vesicles wherein detergent monomers start getting incorporated into vesicles; (II) the stage where detergent monomers, mixed vesicles, and mixed micelles coexist (the saturated boundary indicated as R_{sat} in Figure 3.2a); and (III) the final stage that constitutes pure micelles at varying detergent/lipid ratios and detergent monomers (the solubilization boundary indicate as R_{sol} in Figure 3.2a). These three stages of detergent-liposome interactions are identified as a function of increasing detergent concentrations from ITC measurements and depicted in the phase diagrams in Figure 3.2a & b.

Phase diagram of DPhPG/TX-100 mixture in 200 mM Na-Phosphate buffer is shown in Figure 3.2a. Data are collected from two series of ITC solubilization experiments starting with two different lipid concentrations ($\sim$1 mg ml^{-1} and 4 mg ml^{-1}) wherein the R_{sat} and R_{sol} boundaries are as indicated. (Refer to appendix VII for complete phase diagram analysis). Figure 3.2b (top left panel) represents the raw data from the titration of 1 mg ml^{-1} DPhPG vesicles with 77 mM of TX-100 in buffer at room temperature. The three stages of detergent-liposome interactions are identified as vesicles (I), coexistence (II) and micelles (III) in the curve of compensation heat power, Δp (μcal/sec) versus time, t. Figure 3.2b (bottom left panel) represents the heats of injection, Q (kcal/mol) as a function of increasing TX-100 concentrations, C_{Trit} (mM). Figure 3.2b (top and bottom right panel) represent Δp versus time t, and Q as a function of increasing C_{Trit} resulting from the integration of the power peaks obtained from the titrations of 4 mg ml^{-1} DPhPG vesicles with 154 mM TX-100, respectively. The onset of solubilization (R_{sat}) is represented by the drop in Q (exothermic reaction at stage I − II transition), followed by a region of virtually constant Q (stage II). Beyond this region, an increase in Q (stage II-III transition) marks the completion of solubilization (R_{sol}). The R_{sat} and R_{sol} breakpoints read from these curves are included in Figure 3.2a. The significant findings from our solubilization studies of DPhPG with TX-100, namely, the saturation (R_{sat}) and solubilization (R_{sol}) concentrations of TX-100 are summarized in Table 3.1.

Table 3.1 Highlights of lipid/detergent concentrations, saturation (R_{sat}) and solubilization (R_{sol}) concentrations from TX-100 induced DPhPG solubilization

Lipid Concentration (mg/ml)	Detergent Concentration (mM)	R_{sat} (mM)	R_{sol} (mM)
1	77	1.83	4.75
4	154	4.19	15.85
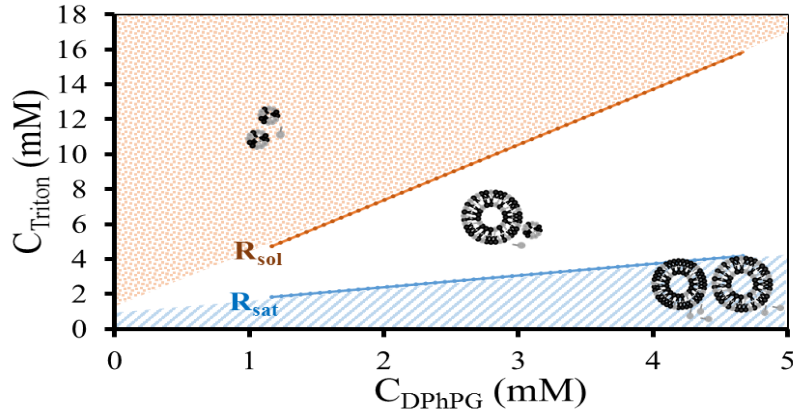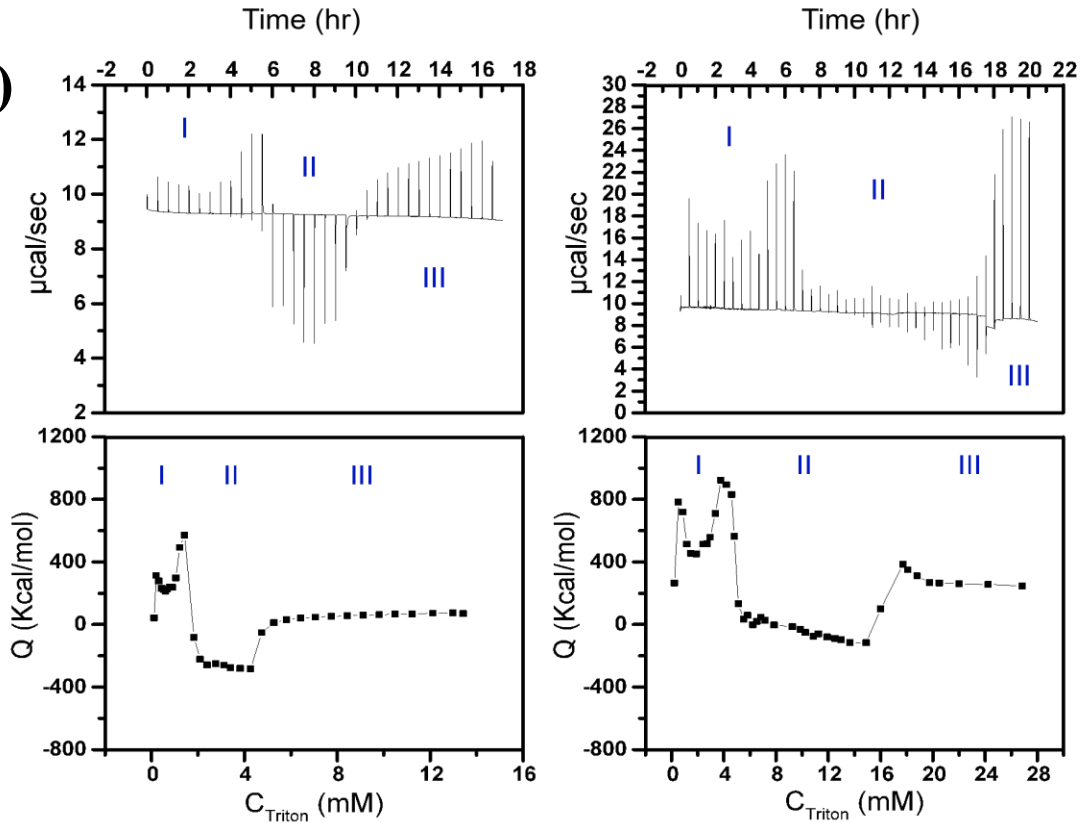
Figure 3.2 Solubilization of preformed DPhPG liposomes induced by stepwise increase of TX-100 concentration. (a) phase diagram of DPhPG/TX-100 mixture in buffer; (b, left panel) solubilization titration of 1 mg ml^{-1} DPhPG liposomes with 77 mM TX-100, Compensation heat power, Δp, versus time, t, on top and heats of injection, Q, as a function of the total detergent concentration, C_{Trit}, on bottom; (b, right panel) solubilization titration of 4 mg ml^{-1} DPhPG liposomes with 154 mM TX-100, Compensation heat power versus time on top and heats of injection as a function of the total detergent concentration on bottom.

Size and morphological variations during the stage II of solubilization are elucidated with cryo-TEM images of liposome structures in their vitrified states (Figure 3.3b & d) as well as DLS measurements (Figure 3.3a & c). Cryo-TEM images for 4 mg mL^{-1} DPhPG liposome solubilization with detergent concentrations ranging between $R_{sat}<$ C$_{Trit}$ $<R_{sol}$ indicate the enlargement in the liposome diameter due to detergent incorporation within the membrane bilayers. Particle size distributions (PSD in terms of number distribution, %) corresponding to solubilization with C$_{Trit}$ = 5 mM indicate two peaks at ~ 150 and 320 nm as compared to the peak size ~ 100 nm for liposomes without any TX-100 (Figure 3.3a). We also observe that these enlarged liposomes coexist with stable open vesicular structures at C$_{Trit}$ ~ 5.0 mM (see Figure 3.3b). This bilayer opening is associated with the rapid solubilization of bilayers by detergents with relatively small polar moiety as in the case of TX-100. Such rapid solubilization is achieved due to detergent molecules interactingfrom both sides of the phospholipid bilayer (transbilayer solubilization) that ultimately makes it permeable and in turn disintegrates into mixed micelles.[89,91,94,95] Upon further increase of detergent concentrations (C$_{Trit}$ ~ 8.0 mM), enlarged vesicles continue to disintegrate into mixed micelles and open vesicular structures with smaller size (~ 30 – 90 nm) as observed from both DLS measurements (Figure 3.3c) and cryo-TEM micrographs (Figure 3.3d). Based on these data, C$_{Trit}$ concentrations were chosen from points within the coexistence region (stage II) of the solubilization phase diagrams in Figure 3.2a to execute our PSI reconstitutions in the liposomes.

3.3.2 Liposome-Based Reconstitution of Trimeric PSI

PSI-proteoliposme reconstitutions were carried out by incorporating TX-100 solubilized PSIs into TX-100 destabilized liposomes at multiple points chosen from within the stage II of solubilization. Following the PSI insertion, the excess detergents were adsorbed by using polystyrene beads. Two points within the stage II of solubilization were chosen: C$_{Trit}$ = 8.0 mM (intermediate part of stage II), and C$_{Trit}$ = 12.0 mM (end of stage II). Protein reconstitution was performed at three weight protein-to-lipid ratios (wPLR) of 0.26, 0.53 and 1.2. Subsequently, size-exclusion chromatography (SEC) fractions were collected prior to any PSI-proteoliposome analysis whereby PSI-proteoliposmes were separated from individual PSIs, small aggregates or excess detergent based on their physical size difference.
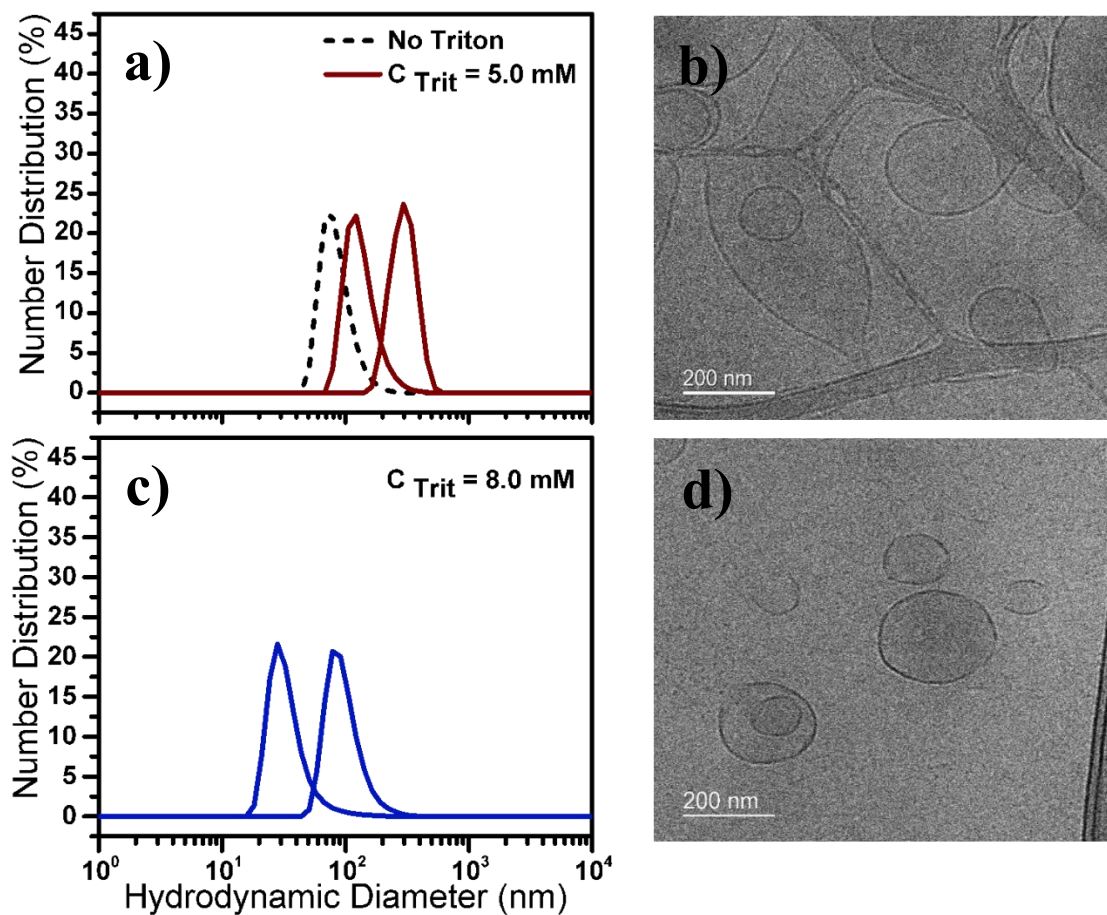
Figure 3.3 Number distribution (%) from DLS measurements (a, c) and corresponding cryo-TEM micrographs (b, d) of preformed DPhPG liposomes during the second stage (stage II) of solubilization with TX-100. Liposomes were treated with different TX-100 concentrations of (a, b) C_{Trit} = 5.0 mM, and (c, d) C_{Trit} = 8.0 mM.

SEC absorbance profiles of the DPhPG liposomes and TX-100 solubilized PSIs acquired at 540 nm (optimal wavelength for liposome absorption) and 680 nm (optimal wavelength for PSI absorption) provide the controls for the PSI-proteoliposome fractionations and are as shown in Figure 3.4a and Figure 3.4b respectively. Shadowed fractions in Figure 3.4b corresponds to detergent micelles. Comparing the SEC elution profiles of PSI-proteoliposomes with TX-100 solubilized PSIs (680 nm profiles in Figure 3.4b) reveals that the PSI-proteoliposomes sample contains no excess detergent micelles due to a lack of an equivalent peak in their chromatogram. Furthermore, SEC elution profiles of PSI-proteoliposomes can be explicitly analyzed from the complete data matrix represented in Figure 3.4c for C_{Trit} = 8 and 12 mM (along rows) and wPLR = 0.26, 0.53 and 1.2 (along columns). It is noted that at wPLR = 0.26, choosing a higher detergent concentration within the stage II for protein insertions results in PSI-proteoliposomes with increasing absorbance intensities (~500 a.u.) for 680 nm (Figure 3.4c, first row). On the other hand, at wPLR = 0.53, the intensities of 680 nm absorbance almost plateau to a consistent value of ~ 1000 a.u. for all three protein addition points at C_{Trit} = 8 and 12 mM cases within the stage II of solubilization (Figure 3.4c, second row). Finally, at wPLR = 1.2, the absorbance intensities for 680 nm indicate an almost consistent value of ~ 1200 a.u. for the different C_{Trit} concentrations (Figure 3.4c, third row). Here, our hypothesis is that once the first PSI is inserted within the bilayer, it disrupts the membrane integrity which essentially lowers the interfacial free energy for subsequent insertions.

Preliminary calculations for number of PSI per liposome in the solution results in 1, 2 and 5 PSI(s) per DPhPG liposome for wPLR = 0.26, 0.53 and 1.2 respectively. A careful inspection of these data in regards to the aforementioned SEC absorbance profiles for PSI-proteoliposomes suggest that at wPLR = 0.26, higher detergent concentrations within stage II for protein insertions result in higher number of liposomes carrying one PSI complex within the suspension. However, upon supplying more PSI proteins to the sample saturates the maximum number of PSIs incorporated within the liposomes. Thus, PSI additions at any point within stage II of solubilization for wPLR = 0.53 and 1.2 results in approximately similar number of liposomes having two or five PSIs respectively. However, the shadowed fractions in the SEC chromatograms of PSI-proteoliposomes at wPLR = 1.2 shows that addition of PSIs at very high concentrations results in PSI-proteoliposomes with higher number of reconstituted PSI as well as individual unassociated PSIs and possibly shredded liposomes present in the sample. Figure 3.5 shows the relative

absorbance intensities at 680 nm for the different PSI-proteoliposomes prepared under different C_{Trit} concentrations and wPLR ratios as derived from the preceding SEC elution steps of purifications. Thus, at wPLR = 1.2, SEC fractions with highest overlapping absorbance intensities at 540 and 680 nm were collected. Afterward, the PSI-proteoliposome formation is characterized mainly by using the intrinsic features of PSI on these fractions.

3.3.3 Absorption spectroscopy of PSI/DPhPG proteoliposomes.

PSI is active over 53% of the solar spectrum with known absorption peaks at around 440 and 680 nm contributed by Chlorophyll *a* (Chl *a*), and shoulders at around 475 and 650 nm originating from Chl *b* in the light-harvesting complexes.[165] Changes in the amplitude and wavelength shifts of absorption peaks of control PSI solution and reconstituted PSI suspension, is a good qualitative indicator of alteration in the microenvironment around the Chl *a* or Chl *b* molecules of PSI. Such qualitative indications of proteoliposome formation has also been demonstrated by earlier studies.[166]

The room temperature absorption spectra of TX-100 solubilized PSI solution in Figure 3.6 demonstrates the signature peaks of PSI at 440 and 680 nm. The aforementioned peaks are absent in the absorption spectra of control DPhPG suspension. The absorption spectra of PSI-proteoliposome suspension (formed by PSI addition at the aforementioned two points in stage II) shows a significant blue shift in the blue region (peak shift from 440 to 418 nm) and a slight blue shift in the red region (peak shift from 680 to 674 nm). This blue shift is attributed to modification of the microenvironment around Chl *a* molecules within PSI-proteoliposomes (Figure 3.6, left panel). Figure 3.6, right panel shows the room temperature absorption spectra collected for pure DPhPG liposome suspensions devoid of PSI after undergoing identical treatments of detergent removal. The data clearly confirms that the blue shifts arise from PSI-proteoliposme formations and are not an artifact from other microenvironment alterations, such as presence of TX-100 detergent molecules.

3.3.4 Florescence spectroscopy of PSI/DPhPG proteoliposomes.

Detailed analysis of the peaks from fluorescence emission spectra can provide indications of the oligomeric states of PSI complexes, where the characteristic emission peaks of monomeric and trimeric PSIs are located at ~730 and 760 nm, respectively.
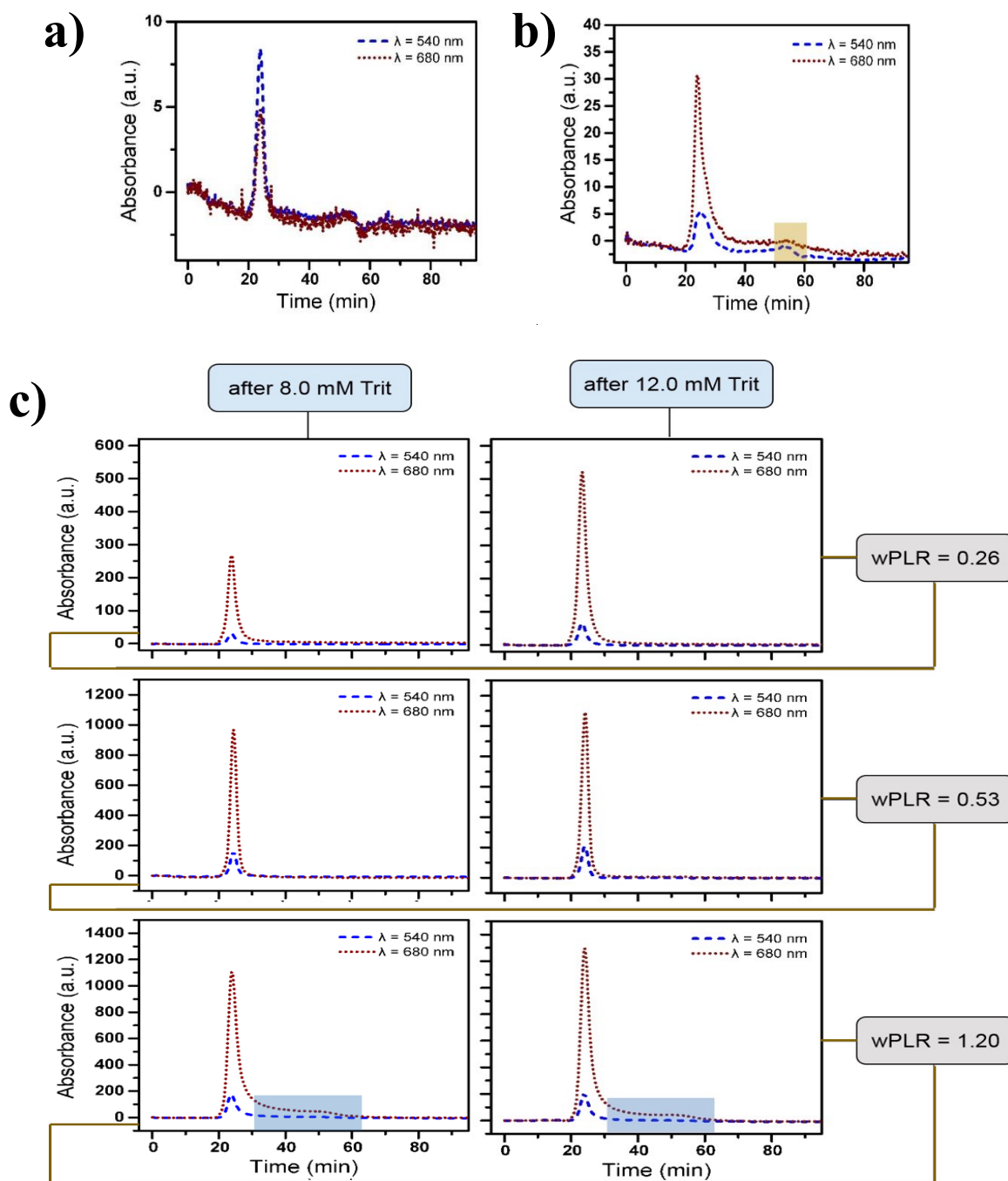
Figure 3.4 SEC elution profiles of: (a) control DPhPG liposomes; (b) TX-100 solubilized PSI; and (c) PSI-proteoliposomes based on optimal wavelengths of absorbance at 540 (blue dashed lines) and 680 nm (red dot lines) for liposomes and PSI respectively. Shadowed fractions in (b) corresponds to detergent micelles. Shadowed fractions in (c) for PSI-proteoliposomes at wPLR = 1.2 correspond to individually unassociated PSIs or shredded liposomes.
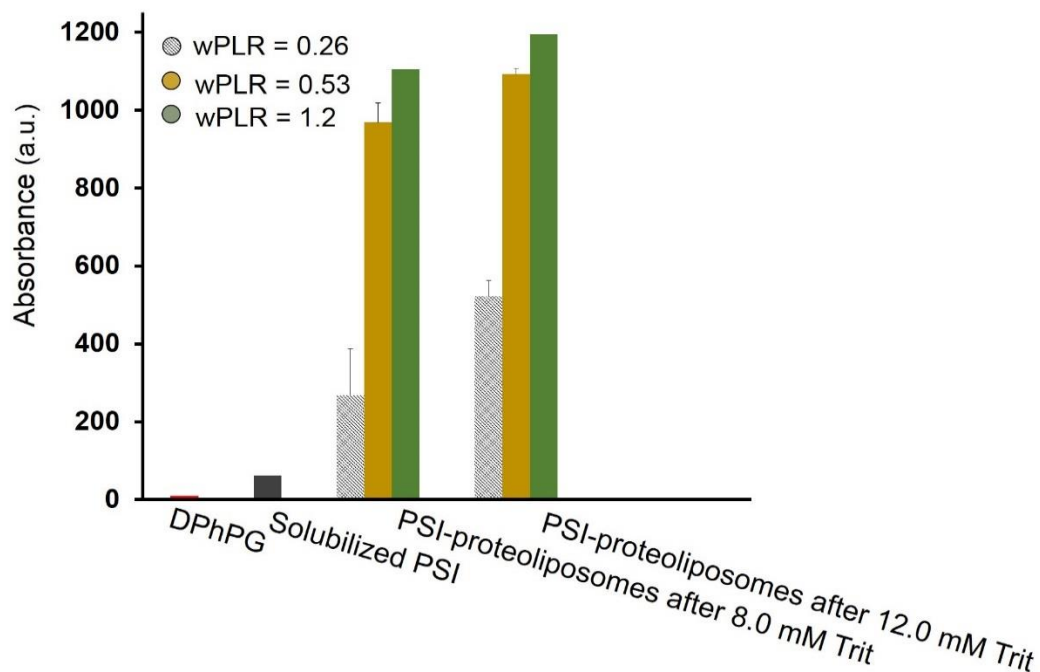
Figure 3.5 Comparisons of the maximum absorbance intensities at 680 nm as obtained from the SEC elution profiles in Figure 3.4.
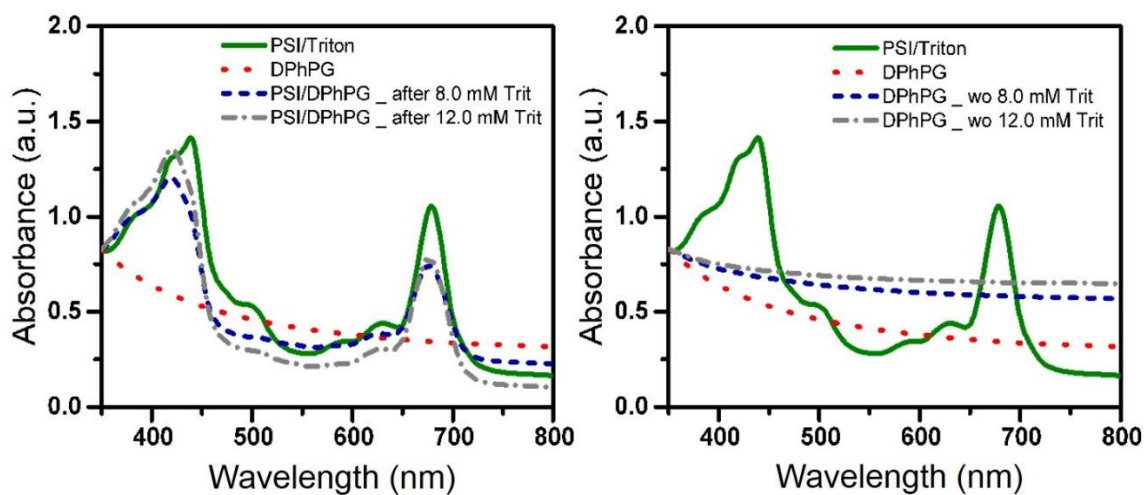
Figure 3.6 Room temperature absorption spectra of DPhPG liposomes, solubilized PSI and PSI-proteoliposomes with left panel indicating PSI/DPhPG reconstituted at different point of second stage of solubilization and right panel indicating DPhPG liposome suspensions after detergent removal.

This arises from an intriguing property of PSI due to the presence of the so-called red antennae Chls. In particular, cyanobacteria contain relatively high amounts of this red Chl that show absorptions at a longer wavelength than the reaction center P700 itself. The amount of red Chls varies among various species of PSI.[167-169] Although monomers and trimers comprise similar set of Chl forms, only the trimers contain an extremely red shifted Chl, which gives rise to a 760 nm fluorescence emission peaks at low temperature (77K).[170,171] Moreover, this method can be used as a complementary qualitative method for the evaluation of successful proteoliposome formations.[105] To this end, appearance of an emission peak at 680 nm can be indicative of uncoupled Chls[170,172,173] which is typically considered as a marker for the proteoliposome formation.

Fluorescence emission spectra of control PSI (without detergent), PSI/detergent solutions as well as pure DPhPG suspensions at room temperature are shown in Figure 3.7. Florescence emission spectra of PSI solution, both in presence and absence of detergent, indicate a small emission band at around 680 nm (750 and 500 florescence counts, respectively). As expected, the emission band at 680 nm is not observed in the case of the pure liposome suspensions. After PSI incorporation, the proteoliposomes were further characterized by florescence emission spectroscopy at room temperature as shown in Figure 3.8. Figure 3.8 (left panel) shows florescence emissions from proteoliposome suspensions after PSI- reconstitution of detergent-destabilized DPhPG liposomes. Emission spectra of PSI-proteoliposomes formed from protein insertions at the intermediate ($C_{Trit} \sim 8$ mM) and end ($C_{Trit} \sim 12$ mM) of stage II of solubilization indicates 12 and 14 times enhancements respectively in their florescence intensities as compared to the control PSI case. Thus, choosing the protein addition point at higher detergent/lipid ratio within stage II of solubilization, results in more significant modification of the microenvironment around Chl *a* molecules within proteoliposomes. Enhanced florescence intensity at 680 nm is observed for the TX-100 mediated proteoliposome suspension further confirming the successful proteoliposome formation. Lack of a peak at 680 nm in the fluorescence emission spectra of DPhPG liposomes suspension after identical treatments detergent removal (Figure 3.8, right panel) further corroborates our hypothesis that observed Chl uncoupling is due to the proteolipose formation. Also, the aforementioned studies provide evidence that protein confinement as a result of the synthetic lipid scaffold enhances the activity of protein.
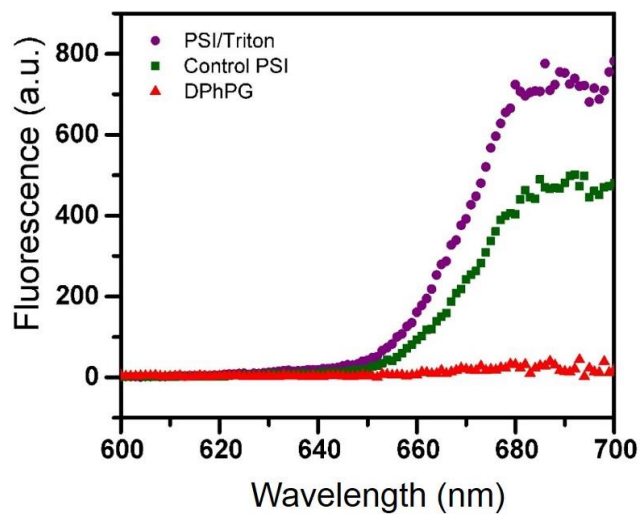
Figure 3.7 Room temperature fluorescence emission spectra of DPhPG liposomes, TX-100 solubilized PSI, and control PSI suspensions.
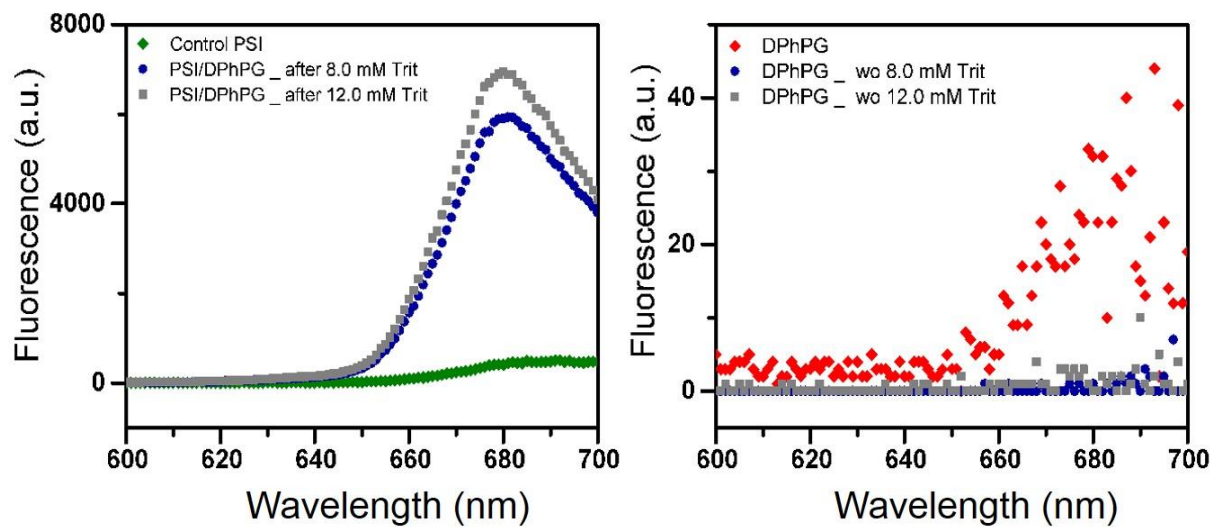
Figure 3.8 Room temperature fluorescence emission spectra of: (left panel) control PSI and PSI-proteoliposomes reconstituted at different point of second stage of solubilization; (right panel) control DPhPG liposomes and DPhPG liposomes suspension after detergent removal.

3.3.5 Atomic force microscopy of PSI/DPhPG proteoliposomes.

A droplet of suspension after SEC column was drop cast on the gold wafers as mentioned in the methods section. AFM topographical characterization of this sample further confirms the successful PSI-proteoliposome formation. For ease of visualization, highly dilute samples from the SEC elution profiles were drop cast on to the substrates to create sparsely located supported collapsed bilayers. The AFM image of suspension treated gold substrate depicted in Figure 3.9a shows two immobilized liposomes on the Au surface and barely any individual PSI. Zoomed-in AFM images in Figure 3.9b clearly show serval membrane-bound PSIs as well as membrane-adsorbed PSIs as also indicated from the SEC elution profiles for the case studies with wPLR = 1.2 in Figure 3.4c.

Detailed cross-sectional surface profiles from the aforementioned AFM image of supported liposomes have been reported in Figure 3.9b, right panel. The cross-sectional profiles indicated an average bilayer height of $h_1 = 5$ nm (shown with arrows marked on Figure 3.9b) as expected for the lipid bilayer system. Furthermore, surface profiles of the immobilized liposome show an average height of $h_2 = 2$ nm as well as average dimeter of $d_2 = 30$ nm, which represent membrane-bound PSI and an average height of $h_3 = 8.5$ nm as well as average diameter of $d_2 = 50$ nm, which represent membrane-adsorbed PSI.

3.4 CONCLUSIONS

Considering the large negatively charged PG content in thylakoid membrane of PSI, we aim to introduce a choice of PG lipid for the study of reconstituted PSI proteins and subsequently systematically incorporate PSI complexes into synthetic membrane-bound structures that mimic the natural thylakoid membrane housing of PSI. Specifically, the current study presents the surfactant-induced membrane solubilization of a negatively charged phospholipid DPhPG by TX-100 commonly used for protein solubilization. Our results indicate that DPhPG liposomes maintain their vesicular structures intact at the initial stages of detergent addition. Furthermore, when solubilized with TX-100, the vesicles undergo the typical three-stage transition to the final micellar stages via mixed vesicles-micelles state. Based on the phase diagram obtained from the solubilization analysis, ideal concentration ratios for successful protein insertion were chosen and PSI complexes were incorporated into detergent-destabilized preformed-liposomes at various points of stage II of solubilization, using polystyrene beads to adsorb the detergent.
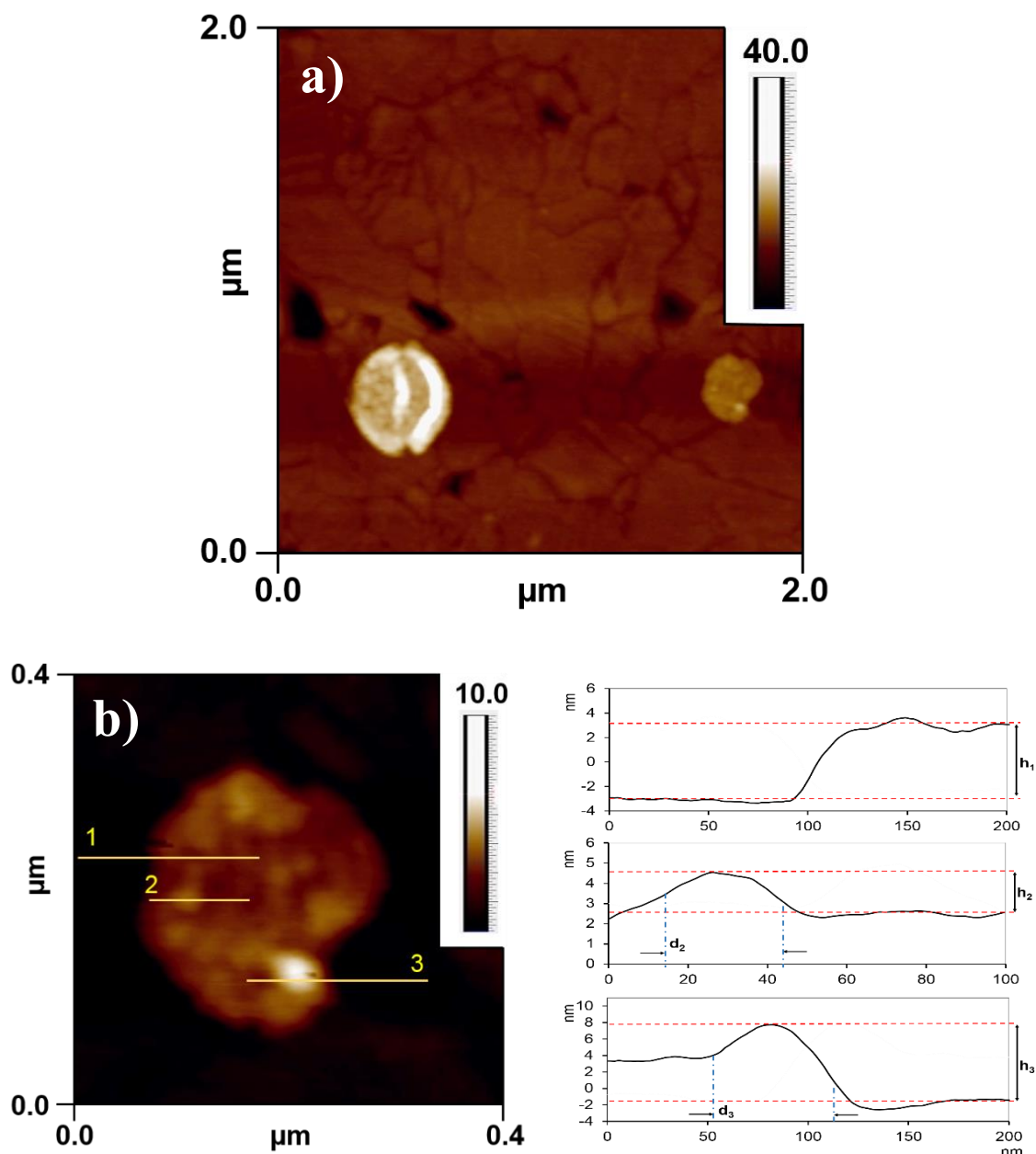
Figure 3.9 AFM images of the PSI-proteoliposomes supported on gold surfaces. (a) Bare gold substrate and PSI-proteoliposomes; (b) zoomed in images of PSI-proteoliposomes and representative cross-sectional surface profiles (1) for lipid bilayer assembled on gold surface ($h_1 \sim$ 5 nm); (2) for membrane-bound PSIs ($h_2 \sim 2$ nm, $d_2 \sim 30$ nm) and (3) for membrane-adsorbed PSI ($h_3 = 8.5$ nm, $d_3 = 50$ nm) are shown for the respective AFM image.

Successful PSI-proteoliposome formation was analyzed via absorption and fluorescence spectroscopy measurements and atomic force microscopy. A clear signature for successful PSI-proteoliposome formation is observed when a significant blue shift in the blue region (peak shift from 440 to 418 nm) and a slight blue shift in the red region of absorbance spectra and enhanced florescence intensity at 680 nm is observed for the TX-100 mediated proteoliposome suspension. AFM topographical characterization of supported liposomes revealed serval membrane-bound PSIs as well as membrane-adsorbed PSIs, further stablishing the successful PSI-proteoliposome formation. Such observations throw light on the alterations in chromophore-chromophore interactions and Chl *a* photoexcitation (as indicated by the enhanced 680 nm fluorescence emissions) owing to microenvironment changes arising from PSI confinement within fabricated proteoliposome structures. In turn, the current study paves the path for optimal tuning of photochemical responses of PSI complexes through rationally designed synthetic bilayer membrane confinements that mimic the natural thylakoid membrane housing of PSI.

CHAPTER 4

PHOTOCURRENT ENHANCEMENT FROM BIOMIMETIC RECONSTRUCTS OF PHOTOSYSTEM I-PROTEOLIPOSOMES SUPPORTED ON ELECTRODE SURFACES

This Chapter is based on the paper in preparation.

"Photocurrent enhancements from biomimetic reconstructs of Photosystem I-proteoliposomes supported on electrode," Hanieh Niroomand, Ravi Pamu, Dibyendu Mukherjee and Bamin Khomami.

4.1 INTRODUCTION

Natural oxygenic photosynthetic processes have been an inspiration for biomimetic and highly efficient solar to chemical energy conversion systems. To this end, several attempts have been made to reconstruct bio-hybrid photoelectrochemical conversion devices via optimal interfacing of inorganic electrodes with Photosystem I (PSI), the transmembrane trimeric protein complex responsible for the photoactivated charge separation with near unity quantum efficiency during natural photosynthesis.[174] In recent years, a flurry of research has been focused on strategies for immobilizing PSI onto conductive material (gold, titanium oxide, silicon, graphene, or gallium (III) arsenide (GaAs), carbon nanotubes (CNTs) or other nanoparticles, and redox polymers).[14-16,18-23,175] Furthermore, efforts have also been directed toward the genetic mutation of PSI to enable direct wiring of PSI to electrodes in order to fabricate efficient PSI-based bio hyrbid photo-sensors.[36-38,49,176] In spite of the large volume of work on the various chemical and inorganic routes to attach PSI to electrode substrates, mostly these works have relied on the use of some form of self-assembled monolayers (SAMs) of organothiol-based compounds to immobilize PSI films onto metal surfaces (mostly gold).[40,42-44,50,52-54] Thus, these efforts have been largely effective in depositing dense monolayers or multilayers of PSI with limited success in preferential orientation of PSI and high photocurrent generation from these systems. Although such efforts are commendable, a significant knowledge gap exists in the reliable verification of the orientation, long-term functionality and photoactivity of PSI to enable light-activated charge transfer with near unity quantum efficiency on these SAM-based assemblies outside of its natural thylakoid membrane housing. Such observations, in turn, have increasingly drawn attention towards the role of the natural thylakoid membrane scaffoldings in enhancing the efficiency, orientation, lifetime and detailed photochemistry of the PSI trimeric complex deposited on various materials.

The efficient electron transfer between the oxidized and reduced redox partners of PSI occurs on opposite sides of the thylakoid membrane (namely the stromal and the lumenal sides), thereby ensuring the protein orientation, while the specific protein conformation within the thylakoid

membrane ensures the optimal stereochemistry for the inter-chromophore excitation energy transfer pathways.[11] Hence, the first step towards the successful fabrication of bio-hybrid devices capable of high photocurrent generation calls for systematic assembly of oriented and functional PSI onto the desired bio-abio interfaces via suitable biomimetic protein scaffoldings. To this end, the current state of research in this area invokes the obvious question: *Do membrane confinements of PSI complexes serve a functional role apart from providing the structural scaffolds for the protein?* To this end, developing on membrane reconstitution of PSI complexes to form stable proteoliposomes as the final product has become of great interest.

Typically, reconstituted proteoliposomes serve as experimental systems for the study of membrane enzymes [55] and small helical membrane proteins, providing a sample environment that accurately mimics the native membrane environment and properties such as hydrophobic thickness, water concentration and lipid order parameter gradients.[56,57] In the context of our present study on reconstituted PSI, emerging studies include a recent work by Saboe et al. where PSI has been reconstituted in a two-dimensional crystal with tethered bilayer lipid membrane support that indicated a 4-fold photocurrent enhancement through the incorporation of conjugated oligoelectrolytes (COEs) units in this device [58]. In addition, photo-bioelectrochemical impact of a series of COEs directly incorporated into thylakoid bioanodes where up to 2.3-fold improvement in amperometric photocurrent density generation has been reported.[62] Moreover, enhanced photocurrent in PSI stabilized in and on a block copolymer support assembled on SAM/gold electrodes in the presence of COEs has also been reported.[63] In line with these works, recent efforts have constructed three-dimensional architectures comprising the redox protein cytochrome c (cyt *c*) as a molecular scaffold for PSI acting as the photo-functional matrix element and DNA molecules as the further building blocks [64] on transparent mesoporous indium tin oxide (μITO) electrodes. Specifically, this construction resulted in an internal quantum efficiency (IQE) of ~39% which is one of the highest values reported for PSI assemblies on inorganic electrodes. One of the interesting aspects of this study is the postulation that such high IQE is due to the high protein loading leading to efficient electron pathways inside 3D transparent conducting oxides.[65] The aforementioned studies indicate significant photocurrent enhancements due to the incorporation and possibly, the confinement of PSI in biomimetic scaffolds. Such promising as well as intriguing results shed light on the photocurrent enhancements arising from the high packing density and orientation of PSI in these complexly tailored biomimetic scaffolds. Yet, the exact role of the

specific membrane scaffolds and microenvironment alterations in driving the enhanced photoactive functionality and near unity quantum efficiency in PSI owing to the conformational changes in its native membrane bound form remain unclear. Specifically, these studies leave us with the unanswered question regarding the biophysical role of membrane confinements in driving the optoelectronic dynamics and charge transfer properties within PSI.

Our main motivation in the present study stems from the desire to attain systematic incorporation of PSI complexes into synthetic membrane-bound structures that mimic the natural thylakoid membrane housing of PSI. The central hypothesis behind this motivation is that PSI confinements in biomimetic membrane frameworks will allow us to tune inter-chromophore electronic coupling within the protein complex by many orders of magnitude through the optimization of chromophore separation and orientation. This is expected to promote photo-excited chromophore-chromophore energy transfer within the PSI and in turn, enhance photocurrent generation. To this end, as the first step towards investigating the optoelectronic behaviors of PSI confined under different bio-abio interfaces, the current study focusses on high density encapsulation of PSI in synthetic lipid bilayer membranes to constitute PSI-proteoliposomes followed by their immobilization onto bio hybrid electrodes and characterization of the photoelectrochemical response of the system. Specifically, the current work reports a detailed investigation of photocurrent enhancements due to PSI confinement in DPhPG (1,2-diphytanoyl-*sn*-glycero-3-phospho-(1'-*rac*-glycerol)) liposomes assembled on specific alkanethiolate SAM (self-assembled monolayer)/Au surfaces.

4.2 EXPERIMENTAL SECTION

4.2.1 Materials.

Dibasic (Na_2HPO_4) and monobasic (NaH_2PO_4) sodium phosphate with >99 % assay were purchased from Fisher Scientific, were used to prepare the aqueous buffer solutions of 200 mM Na-Phosphate with pH = 7.0. All aqueous buffer solutions of 200 mM Na-Phosphate were prepared in ultrapure de-ionized (D.I.) water with a resistivity of 18.2 MΩ cm at 25 °C (Millipore, Billerica, MA). Triton X-100 (10 % w/v aqueous solution) was obtained from Anatrace. DPhPG (1,2-diphytanoyl-*sn*-glycero-3-phospho-(1'-*rac*-glycerol)) was purchased as lyophilized powders from Avanti Polar Lipids, Inc. Polycarbonate filters were also purchased from Avanti Polar Lipids,

Inc. Carbon coated (400 mesh) copper grids were purchased from SPI supplies, USA. Gold coated silicon wafers, Au thickness ~ 100 nm were purchased from Platypus Technologies.

4.2.2 Methods.

4.2.2.1 Growth of *T. elongatus* and Preparation of Photosystem I.

The thermophilic cyanobacterium *Thermosynechococcus elongates* BP-1 was grown and extracted from thylakoids according to Kern et al.[177] The details of the extraction and purification of the trimeric PSI complex from the grown *T. elongatus* cells are provided elsewhere.[64] Based on spectrophotometer measurement of chlorophyll concentration, the concentration of the extracted PSI trimers is estimated to be around 20.0×10^{-6} mol L^{-1}.

4.2.2.2 Liposome Preparation.

4 mg ml^{-1} lipid suspensions were prepared in 200 mM Na-Phosphate (pH = 7.0) buffer, followed by 3–4 freeze–thaw cycles to form multilamellar liposomes. These suspensions were then extruded through 100 nm pore sized filter using a mini-extruder (Avanti Polar Lipids) to form unilamellar vesicles at room temperature. The large unilamellar vesicle sizes of ~100 nm were confirmed via dynamic light scattering (DLS) measurements. Further details regarding the lipid vesicle preparations can be found in previous studies.[164]

4.2.2.3 Negative-Staining Electron Microscopy (NS-EM).

Negative staining was used to facilitate electron microcopy imaging by embedding and supporting a thin layer of biological sample by a dried layer of heavy metal-containing salt, thereby increasing the contrast of biological material with their surroundings without causing structural alteration.[43, 44] A sequential two-droplet method was used for negative staining. Aliquots (~ 5 µl) of the lipid/detergent in buffer suspensions were adhered to thin carbon-coated 400-mesh copper grids that were glow-discharged for 20s to render them hydrophilic. The suspension was incubated for 1 min at room temperature. Excess sample solution was removed by blotting with a filter paper touched to the edge of the grid. After removing the excess fluid, the grid was stained with 1% (w/v) uranyl acetate (UAC) at pH = 3.0 for 60s. In turn the grid was dried at room temperature. Negatively stained specimens were examined with the Zeiss Auriga FIB-SEM microscope operated at 30 kV in STEM mode.

4.2.2.4 Reconstitution of PSI.

Detergent-mediated protein reconstitution was performed by addition of a prototypical non-ionic detergent Triton X-100 (TX-100) to preformed liposomes (4 mg mL^{-1}) (see chapter.3).[66] The solution was equilibrated for 60 min, then mixed with the solubilized protein in 200 mM Na-Phosphate buffer (pH 7.0), and afterwards, the mixture was incubated for 30 min at room temperature under gentle agitation. The final protein-to-lipid weight ratios used for all our studies (protein to lipid weight ratios or wPLR) were 1.2. For PSI reconstitution, TX-100 was slowly removed by a two-step procedure, i.e., addition of 15mg Bio-Beads per milligram of TX-100 for 1 hour at room temperature and 12 hours at 4°C, followed by an addition of 15 mg Bio-Beads per milligram of TX-100 at room temperature to ensure full detergent removal.

4.2.2.5 Preparation of Alkanethiolate SAM/Au Substrates.

Commercial Au coated Si wafers (Au layer thickness ∼10 nm, Platypus Technologies) were dipped in freshly prepared Aqua Regia (concentrated HCl and HNO$_3$ acids in volumetric ratio of 3:1 respectively) prior to adsorbing thiols onto the surface. Freshly cleaved Au substrates (Au thickness ∼60–70 nm) were then immersed in 5 mM ethanolic solution of 4-mercaptobutyric acid (HS–C$_3$H$_6$–COOH, Sigma–Aldrich), 4-Mercapto-1-butanol (HS-C$_4$H$_8$-OH, Sigma–Aldrich) and 6-Mercapto-1-hexanol (HS-C$_6$H$_{12}$-OH, Sigma–Aldrich) for 7 days at room temperature in a chamber filled with inert dry N$_2$. Thiolated Au substrates were washed in isopropanol (Electronic grade residue free; 99%), de-ionized water, and finally dried under a stream of dry N$_2$. Monolayer formation was confirmed by measuring the thiol thickness on Au substrates at multiple spots using spectroscopic ellipsometer and was determined to be 0.53 ± 0.09 nm, 0.46 ± 0.16 nm and 0.62 ± 0.08 nm for C$_4$-COOH, C$_4$-OH and C$_6$-OH respectively.

4.2.2.6 PSI-Proteoliposome Deposition on the Alkanethiolate SAM/Au Substrates.

150 µl of protein-lipid suspensions were drop cast on the alkanethiolate SAM/Au substrates and incubated for 1 hour at 45°C. In turn, the samples were left at room temperature to cool for 1hour, thereby allowing the surface assembly of PSIs incorporated within the supported lipid bilayers (PSI-SLB). Subsequently, PSI-SLBs were washed several times at room temperature with Na-Phosphate buffer and de-ionized water. Then, size-exclusion chromatography fractions were collected using a Sephacryl S-400 column attached to an AKTA purifier (GE). A total of 200 µl of sample was loaded at a flow rate of 0.5 ml min^{-1}. The sample elution was monitored by optimal

wavelength for liposome and PSI absorbance at 540 and 680 nm, thereby enabling the detection of both PSI and lipids.

4.2.2.7 Atomic Force Microscopy (AFM).

AFM topographical characterization for PSI-proteoliposome Au substrates was carried out on commercial gold coated silicon wafers, Au thickness ~ 100 nm. Gold wafers were cleaned by immersion in isopropanol (99.99% v/v) and de-ionized water for 10 min, and drying in an N_2 stream. Surface immobilization of PSI-proteoliposomes was carried out by drop casting a few microliters of PSI-proteoliposome suspension after size exclusion chromatography on the Au wafers. The monolayer-covered gold wafer was allowed to dry for 1hour at 158°F and 1hour at room temperature and then rinsed in de-ionized water and dried in an N_2 stream. Surface topography images were collected on an AFM instrument (NT-MDT) in the tapping mode using a silicon cantilever compatible with softer biological materials (NT-MDT; Model: NSG03). The tip had a force constant of 0.35–6.1 N m^{-1} and a resonant frequency of 47-150 kHz.

4.2.2.8 Electrochemical and Photoelectrochemical Characterization.

Electrochemical measurements were conducted using a bi-potentiostat (Make: Bio-Logic; Model: SP-200) operated using the EC-Lab software. A glass electrochemical cell with three-electrode configurations was used that carried a Pt wire counter electrode, a Ag/AgCl (sat. KCl) reference electrode (BAS Inc.; Model: MF-2052 with a reference shift +0.197 V vs. NHE) and a Au substrate as the working electrode with the specific surface treatments (i.e., SAM/Au, and PSI as well as PSI-SLB on SAM/Au electrodes). Except where specified, all electrochemical measurements were carried out in 200 mM Na-phosphate aqueous buffer (pH = 7.0) as the standard electrolyte to prevent any protein denaturation. Chronoamperometry (CA) data were collected at a bias of +0 V vs. reference and idled for 15 min before exposing the PSI-SLB/SAM/Au electrodes to light on/off conditions with 2–5 minutes pulses. This potential was chosen to facilitate the photoresponse solely from PSI. This bias is close to the open circuit voltage (OCV) for all tested PSI-SLB/SAM/Au electrodes, with minor background current shifts. We note here that the OCV shifts at varying solution content and concentrations, as well as upon surface modifications. A constant bias voltage was chosen over OCV to control the energy gap at the electrode surface, which greatly affects the electron transfer kinetics to and from PSI or methyl viologen (MV). 1 mM of methyl violgen (MV) was added as the electron scavenger. All data were measured under dark, room temperature conditions except for the light experiments where the measurements were

taken while the working electrodes was under illumination from an LED source (ThorLabs; model: M660L4) with a nominal intensity of 1000 W m^{-2} (λ = 660 nm).

4.3 RESULTS AND DISCUSSION

In order to illustrate the arrangements of the immobilized PSI-proteoliposome systems, Figure 4.1 depicts the typical hierarchical assembly of PSI complexes in synthetic membrane-bound PSI structures on SAM-mediated electrode substrates. The figure also displays the anticipated electron transfer pathways for the oriented PSI systems.
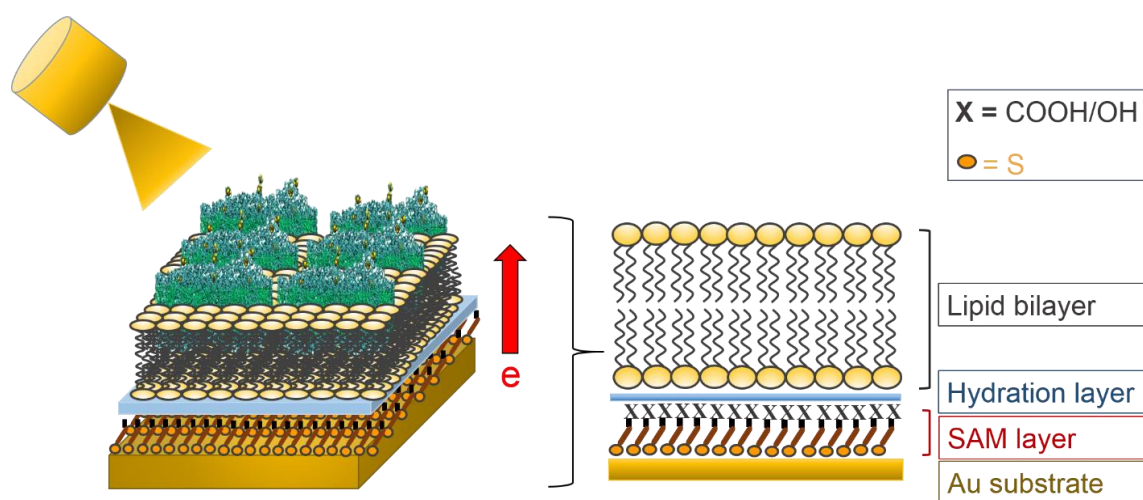
Figure 4.1 Schematic representation of a typical PSI-SLB/SAM/Au electrode assembly along with the anticipated electron transfer pathway.

The presence of trimeric PSI complexes, as extracted from cyanobacterial cultures and described in the Experimental Section, was first confirmed using negative-staining electron microscopy (NS-EM) as shown in Figure 4.2. Figure 4.2 also show the typical structure and dimensions of a PSI trimer as revealed by previous crystallographic studies. Subsequently, PSI-proteoliposme reconstitution was carried out by incorporating PSI solubilized with a prototypical non-ionic detergent namely, Triton X-100 (TX-100) into liposomes destabilized with TX-100 at detergent concentrations of C_{Trit} = 4.0, 8.0 and 12.0 mM. Lipid, detergent and protein concentrations for the successful reconstitution process have been described in details in our recent work on surfactant induced DPhPG solubilization (see chapter.3).[67] Following the PSI insertion,

the excess detergent was adsorbed by using polystyrene beads. All protein reconstitutions were performed at protein-to-lipid weight ratios of 1.2. In turn, size-exclusion chromatography (SEC) fractions were collected prior to any PSI-proteoliposome analyses. Specifically, PSI-proteoliposmes were separated from individual PSIs, small aggregates or excess detergents based on their physical size differences (data shown in chapter.3).[67] To assemble the PSI-SLB (i.e., PSI incorporated within supported lipid bilayers) electrode, PSI-proteoliposome suspensions collected from SEC fractions were drop casted onto OH- and COOH-terminated thiol SAM/Au substrates (see the Experimental Section). Detailed technical specifications regarding the physical properties of 4-mercaptobutyric acid (C_4-COOH), 4-Mercapto-1-butanol (C_4-OH) and 6-Mercapto-1-hexanol (C_6-OH) are provided in Table 4.1.

Table 4.1 Physical properties of SAMs, C4-COOH, C4-OH and C6-OH

Chemical Name	Linear Formula	Molecular Weight
4-Mercaptobutyric acid	HS(CH2)3COOH	120.17
4-Mercapto-1-butanol	HS(CH2)4OH	106.19
6-Mercapto-1-hexanol	HS(CH2)6OH	134.24

4.3.1 Photoelectrochemical Properties of PSI-SLB Electrodes

Chronoamperometry (CA) measurements were carried out on PSI-SLB/C_4COOH SAM/Au, PSI-SLB/C_4OH SAM/Au and PSI-SLB/C_6OH SAM/Au electrodes in light and dark conditions with the addition of methyl viologen (MV) as the electron scavenger under aerobic conditions. MV acts as an electron acceptor from the reducing (stromal) side of PSI.[54] Here, the aerobic conditions refer to the ambient equivalent levels of dissolved oxygen (O_2) in the buffer electrolyte solution.

Figure 4.3 shows that in the presence of MV and dissolved O_2, a stable net photocurrent of ~ 14.5 nA/cm^2 (negative directions as compared to baseline current suggesting the upward oriented incorporation) is achieved in the case of PSI-SLB/C_4COOH SAM/Au electrode, while a stable net photocurrent of ~18 nA/cm^2 and ~20 nA/cm^2 is obtained in the case of PSI-SLB/C_4OH SAM/Au and PSI-SLB/C_6OH SAM/Au electrodes, respectively.
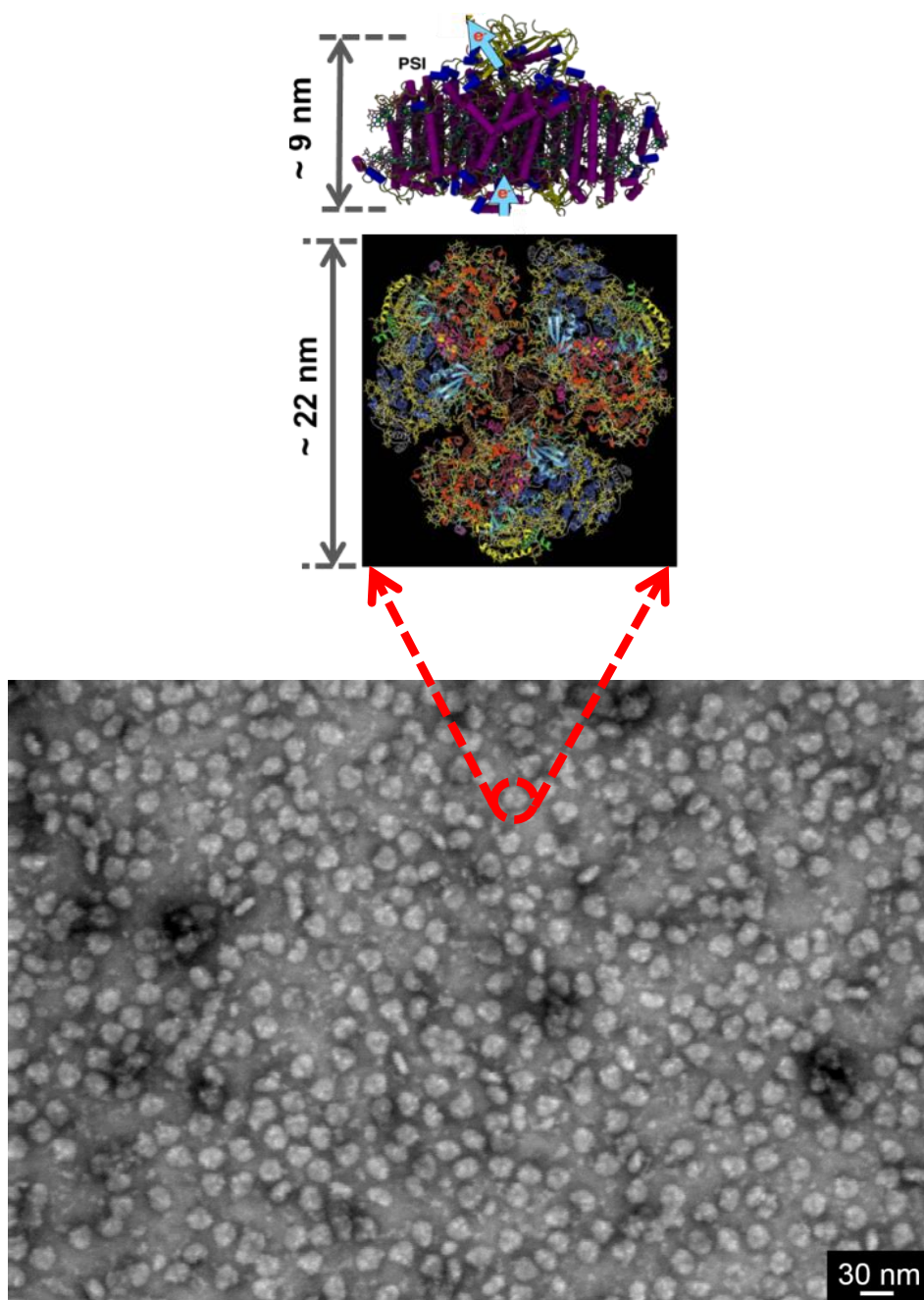
Figure 4.2 Stained-TEM micrograph representing individual PSI trimeric complexes from cyanobacterial strains. (Top) Typical structure and dimensions of PSI trimer from crystallographic studies.

All photocurrents are reported for the third equilibrated light on/off pulse in Figure 4.3. The aforementioned data are obtained for PSI-proteoliposome reconstituted with $C_{Trit} = 12.0$ mM. The SAM treated Au substrate without the addition of PSI generated a photocurrent of ~ 1 nA/cm^2 (Figure 4.3). The comparisons of the maximum photocurrent density obtained from the electrochemical CA measurements on various SAM substrates with different terminal chemistries and PSI-proteoliposmes reconstituted with different detergent concentrations ($C_{Trit} = 4.0$, 8.0 and 12.0 mM), reveal almost similar photocurrents to the one obtained from PSI/C$_4$COOH SAM/Au substrate with a minor increase observed in the case of PSI-SLB/SAM/Au samples for PSI-proteoliposomes reconstituted with $C_{Trit} = 12$mM (Figure 4.4). This observation contradicts our initial hypothesis that PSI confinements in a biomimetic membrane framework will promote photocurrent enhancements.

In an effort to explain these observations, surface topography images for of PSI-SLB treated C$_4$-COOH SAM/Au, C$_4$-OH SAM/Au and C$_6$-OH SAM/Au substrates acquired from AFM measurements are presented in Figure 4.5a-d. These images reveal a semi-sparse monolayer of PSIs within the SLB, as well the presence of some intact liposomes which have not fully collapsed on the SAM layers (arrow indicators in Figures 4.5b-d). However in the case of the deposition of individual PSI trimers onto the alkanethiolate SAM/Au substrates, as shown in Figure 4.5a, a relatively uniform PSI monolayer formation with high surface coverage, as reported in our earlier studies, is observed.[51,53] It should be noted that although only PSI deposition on the C$_4$COOH SAM/Au substrate is shown in Figure 4.5a, PSI depositions on C$_4$OH SAM/Au and C$_6$OH SAM/Au substrates also indicated similar dense monolayer coverage.

The aforementioned differences in the surface coverage (number of immobilized PSI per unit area of the electrode) can provide a plausible explanation for the relatively low photocurrent enhancement achieved in the case of membrane-bound PSI/SAM/Au electrode cases. In order to further investigate our rationale, the number of PSI complexes assembled per unit surface area was subsequently counted from the respective AFM images. Specifically, the PSI complexes were identified based on the typical average protein diameters of ~22 nm as well as average heights of ~9 nm which are commensurate with the expected dimensions of the cyanobacterial PSI trimeric complexes (see Figure 4.2).[51,53]
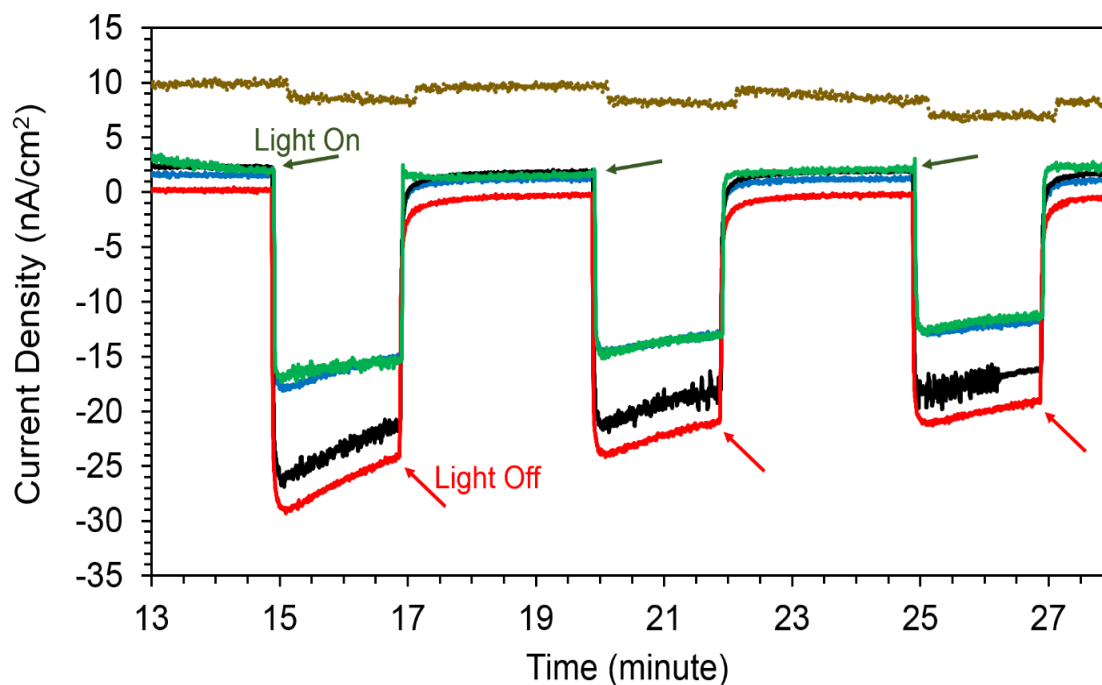
Figure 4.3 Results showing a maximum 14.5 ± 0.9 nA/cm^2 cathodic photocurrent from PSI/C$_4$COOH SAM/Au substrate at OCV vs. Ag/AgCl under illumination ($\lambda = 660$ nm) under aerobic conditions (green line). Subsequent photocurrent enhancements for PSI-SLB assembled onto C$_4$COOH-thiol/Au (blue line), C$_4$OH-thiol/Au (black line) and C$_6$OH-thiol/Au (red line) are also indicated. The Photocurrent of SAM treated Au substrate without the addition of PSI (ochre line) is moved up for ease of visualization.
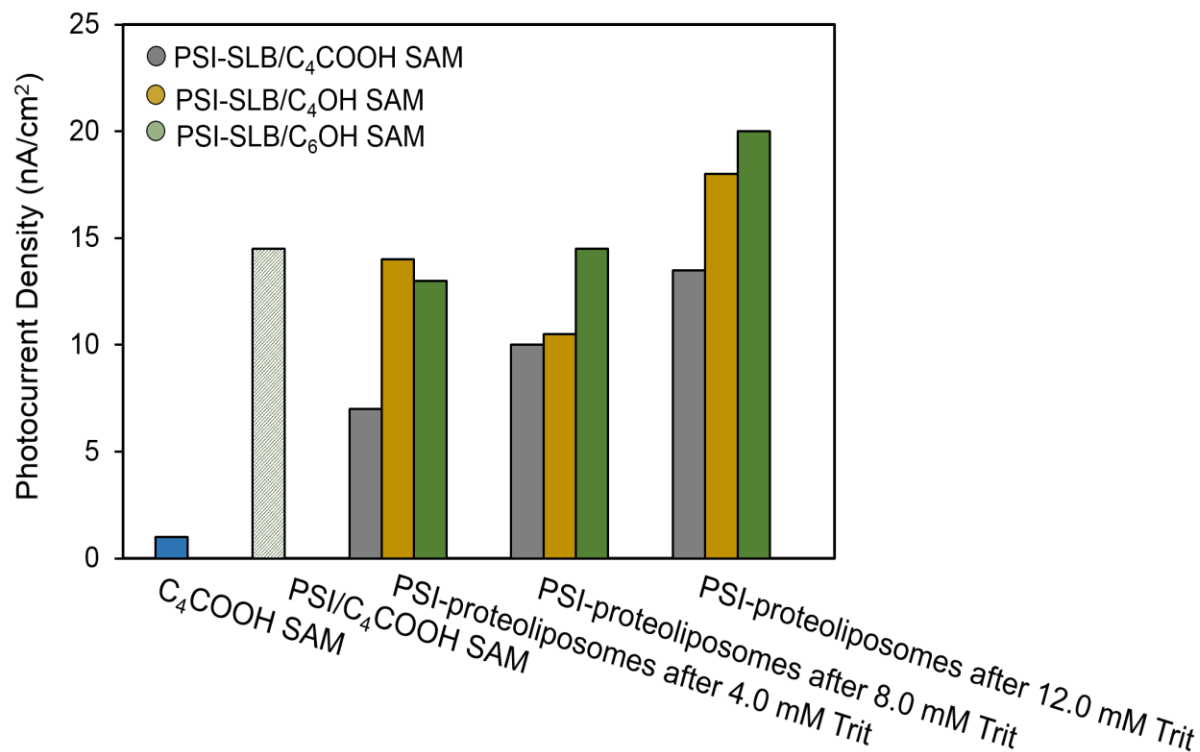
Figure 4.4 Comparisons for maximum photocurrent densities (nA/cm^2) as obtained from chronoamperometry measurements on C4COOH/SAM (controls) along with PSI-SLB on different SAM/Au substrates made from PSI-proteoliposomes reconstituted with different TX-100 concentrations (C$_{Trit}$ = 4, 8 and 12 mM).
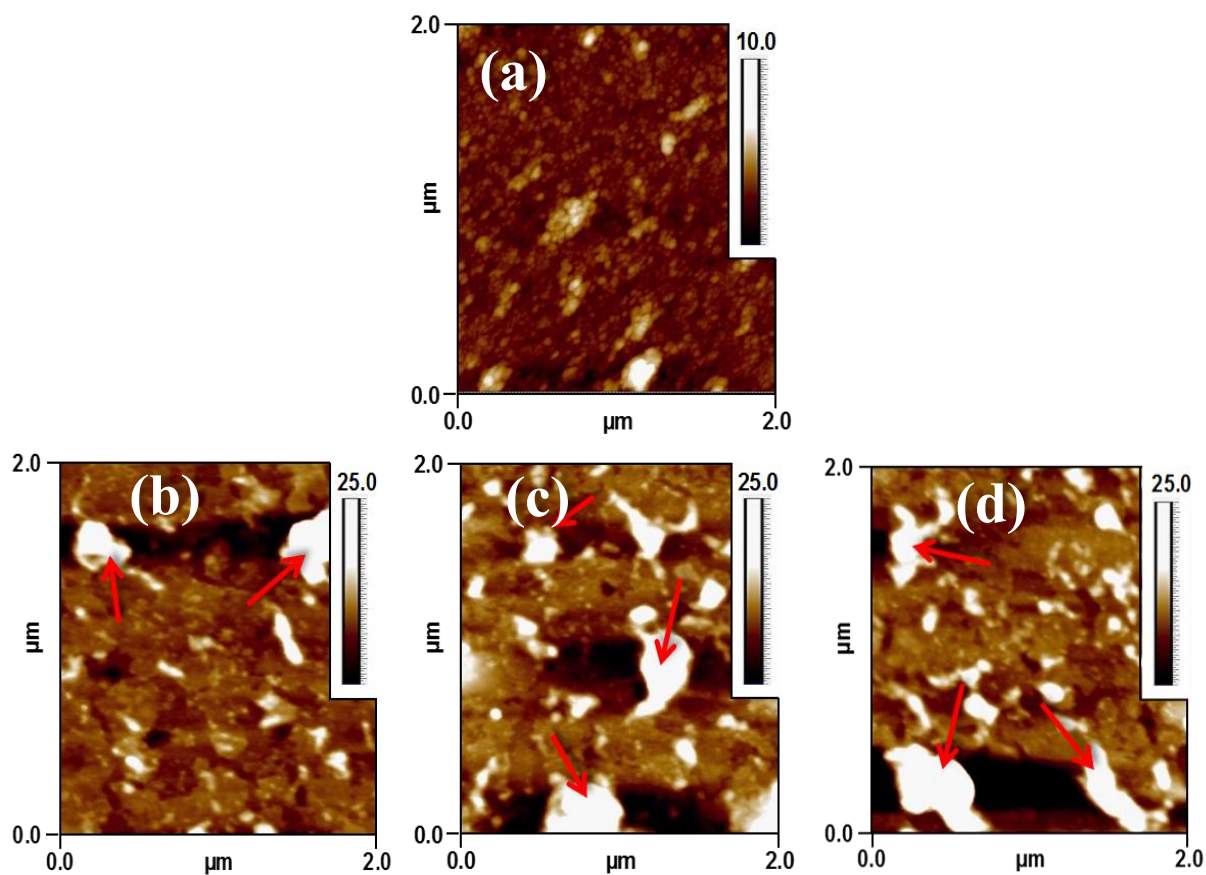
Figure 4.5 AFM images showing the surface topographies of: (a) PSI/C$_4$COOH SAM/Au; (b) PSI-SLB/C4COOH SAM/Au; (c) PSI-SLB/C$_4$OH SAM/Au and (d) PSI-SLB/C$_6$OH SAM/Au. Red arrows indicate the presence of liposomes not fully collapsed onto the SAM substrates.

Upon normalization of the measured photocurrent densities with respect to the number of PSI complexes immobilized on the respective substrates (as calculated from imaging analysis of AFM topographies), the photocurrent enhancements for the reconstituted PSI-proteoliposomes as compared to those from individual PSI trimers immobilized on SAM/Au substrates immediately become evident (see Figure 4.6). Specifically, the representative case of PSI-proteoliposomes reconstituted with $C_{Trit} = 12$ mM (i.e., the optimal reconstitution case based on our earlier studies; see chapter.3),[67] indicate $\sim$ 3-4 times enhancements in the photocurrent obtained from the PSI-SLB/C$_4$OH SAM/Au substrate when compared to that from the PSI/C$_4$COOH SAM/Au substrate. Also, based on the AFM images and photocurrent measurements, our observations indicate the possibility of a better assembly and hence higher performance for PSI-SLBs formed on OH-terminated SAMs.
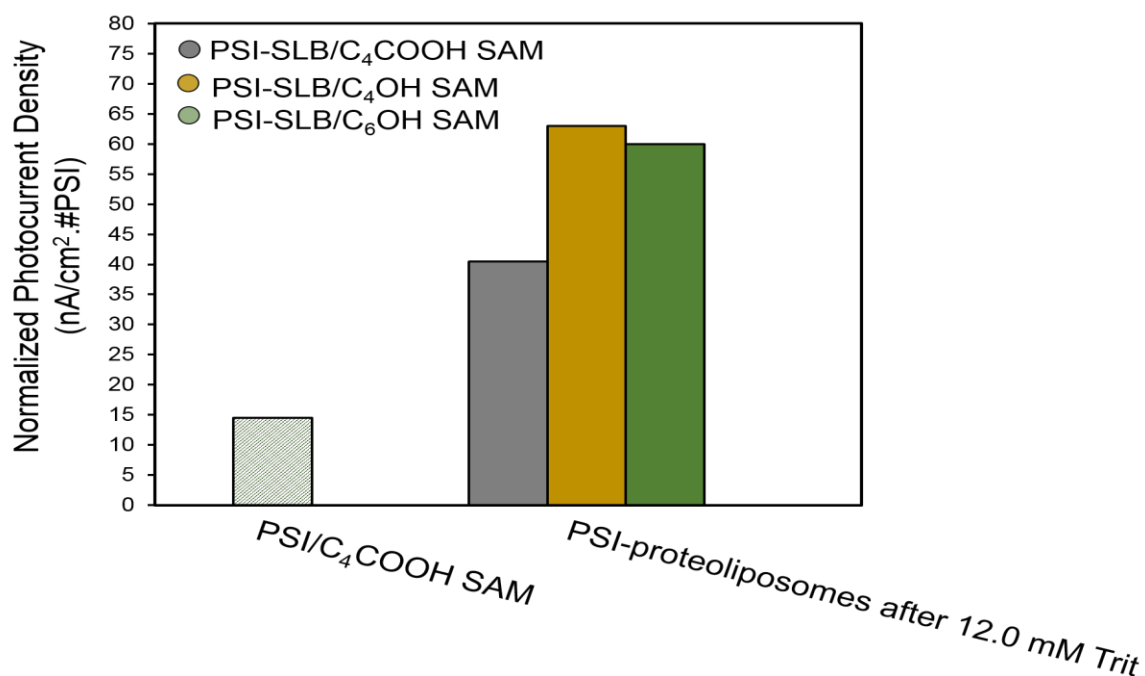
Figure 4.6 Comparisons for the maximum photocurrent densities normalized with respect to number of PSI complexes assembled on the respective substrates. Representative results compared here for PSI-SLB/SAM/Au substrates made from PSI-proteoliposomes reconstituted with 12 mM TX-100.

4.4 CONCLUSIONS

The work presented here demonstrates photocurrent enhancements obtained as a result of systematic assembly of functional PSI, an integral membrane protein complex, onto bio-abio interfaces via protein confinement in suitable membrane scaffoldings namely, PG-based negatively charged liposomes (DPhPG) that mimic the natural thylakoid membrane housing of PSI. Specifically, this study paves the way toward successful fabrication of efficient PSI-based bio-hybrid photoelectrochemical energy conversion devices. Moreover, detailed electrochemical measurements of PSI-proteoliposomes supported on various alkanethiolate SAM/Au surfaces indicate up to four times enhancements in the photocurrent density as compared to the measurements from dense monolayer of individual PSI on SAM/Au substrates. Overall, this study underscores the critical significance of the understanding of the unique optoelectronic properties of PSI under biomimetic confinement that is required for advancement in the design of photochemical energy conversion systems as well as artificial photosynthetic systems.

CHAPTER 5

CONCLUSION AND FUTURE DIRECTION

This dissertation focuses on utilizing the cyanobacterial PSI from *Thermosynechococcus Elongatus* for integration into organic/inorganic interfaces in bio-hybrid devices that mediate photo-electrochemical energy conversions for electricity and/or solar fuel production. In this thesis the effect of systematic incorporation of PSI complexes into synthetic membrane-bound structures that mimic the natural thylakoid membrane housing of PSI in an effort to enhance their performances and photocurrent responses has been demonstrated.

In Chapter 1, the photosynthesis process was introduced from a functional point of view and in particular, the foundation was laid out for a basic understanding of the structures associated with cyanobacterial photosynthetic membrane proteins, the function of thylakoid membrane and photactivated properties of PSI. Furthermore, the background literature review for PSI biohybrid systems/devices along with techniques and methods by which such bio-hybrid systems were experimentally characterized was discussed in details.

In Chapter 2, phase transition stages for detergent-mediated liposome solubilization of bio-mimetic membranes was investigated with the primary motivation of choosing a suitable synthetic lipid bilayer membrane for integrating the transmembrane protein complex, PSI into bio-hybrid opto-electronic devices. To this end, the interaction of two nonionic detergents *n-dodecyl*-β-D-maltoside (DDM) and Triton X-100 (TX-100) with two types of phospholipids, namely DPhPC (1,2-diphytanoyl-*sn*-glycero-3-phosphocholine) and DPPG (1,2-dipalmitoyl-*sn*-glycero-3-phospho-(1'-*rac*-glycerol)) were examined. Specifically, solubilization processes for large unilamellar liposomes were studied with the aid of turbidity measurements, dynamic light scattering and cryo-transmission electron microscopy imaging. Results from this research indicated that the solubilization process is well depicted by a three-stage model, wherein the lamellar-to-micellar transitions for DPhPC liposomes are dictated by the critical detergent/phospholipid ratios. The solubilization of DPhPC by DDM was devoid of a "gel-like" phase unlike that of reported for egg PC treated with DDM.[90,92] Furthermore, DDM is shown to be a stable candidate for DPhPC solubilization and proteoliposome formation. Finally, although the solubilization of DPPG with DDM indicated the familiar three-stage process, the same process with TX-100 indicated structural deformation of vesicles into complex network of kinetically trapped micro and nanostructured arrangements of lipid bilayers.

The role of the natural thylakoid membrane housing of PSI in driving its robust photoactivated charge separation with near unity quantum efficiency is not fundamentally understood. To this

end, rational design of suitable biomimetic protein scaffolds for PSI incorporation is of great scientific interest as it can pave the path for future fabrication of bio-hybrid devices such as solid state bioelectronics, bio-hybrid sensors, and photoelectrochemical devices. In all such devices, optimally designed bio-abio interfaces need to be integrated such that they do not compromise the intrinsic photoactivity of PSI. Therefore, **Chapter 3** is dedicated to the fundamental understanding of surfactant-induced membrane solubilization of a negatively charged phospholipid (DPhPG) with the motivation of PSI reconstitution in DPhPG liposomes as a biomimetic reconstruct of the natural membrane bound protein. Specifically, a simple yet elegant method for incorporation of PSI trimeric complexes into DPhPG bilayer membranes that mimic the natural thylakoid membrane housing of PSI is introduced. The efficacy of this method was demonstrated via absorption and fluorescence spectroscopy measurements as well as direct visualization using atomic force microscopy. This study provided the proof-of-concept evidence for the possibility of tuning the photoexcitation characteristics of PSI confined in synthetic lipid scaffolds.

Inspired by the preliminary results of Chapter 3, **Chapter 4** delves into the detailed photoelectrochemical characterizations of PSI-proteoliposomes made from PSI incorporated within biomimetic membrane scaffolds and supported on suitable SAM substrates with the goal of achieving biomimetic entrapment of PSI on hybrid electrode surfaces. Detailed electrochemical measurements were conducted to investigate the enhancement of photocurrent arising from such confinement. Atomic force microscopy measurements were used as a direct visualization tool to image assembly process. Finally, it was observed that the aforementioned bio hybrid electrodes made from SAM supported PSI-proteoliposome systems indicated a photocurrent generation that was recorded to be four times higher than that generated from a dense monolayer of individual PSI immobilized on SAM substrates using an equivalent amount of PSI.

Perspectives, Future Directions and Recommendations

The research studies presented in the current thesis offered fundamental science advancements to previous studies in the field of bio hybrid devices fabricated using PSI as the photoactive charge separator. The facile and elegant incorporation of PSI trimeric complexes into bilayer membranes that mimic the natural thylakoid membrane housing of PS facilitated the ideal biomimetic reconstructs for highly efficient photoactivated electron transport in bio hybrid systems. While great progress in the design and construction of reconstituted PSI-based systems has been

described in this work, the full potential of achieving the photo excited energy transfer with near unity quantum efficiency for the protein complex encapsulated within synthetic protein scaffolds remains a grand challenge problem. Hence, the development of these bio hybrid technologies should focus on further addressing the obvious question regarding the role of the natural thylakoid membrane housing of PSI trimeric complex in providing the required structural and functional scaffold to the protein. The selection of optimal synthetic scaffolds for the seamless incorporation of PSI into biomimetic systems is required to enhance the performance of PSI-driven optoelectronic devices. Furthermore, special attention should be focused on the development of more effective electrochemical mediators for efficient electron transport pathways, enhancement of the light absorbing capabilities of PSI, and improvement in immobilization techniques for reconstituted PSI on suitable surfaces. Finally, a systematic study of the role of confinement in tuning the inter-chromophore electronic coupling within the protein complex and the possible role of quantum coherent effects in the excitation energy transfer processes is of utmost importance. Specifically, understanding quantum coherent effects as a function of microenvironment alteration in complex photoactive biomaterials will be critical to the basic understanding of the unique optoelectronic properties of PSI under biomimetic confinement, thereby paving the way for advancements in the future design of artificial photosynthetic systems. More broadly, the suggested future studies will enable the development of next generation complex electronic materials across many disciplines such as biology, chemistry, and materials science.

REFERENCES

1   Nelson, N. & Ben-Shem, A. The structure of photosystem I and evolution of photosynthesis. *Bioessays* **27**, 914-922, doi:10.1002/bies.20278 (2005).

2   Orr, L. & Govindjee. Photosynthesis online. *Photosynthesis Research* **105**, 167-200, doi:10.1007/s11120-010-9570-8 (2010).

3   Leadbetter, E. R. & Poindexter, J. S. *Bacteria in Nature*. Vol. 1 (Plenum Press, 1985).

4   Walker, D. *Energy, Plants and Man*. (Oxygraphics, 1992).

5   Liberton, M. *et al.* Organization and Flexibility of Cyanobacterial Thylakoid Membranes Examined by Neutron Scattering. *The Journal of Biological Chemistry* **288**, 3632-3640, doi:10.1074/jbc.M112.416933 (2013).

6   Stingaciu, L.-R. *et al.* Revealing the Dynamics of Thylakoid Membranes in Living Cyanobacterial Cells. *Scientific Reports* **6**, 19627, doi:10.1038/srep19627 (2016).

7   Davis, A. D. *Light-dark FTIR absorbance difference spectroscopy for the study of photosystem I* Bachelor of science thesis, Brock University, (2007).

8   Jordan, P. *et al.* Three-dimensional structure of cyanobacterial photosystem I at 2.5[thinsp][angst] resolution. *Nature* **411**, 909-917, doi:http://www.nature.com/nature/journal/v411/n6840/suppinfo/411909a0_S1.html (2001).

9   Golbeck, J. H. *Photosystem I: The light-driven plastocyanin: ferredoxin oxidoreductase*. Vol. 24 764 (Springer, 2006).

10   Brettel, K. Electron transfer and arrangement of the redox cofactors in photosystem I. *Biochimica et Biophysica Acta (BBA) - Bioenergetics* **1318**, 322-373, doi:http://dx.doi.org/10.1016/S0005-2728(96)00112-0 (1997).

11   Brettel, K. & Leibl, W. Electron transfer in photosystem I. *Biochimica et Biophysica Acta (BBA) - Bioenergetics* **1507**, 100-114, doi:http://dx.doi.org/10.1016/S0005-2728(01)00202-X (2001).

12   Nelson, N. Evolution of photosystem I and the control of global enthalpy in an oxidizing world. *Photosynthesis Research* **116**, 145-151, doi:10.1007/s11120-013-9902-6 (2013).

13   Bennett, T. *et al.* Elucidating the role of methyl viologen as a scavenger of photoactivated electrons from photosystem I under aerobic and anaerobic conditions. *Physical chemistry chemical physics : PCCP* **18**, 8512-8521, doi:10.1039/c6cp00049e (2016).

14   Terasaki, N. *et al.* Fabrication of novel photosystem I-gold nanoparticle hybrids and their photocurrent enhancement. *Thin Solid Films* **499**, 153-156, doi:10.1016/j.tsf.2005.07.050 (2006).

15   Gerster, D. *et al.* Photocurrent of a single photosynthetic protein. *Nat Nano* **7**, 673-676, doi:http://www.nature.com/nnano/journal/v7/n10/abs/nnano.2012.165.html#supplementary-information (2012).

16   Ciesielski, P. N. *et al.* Functionalized Nanoporous Gold Leaf Electrode Films for the Immobilization of Photosystem I. *Acs Nano* **2**, 2465-2472, doi:10.1021/nn800389k (2008).

17   LeBlanc, G., Chen, G., Gizzie, E. A., Jennings, G. K. & Cliffel, D. E. Enhanced Photocurrents of Photosystem I Films on p-Doped Silicon. *Adv Mater* **24**, 5959-5962, doi:10.1002/adma.201202794 (2012).

18   LeBlanc, G., Chen, G., Jennings, G. K. & Cliffel, D. E. Photoreduction of Catalytic Platinum Particles Using Immobilized Multilayers of Photosystem I. *Langmuir* **28**, 7952-7956, doi:10.1021/la301019t (2012).

19   Gunther, D. *et al.* Photosystem I on Graphene as a Highly Transparent, Photoactive Electrode. *Langmuir* **29**, 4177-4180, doi:10.1021/la305020c (2013).

20   LeBlanc, G., Winter, K. M., Crosby, W. B., Jennings, G. K. & Cliffel, D. E. Integration of Photosystem I with Graphene Oxide for Photocurrent Enhancement. *Adv. Energy Mater.* **4**, 5, doi:10.1002/aenm.201301953 (2014).

21   Frolov, L., Rosenwaks, Y., Richter, S., Carmeli, C. & Carmeli, I. Photoelectric Junctions Between GaAs and Photosynthetic Reaction Center Protein. *The Journal of Physical Chemistry C* **112**, 13426-13430, doi:10.1021/jp800586w (2008).

22   Carmeli, I. *et al.* A Photosynthetic Reaction Center Covalently Bound to Carbon Nanotubes. *Adv Mater* **19**, 3901-3905, doi:10.1002/adma.200700536 (2007).

23   Kaniber, S. M., Brandstetter, M., Simmel, F. C., Carmeli, I. & Holleitner, A. W. On-Chip Functionalization of Carbon Nanotubes with Photosystem I. *J Am Chem Soc* **132**, 2872-2873, doi:10.1021/ja910790x (2010).

24   Greenbaum, E. PLATINIZED CHLOROPLASTS - A NOVEL PHOTOCATALYTIC MATERIAL. *Science* **230**, 1373-1375, doi:10.1126/science.230.4732.1373 (1985).

25   Greenbaum, E. PHOTOBIOELECTRONIC STUDIES WITH THYLAKOID MEMBRANES. *Applied Biochemistry and Biotechnology* **20-1**, 813-824, doi:10.1007/bf02936528 (1989).

26   Iwuchukwu, I. J. *et al.* Self-organized photosynthetic nanoparticle for cell-free hydrogen production. *Nat Nano* **5**, 73-79, doi:http://www.nature.com/nnano/journal/v5/n1/suppinfo/nnano.2009.315_S1.html (2010).

27   Evans, B. R., O'Neill, H. M., Hutchens, S. A., Bruce, B. D. & Greenbaum, E. Enhanced Photocatalytic Hydrogen Evolution by Covalent Attachment of Plastocyanin to Photosystem I. *Nano Letters* **4**, 1815-1819, doi:10.1021/nl0493388 (2004).

28   Utschig, L. M. *et al.* Photocatalytic Hydrogen Production from Noncovalent Biohybrid Photosystem I/Pt Nanoparticle Complexes. *The Journal of Physical Chemistry Letters* **2**, 236-241, doi:10.1021/jz101728v (2011).

29   Lee, J. W., Lee, I. & Greenbaum, E. Platinization: A novel technique to anchor photosystem I reaction centres onto a metal surface at biological temperature and pH. *Biosensors & Bioelectronics* **11**, 375-387, doi:10.1016/0956-5663(96)82733-3 (1996).

30   Frolov, L., Wilner, O., Carmeli, C. & Carmeli, I. Fabrication of Oriented Multilayers of Photosystem I Proteins on Solid Surfaces by Auto-Metallization. *Adv Mater* **20**, 263-266, doi:10.1002/adma.200701474 (2008).

31   Lee, I., Lee, J. W. & Greenbaum, E. Biomolecular electronics: Vectorial arrays of photosynthetic reaction centers. *Physical Review Letters* **79**, 3294-3297, doi:10.1103/PhysRevLett.79.3294 (1997).

32   Kievit, O. & Brudvig, G. W. Direct electrochemistry of photosystem I. *J Electroanal Chem* **497**, 139-149, doi:10.1016/s0022-0728(00)00467-8 (2001).

33   Munge, B. *et al.* Electron Transfer Reactions of Redox Cofactors in Spinach Photosystem I Reaction Center Protein in Lipid Films on Electrodes. *J Am Chem Soc* **125**, 12457-12463, doi:10.1021/ja036671p (2003).

34   Proux-Delrouyre, V. *et al.* Electrocatalytic Investigation of Light-Induced Electron Transfer between Cytochrome c6 and Photosystem I. *J Am Chem Soc* **125**, 13686-13692, doi:10.1021/ja0363819 (2003).

35   Das, R. *et al.* Integration of Photosynthetic Protein Molecular Complexes in Solid-State Electronic Devices. *Nano Letters* **4**, 1079-1083, doi:10.1021/nl049579f (2004).

36   Terasaki, N. *et al.* Plugging a Molecular Wire into Photosystem I: Reconstitution of the Photoelectric Conversion System on a Gold Electrode. *Angewandte Chemie International Edition* **48**, 1585-1587, doi:10.1002/anie.200805748 (2009).

37   Terasaki, N. *et al.* Photosensor Based on an FET Utilizing a Biocomponent of Photosystem I for Use in Imaging Devices. *Langmuir* **25**, 11969-11974, doi:10.1021/la901091e (2009).

38   Terasaki, N. *et al.* Bio-photosensor: Cyanobacterial photosystem I coupled with transistor via molecular wire. *Biochimica et Biophysica Acta (BBA) - Bioenergetics* **1767**, 653-659, doi:http://dx.doi.org/10.1016/j.bbabio.2006.11.008 (2007).

39   Frolov, L., Rosenwaks, Y., Carmeli, C. & Carmeli, I. Fabrication of a photoelectronic device by direct chemical binding of the photosynthetic reaction center protein to metal surfaces. *Adv Mater* **17**, 2434-+, doi:10.1002/adma.200500295 (2005).

40   Ko, B. S. *et al.* Effect of surface composition on the adsorption of photosystem I onto alkanethiolate self-assembled monolayers on gold. *Langmuir* **20**, 4033-4038, doi:10.1021/la0356809 (2004).

41   Kincaid, H. A., Niedringhaus, T., Ciobanu, M., Cliffel, D. E. & Jennings, G. K. Entrapment of Photosystem I within Self-Assembled Films. *Langmuir* **22**, 8114-8120, doi:10.1021/la061326+ (2006).

42   Ciobanu, M., Kincaid, H. A., Jennings, G. K. & Cliffel, D. E. Photosystem I Patterning Imaged by Scanning Electrochemical Microscopy. *Langmuir* **21**, 692-698, doi:10.1021/la048075u (2005).

43   Ciobanu, M. *et al.* Electrochemistry and photoelectrochemistry of photosystem I adsorbed on hydroxyl-terminated monolayers. *J. Electroanal. Chem.* **599**, 72-78, doi:10.1016/j.jelechem.2006.09.019 (2007).

44   Faulkner, C. J., Lees, S., Ciesielski, P. N., Cliffel, D. E. & Jennings, G. K. Rapid Assembly of Photosystem I Monolayers on Gold Electrodes. *Langmuir* **24**, 8409-8412, doi:10.1021/la800670b (2008).

45   Ciesielski, P. N. *et al.* Enhanced Photocurrent Production by Photosystem I Multilayer Assemblies. *Adv Funct Mater* **20**, 4048-4054, doi:10.1002/adfm.201001193 (2010).

46   Ciesielski, P. N. *et al.* Photosystem I – Based biohybrid photoelectrochemical cells. *Bioresource Technol* **101**, 3047-3053, doi:http://dx.doi.org/10.1016/j.biortech.2009.12.045 (2010).

47   Yella, A. *et al.* Porphyrin-Sensitized Solar Cells with Cobalt (II/III)–Based Redox Electrolyte Exceed 12 Percent Efficiency. *Science* **334**, 629-634, doi:10.1126/science.1209688 (2011).

48   Chen, G. P., LeBlanc, G., Jennings, G. K. & Cliffel, D. E. Effect of Redox Mediator on the Photo-Induced Current of a Photosystem I Modified Electrode. *Journal of the Electrochemical Society* **160**, H315-H320, doi:10.1149/2.054306jes (2013).

49   Le, R. K., Raeeszadeh-Sarmazdeh, M., Boder, E. T. & Frymier, P. D. Sortase-Mediated Ligation of PsaE-Modified Photosystem I from Synechocystis sp. PCC 6803 to a Conductive Surface for Enhanced Photocurrent Production on a Gold Electrode. *Langmuir* **31**, 1180-1188, doi:10.1021/la5031284 (2015).

50   Manocchi, A. K. *et al.* Photocurrent Generation from Surface Assembled Photosystem I on Alkanethiol Modified Electrodes. *Langmuir* **29**, 2412-2419, doi:10.1021/la304477u (2013).

51	Mukherjee, D., May, M., Vaughn, M., Bruce, B. D. & Khomami, B. Controlling the Morphology of Photosystem I Assembly on Thiol-Activated Au Substrates. *Langmuir* **26**, 16048-16054, doi:10.1021/la102832x (2010).

52	Mukherjee, D., Vaughn, M., Khomami, B. & Bruce, B. D. Modulation of cyanobacterial photosystem I deposition properties on alkanethiolate Au substrate by various experimental conditions. *Colloids and Surfaces B-Biointerfaces* **88**, 181-190, doi:10.1016/j.colsurfb.2011.06.029 (2011).

53	Mukherjee, D., May, M. & Khomami, B. Detergent-protein interactions in aqueous buffer suspensions of Photosystem I (PS I). *J Colloid Interf Sci* **358**, 477-484, doi:10.1016/j.jcis.2011.03.070 (2011).

54	Bennett, T. *et al.* Elucidating the role of methyl viologen as a scavenger of photoactivated electrons from photosystem I under aerobic and anaerobic conditions. *Physical Chemistry Chemical Physics* **18**, 8512-8521, doi:10.1039/C6CP00049E (2016).

55	White, G. F., Racher, K. I., Lipski, A., Hallett, F. R. & Wood, J. M. Physical properties of liposomes and proteoliposomes prepared from Escherichia coli polar lipids. *Biochimica et Biophysica Acta (BBA) - Biomembranes* **1468**, 175-186, doi:http://dx.doi.org/10.1016/S0005-2736(00)00255-8 (2000).

56	Das, N., Murray, D. T. & Cross, T. A. Lipid bilayer preparations of membrane proteins for oriented and magic-angle spinning solid-state NMR samples. *Nature protocols* **8**, 2256-2270, doi:10.1038/nprot.2013.129 (2013).

57	Zhou, H.-X. & Cross, T. A. Influences of membrane mimetic environments on membrane protein structures. *Annu Rev Biophys* **42**, 361-392, doi:10.1146/annurev-biophys-083012-130326 (2013).

58	Saboe, P. O. *et al.* Two-dimensional protein crystals for solar energy conversion. *Advanced Materials* **26**, 7064-+, doi:10.1002/adma.201402375 (2014).

59	Yang, H., Yang, S., Kong, J., Dong, A. & Yu, S. Obtaining information about protein secondary structures in aqueous solution using Fourier transform IR spectroscopy. *Nat. Protocols* **10**, 382-396, doi:10.1038/nprot.2015.024 (2015).

60	Yan, H. *et al.* Influence of molecular structure on the antimicrobial function of phenylenevinylene conjugated oligoelectrolytes. *Chemical Science* **7**, 5714-5722, doi:10.1039/C6SC00630B (2016).

61	Catania, C., Ajo-Franklin, C. & Bazan, G. C. Membrane permeabilization by conjugated oligoelectrolytes accelerates whole-cell catalysis. *RSC Advances* **6**, 100300-100306, doi:10.1039/C6RA23083K (2016).

62	Kirchhofer, N. D., Rasmussen, M. A., Dahlquist, F. W., Minteer, S. D. & Bazan, G. C. The photobioelectrochemical activity of thylakoid bioanodes is increased via photocurrent generation and improved contacts by membrane-intercalating conjugated oligoelectrolytes. *Energy & Environmental Science* **8**, 2698-2706, doi:10.1039/C5EE01707F (2015).

63	Saboe, P. O. *et al.* Biomimetic wiring and stabilization of photosynthetic membrane proteins with block copolymer interfaces. *Journal of Materials Chemistry A* **4**, 15457-15463, doi:10.1039/C6TA07148A (2016).

64	Stieger, K. R. *et al.* Engineering of supramolecular photoactive protein architectures: the defined co-assembly of photosystem I and cytochrome c using a nanoscaled DNA-matrix. *Nanoscale* **8**, 10695-10705, doi:10.1039/C6NR00097E (2016).

65   Stieger, K. R. *et al.* Biohybrid architectures for efficient light-to-current conversion based on photosystem I within scalable 3D mesoporous electrodes. *Journal of Materials Chemistry A* **4**, 17009-17017, doi:10.1039/C6TA07141D (2016).

66   Niroomand, H., Venkatesan, G. A., Sarles, S. A., Mukherjee, D. & Khomami, B. Lipid-detergent phase transitions during detergent-mediated liposome solubilization. *The Journal of Membrane Biology* **249**, 523-538, doi:10.1007/s00232-016-9894-1 (2016).

67   Niroomand, H., Mukherjee, D. & Khomami, B. Tuning the photoexcitation response of cyanobacterial Photosystem I via reconstitution into Proteoliposomes. (2016).

68   Levine, Y. K., Bailey, A. I. & Wilkins, M. H. F. Multilayers of phospholipid biomolecular leaflets. *Nature* **220**, 577-&, doi:10.1038/220577a0 (1968).

69   Gennis, R. B. *Biomembranes: molecular structure and function*. (Springer-Verlag, 1989).

70   Silvius, J. R. Solubilization and functional reconstitution of biomembrane components. *Annual Review of Biophysics and Biomolecular Structure* **21**, 323-348, doi:10.1146/annurev.biophys.21.1.323 (1992).

71   Rigaud, J.-L., Pitard, B. & Levy, D. Reconstitution of membrane proteins into liposomes: application to energy-transducing membrane proteins. *Biochimica et Biophysica Acta (BBA) - Bioenergetics* **1231**, 223-246, doi:http://dx.doi.org/10.1016/0005-2728(95)00091-V (1995).

72   Pata, V., Ahmed, F., Discher, D. E. & Dan, N. Membrane solubilization by detergent: resistance conferred by thickness. *Langmuir* **20**, 3888-3893, doi:10.1021/la035734e (2004).

73   Lichtenberg, D., Robson, R. J. & Dennis, E. A. Solubilization of phospholipids by detergents structural and kinetic aspects. *Biochimica et Biophysica Acta (BBA) - Reviews on Biomembranes* **737**, doi:http://dx.doi.org/10.1016/0304-4157(83)90004-7 (1983).

74   Kragh-Hansen, U., le Maire, M. & Moller, J. V. The mechanism of detergent solubilization of liposomes and protein-containing membranes. *Biophysical Journal* **75**, 2932-2946 (1998).

75   Lopez, O., Cocera, M., Wehrli, E., Parra, J. L. & de la Maza, A. Solubilization of liposomes by sodium dodecyl sulfate: New mechanism based on the direct formation of mixed micelles. *Arch. Biochem. Biophys.* **367**, 153-160, doi:10.1006/abbi.1999.1267 (1999).

76   Lopez, O. *et al.* Octyl glucoside-mediated solubilization and reconstitution of liposomes: Structural and kinetic aspects. *Journal of Physical Chemistry B* **105**, 9879-9886, doi:10.1021/jp010273w (2001).

77   Deamer, D. & Bangham, A. D. Large volume liposome by an ether vaporization method. *Biochimica et Biophysica Acta* **443**, 629-634, doi:10.1016/0005-2736(76)90483-1 (1976).

78   Helenius, A., McCaslin, D. R., Fries, E. & Tanford, C. Properties of detergents. *Methods in enzymology* **56**, 734-749 (1979).

79   Szoka, F. & Papahadjopoulos, D. Comprehensive properties and methods of preparation of lipid vesicles (liposomes). *Annual Review of Biophysics and Bioengineering* **9**, 467-508, doi:doi:10.1146/annurev.bb.09.060180.002343 (1980).

80   Cladera, J., Rigaud, J. L., Villaverde, J. & Dunach, M. Liposome solubilization and membrane protein reconstitution using Chaps and Chapso. *Eur. J. Biochem.* **243**, 798-804, doi:10.1111/j.1432-1033.1997.00798.x (1997).

81   Paternostre, M. T., Roux, M. & Rigaud, J. L. Mechanisms of membrane protein insertion into liposomes during reconstitution procedures involving the use of detergents. 1. Solubilization of large unilamellar liposomes (prepared by reverse-phase evaporation) by

Triton X-100, octyl glucoside, and sodium cholate. *Biochemistry* **27**, 2668-2677, doi:10.1021/bi00408a006 (1988).

82   Sato, N. Roles of the acidic lipids sulfoquinovosyl diacylglycerol and phosphatidylglycerol in photosynthesis: their specificity and evolution. *J. Plant Res.* **117**, 495-505, doi:10.1007/s10265-004-0183-1 (2004).

83   Douce, R., Holtz, R. B. & Benson, A. A. Isolation and properties of envelope of spinach-chloroplasts. *J. Biol. Chem.* **248**, 7215-7222 (1973).

84   Mendiolamorgenthaler, L., Eichenberger, W. & Boschetti, A. Isolation of chloroplast envelopes from chlamydomonas – lipid and polypeptide composition. *Plant Science* **41**, 97-104, doi:10.1016/0168-9452(85)90109-8 (1985).

85   Gombos, Z., Wada, H., Varkonyi, Z., Los, D. A. & Murata, N. Characterization of the Fad12 mutant of Synechocystis that is defective in Delta 12 acyl-lipid desaturase activity. *Biochimica et Biophysica Acta-Lipids and Lipid Metabolism* **1299**, 117-123, doi:10.1016/0005-2760(95)00204-9 (1996).

86   Rigaud, J. L. & Levy, D. Reconstitution of membrane proteins into liposomes. *Liposomes, Pt B* **372**, 65-86 (2003).

87   Lichtenberg, D., Opatowski, E. & Kozlov, M. M. Phase boundaries in mixtures of membrane-forming amphiphiles and micelle-forming amphiphiles. *Biochimica et Biophysica Acta (BBA) - Biomembranes* **1508**, 1-19, doi:http://dx.doi.org/10.1016/S0304-4157(00)00004-6 (2000).

88   Geertsma, E. R., Mahmood, N., Schuurman-Wolters, G. K. & Poolman, B. Membrane reconstitution of ABC transporters and assays of translocator function. *Nature Protocols* **3**, 256-266, doi:10.1038/nprot.2007.519 (2008).

89   Lichtenberg, D., Ahyayauch, H. & Goni, F. M. The mechanism of detergent solubilization of lipid bilayers. *Biophysical Journal* **105**, 1090-1090, doi:10.1016/j.bpj.2013.07.045 (2013).

90   Lambert, O., Levy, D., Ranck, J.-L., Leblanc, G. & Rigaud, J.-L. A new "gel-like" phase in dodecyl maltoside–lipid mixtures: implications in solubilization and reconstitution studies. *Biophysical Journal* **74**, 918-930, doi:http://dx.doi.org/10.1016/S0006-3495(98)74015-9 (1998).

91   Lichtenberg, D., Ahyayauch, H., Alonso, A. & Goñi, F. M. Detergent solubilization of lipid bilayers: a balance of driving forces. *Trends in Biochemical Sciences* **38**, 85-93, doi:http://dx.doi.org/10.1016/j.tibs.2012.11.005 (2013).

92   Knol, J., Sjollema, K. & Poolman, B. Detergent-mediated reconstitution of membrane proteins. *Biochemistry* **37**, 16410-16415, doi:10.1021/bi981596u (1998).

93   Arnulphi, C. *et al.* Triton X-100 partitioning into sphingomyelin bilayers at subsolubilizing detergent concentrations: effect of lipid phase and a comparison with dipalmitoylphosphatidylcholine. *Biophysical Journal* **93**, 3504-3514, doi:10.1529/biophysj.107.104463 (2007).

94   Stuart, M. C. A. & Boekema, E. J. Two distinct mechanisms of vesicle-to-micelle and micelle-to-vesicle transition are mediated by the packing parameter of phospholipid–detergent systems. *Biochimica et Biophysica Acta (BBA) - Biomembranes* **1768**, 2681-2689, doi:http://dx.doi.org/10.1016/j.bbamem.2007.06.024 (2007).

95   Sudbrack, T. P., Archilha, N. L., Itri, R. & Riske, K. A. Observing the solubilization of lipid bilayers by detergents with optical microscopy of GUVs. *The Journal of Physical Chemistry B* **115**, 269-277, doi:10.1021/jp108653e (2011).

96   Nazari, M., Kurdi, M. & Heerklotz, H. Classifying surfactants with respect to their effect on lipid membrane order. *Biophysical Journal* **102**, 498-506, doi:http://dx.doi.org/10.1016/j.bpj.2011.12.029 (2012).

97   Heerklotz, H. & Seelig, J. Correlation of membrane/water partition coefficients of detergents with the critical micelle concentration. *Biophysical Journal* **78**, 2435-2440, doi:http://dx.doi.org/10.1016/S0006-3495(00)76787-7 (2000).

98   Rigaud, J. L., Paternostre, M. T. & Bluzat, A. Mechanism of membrane-protein insertion into liposomes during reconstitution procedures involving the use of detergents .2. Incorporation of the light-driven proton pump bacteriorhodopsin. *Biochemistry* **27**, 2677-2688, doi:10.1021/bi00408a007 (1988).

99   Gaillard, I., Slotboom, D. J., Knol, J., Lolkema, J. S. & Konings, W. N. Purification and reconstitution of the glutamate carrier GltT of the thermophilic bacterium Bacillus stearothermophilus. *Biochemistry* **35**, 6150-6156, doi:10.1021/bi953005v (1996).

100   Lévy, D., Gulik, A., Bluzat, A. & Rigaud, J.-L. Reconstitution of the sarcoplasmic reticulum Ca2+-ATPase: mechanisms of membrane protein insertion into liposomes during reconstitution procedures involving the use of detergents. *Biochimica et Biophysica Acta (BBA) - Biomembranes* **1107**, 283-298, doi:http://dx.doi.org/10.1016/0005-2736(92)90415-I (1992).

101   Coelfen, H., Harding, S. E., Boulter, J. M. & Watts, A. Hydrodynamic examination of the dimeric cytoplasmic domain of the human erythrocyte anion transporter, band 3. *Biophysical Journal* **71**, 1611-1615 (1996).

102   Hagting, A., Velde, J. V. D., Poolman, B. & Konings, W. N. Membrane topology of the di- and tripeptide transport protein of Lactococcus lactis. *Biochemistry* **36**, 6777-6785, doi:10.1021/bi963068t (1997).

103   Parmar, M. M., Edwards, K. & Madden, T. D. Incorporation of bacterial membrane proteins into liposomes: factors influencing protein reconstitution. *Biochimica et Biophysica Acta (BBA) - Biomembranes* **1421**, 77-90, doi:10.1016/s0005-2736(99)00118-2 (1999).

104   Cladera, J., Rigaud, J. L., Bottin, H. & Dunach, M. Functional reconstitution of photosystem I reaction center from cyanobacterium Synechocystis sp PCC6803 into liposomes using a new reconstitution procedure. *Journal of Bioenergetics and Biomembranes* **28**, 503-515, doi:10.1007/bf02110440 (1996).

105   Yang, Z. L., Su, X. H., Wu, F., Gong, Y. D. & Kuang, T. Y. Photochemical activities of plant photosystem I particles reconstituted into phosphatidylglycerol liposomes. *Journal of Photochemistry and Photobiology B-Biology* **78**, 125-134, doi:10.1016/j.jphotobiol.2004.10.003 (2005).

106   Milhiet, P.-E. *et al.* High-resolution AFM of membrane proteins directly incorporated at high density in planar lipid bilayer. *Biophysical Journal* **91**, 3268-3275, doi:10.1529/biophysj.106.087791 (2006).

107   Baba, T. *et al.* Formation and characterization of planar lipid bilayer membranes from synthetic phytanyl-chained glycolipids. *Biochimica et Biophysica Acta (BBA) - Biomembranes* **1421**, 91-102, doi:http://dx.doi.org/10.1016/S0005-2736(99)00114-5 (1999).

108   Koeppe, R. E. & Andersen, O. S. Engineering the gramicidin channel. *Annual Review of Biophysics and Biomolecular Structure* **25**, 231-258 (1996).

109 Spassova, M. *et al.* Pores formed in lipid bilayers and in native membranes by Nodularin, a cyanobacterial toxin. *European Biophysics Journal* **24**, 69-76 (1995).

110 Lovejoy, B., Akerfeldt, K. S., Degrado, W. F. & Eisenberg, D. Crystallization of proton channel peptides. *Protein Science* **1**, 1073-1077 (1992).

111 Hsieh, C. H., Sue, S. C., Lyu, P. C. & Wu, W. G. Membrane packing geometry of diphytanoylphosphatidylcholine is highly sensitive to hydration: phospholipid polymorphism induced by molecular rearrangement in the headgroup region. *Biophysical Journal* **73**, 870-877, doi:http://dx.doi.org/10.1016/S0006-3495(97)78120-7 (1997).

112 Sokolov, V. S. *et al.* Interaction of pyridinium bis-retinoid (A2E) with bilayer lipid membranes. *Journal of Photochemistry and Photobiology B: Biology* **86**, 177-185, doi:http://dx.doi.org/10.1016/j.jphotobiol.2006.09.006 (2007).

113 Andersson, M. *et al.* Vesicle and bilayer formation of diphytanoylphosphatidylcholine (DPhPC) and diphytanoylphosphatidylethanolamine (DPhPE) mixtures and their bilayers' electrical stability. *Colloids and Surfaces B: Biointerfaces* **82**, 550-561, doi:http://dx.doi.org/10.1016/j.colsurfb.2010.10.017 (2011).

114 Bayley, H. *et al.* Droplet interface bilayers. *Molecular BioSystems* **4**, 1191-1208, doi:10.1039/B808893D (2008).

115 Lindsey, H., Petersen, N. O. & Chan, S. I. Physicochemical characterization of 1,2-diphytanoyl-sn-glycero-3-phosphocholine in model membrane systems. *Biochimica et Biophysica Acta (BBA) - Biomembranes* **555**, 147-167, doi:http://dx.doi.org/10.1016/0005-2736(79)90079-8 (1979).

116 Morrow, M. R., Temple, S., Stewart, J. & Keough, K. M. W. Comparison of DPPC and DPPG environments in pulmonary surfactant models. *Biophysical Journal* **93**, 164-175, doi:http://dx.doi.org/10.1529/biophysj.106.102681 (2007).

117 Konovalov, O., Myagkov, I., Struth, B. & Lohner, K. Lipid discrimination in phospholipid monolayers by the antimicrobial frog skin peptide PGLa. A synchrotron X-ray grazing incidence and reflectivity study. *European Biophysics Journal* **31**, 428-437, doi:10.1007/s00249-002-0233-3 (2002).

118 Lohner, K., Latal, A., Degovics, G. & Garidel, P. Packing characteristics of a model system mimicking cytoplasmic bacterial membranes. *Chemistry and Physics of Lipids* **111**, 177-192, doi:http://dx.doi.org/10.1016/S0009-3084(01)00157-8 (2001).

119 Lichtenberg, D. & Barenholz, Y. in *methods of biochemical analysis* (John Wiley & Sons, Inc., 2006).

120 Helenius, A. & Simons, K. Solubilization of membranes by detergents. *Biochimica et Biophysica Acta* **415**, 29-79, doi:10.1016/0304-4157(75)90016-7 (1975).

121 De Carlo, S. & Harris, J. R. Negative staining and cryo-negative staining of macromolecules and viruses for TEM. *Micron* **42**, 117-131, doi:10.1016/j.micron.2010.06.003 (2011).

122 Hayat, M. A. & Miller, S. E. *Negative staining*. (McGraw-Hill, 1990).

123 Kuntsche, J., Horst, J. C. & Bunjes, H. Cryogenic transmission electron microscopy (cryo-TEM) for studying the morphology of colloidal drug delivery systems. *International Journal of Pharmaceutics* **417**, 120-137, doi:10.1016/j.ijpharm.2011.02.001 (2011).

124 Ribeiro, A. A. & Dennis, E. A. Effect of thermotropic phase transitions of dipalmitoylphosphatidylcholine on the formation of mixed micelles with Triton X-100. *Biochimica et Biophysica Acta (BBA) - Biomembranes* **332**, 26-35, doi:http://dx.doi.org/10.1016/0005-2736(74)90118-7 (1974).

125   Patra, S. K., Alonso, A. & Goñi, F. M. Detergent solubilisation of phospholipid bilayers in the gel state: the role of polar and hydrophobic forces. *Biochimica et Biophysica Acta (BBA) - Biomembranes* **1373**, 112-118, doi:http://dx.doi.org/10.1016/S0005-2736(98)00095-9 (1998).

126   Alonso, A., Villena, A. & Goñi, F. M. Lysis and reassembly of sonicated lecithin vesicles in the presence of triton X-100. *FEBS Letters* **123**, 200-204, doi:http://dx.doi.org/10.1016/0014-5793(81)80287-6 (1981).

127   London, E. & Brown, D. A. Insolubility of lipids in Triton X-100: physical origin and relationship to sphingolipid/cholesterol membrane domains (rafts). *Biochimica et Biophysica Acta (BBA) - Biomembranes* **1508**, 182-195, doi:http://dx.doi.org/10.1016/S0304-4157(00)00007-1 (2000).

128   Levitan, I., Christian, A. E., Tulenko, T. N. & Rothblat, G. H. Membrane Cholesterol Content Modulates Activation of Volume-Regulated Anion Current in Bovine Endothelial Cells. *The Journal of General Physiology* **115**, 405-416 (2000).

129   Sanat, K., Raghunathan, V. A. & Satyajit, M. Phase behaviour of dipalmitoyl phosphatidylcholine (DPPC)-cholesterol membranes. *Journal of Physics: Condensed Matter* **17**, S1177 (2005).

130   Babnik, B. *et al.* Shape transformation and burst of giant POPC unilamellar liposomes modulated by non-ionic detergent C12E8. *Chemistry and Physics of Lipids* **125**, 123-138, doi:http://dx.doi.org/10.1016/S0009-3084(03)00084-7 (2003).

131   Yasmann, A. & Sukharev, S. Properties of diphytanoyl phospholipids at the air–water interface. *Langmuir* **31**, 350-357, doi:10.1021/la503800g (2015).

132   Pabst, G., Danner, S., Karmakar, S., Deutsch, G. & Raghunathan, V. A. On the propensity of phosphatidylglycerols to form interdigitated phases. *Biophysical Journal* **93**, 513-525, doi:http://dx.doi.org/10.1529/biophysj.106.101592 (2007).

133   Ege, C. & Lee, K. Y. C. Insertion of azlzheimer's Aβ40 peptide into lipid monolayers. *Biophysical Journal* **87**, 1732-1740, doi:10.1529/biophysj.104.043265 (2004).

134   Ahyayauch, H., Collado, M I., Alonso, A. & Goñi, Felix M. Lipid bilayers in the gel phase become saturated by Triton X-100 at lower surfactant concentrations than those in the fluid phase. *Biophysical Journal* **102**, 2510-2516, doi:10.1016/j.bpj.2012.04.041 (2012).

135   Seddon, A. M., Curnow, P. & Booth, P. J. Membrane proteins, lipids and detergents: not just a soap opera. *Biochimica et Biophysica Acta (BBA) - Biomembranes* **1666**, 105-117, doi:http://dx.doi.org/10.1016/j.bbamem.2004.04.011 (2004).

136   Sorrenti, A., Illa, O. & Ortuno, R. M. Amphiphiles in aqueous solution: well beyond a soap bubble. *Chemical Society Reviews* **42**, 8200-8219, doi:10.1039/c3cs60151j (2013).

137   Lanyi, J. K. & Schobert, B. Structural changes in the L photointermediate of bacteriorhodopsin. *J Mol Biol* **365**, 1379-1392, doi:10.1016/j.jmb.2006.11.016 (2007).

138   Murata, K. *et al.* Structural determinants of water permeation through aquaporin-1. *Nature* **407**, 599-605, doi:10.1038/35036519 (2000).

139   Fleishman, S. J. *et al.* Quasi-symmetry in the cryo-EM structure of EmrE provides the key to modeling its transmembrane domain. *J Mol Biol* **364**, 54-67, doi:10.1016/j.jmb.2006.08.072 (2006).

140   Anfinsen, C. B. Principles that govern the folding of protein chains. *Science* **181**, 223-230, doi:10.1126/science.181.4096.223 (1973).

141   Ketchem, R. R., Lee, K. C., Huo, S. & Cross, T. A. Macromolecular structural elucidation with solid-state NMR-derived orientational constraints. *J Biomol NMR* **8**, 1-14, doi:10.1007/bf00198135 (1996).

142   Cross, T. A., Sharma, M., Yi, M. & Zhou, H.-X. Influence of solubilizing environments on membrane protein structures. *Trends Biochem Sci* **36**, 117-125, doi:10.1016/j.tibs.2010.07.005 (2011).

143   Sharma, M. *et al.* Insight into the mechanism of the influenza A proton channel from a structure in a lipid bilayer. *Science (New York, N.Y.)* **330**, 509-512, doi:10.1126/science.1191750 (2010).

144   Holm, P. J. *et al.* Structural basis for detoxification and oxidative stress protection in membranes. *J Mol Biol* **360**, 934-945, doi:10.1016/j.jmb.2006.05.056 (2006).

145   Jegerschöld, C. *et al.* Structural basis for induced formation of the inflammatory mediator prostaglandin E2. *Proc Natl Acad Sci U S A* **105**, 11110-11115, doi:10.1073/pnas.0802894105 (2008).

146   Das, B. B. *et al.* Structure determination of a membrane protein in proteoliposomes. *J Am Chem Soc* **134**, 2047-2056, doi:10.1021/ja209464f (2012).

147   Grotjohann, I. & Fromme, P. Structure of cyanobacterial photosystem I. *Photosynth Res* **85**, 51-72, doi:10.1007/s11120-005-1440-4 (2005).

148   Mukherjee, D., Vaughn, M., Khomami, B. & Bruce, B. D. Modulation of cyanobacterial Photosystem I deposition properties on alkanethiolate Au substrate by various experimental conditions. *Colloids and Surfaces B: Biointerfaces* **88**, 181 - 190 (2011).

149   Mattei, B., França, A. D. C. & Riske, K. A. Solubilization of binary lipid mixtures by the detergent Triton X-100: the role of cholesterol. *Langmuir* **31**, 378-386, doi:10.1021/la504004r (2015).

150   Marsh, D. *Handbook of Lipid Bilayers, Second Edition*. (CRC Press, 2013).

151   Marsh, D. Cholesterol-induced fluid membrane domains: a compendium of lipid-raft ternary phase diagrams. *Biochimica et Biophysica Acta (BBA) - Biomembranes* **1788**, 2114-2123, doi:http://dx.doi.org/10.1016/j.bbamem.2009.08.004 (2009).

152   Findlay, E. J. & Barton, P. G. Phase behavior of synthetic phosphatidylglycerols and binary-mixtures with phosphatidylcholines in presence and absence of calcium-ions. *Biochemistry* **17**, 2400-2405, doi:10.1021/bi00605a023 (1978).

153   Garidel, P., Johann, C., Mennicke, L. & Blume, A. The mixing behavior of pseudobinary phosphatidylcholine phosphatidylglycerol mixtures as a function of pH and chain length. *European Biophysics Journal with Biophysics Letters* **26**, 447-459, doi:10.1007/s002490050099 (1997).

154   Blosser, Matthew C., Starr, Jordan B., Turtle, Cameron W., Ashcraft, J. & Keller, Sarah L. Minimal effect of lipid charge on membrane miscibility phase behavior in three ternary systems. *Biophysical Journal* **104**, 2629-2638, doi:10.1016/j.bpj.2013.04.055 (2013).

155   Rajarathnam, K. & Rösgen, J. Isothermal titration calorimetry of membrane proteins — progress and challenges. *Biochimica et Biophysica Acta (BBA) - Biomembranes* **1838**, 69-77, doi:http://dx.doi.org/10.1016/j.bbamem.2013.05.023 (2014).

156   Perspicace, S. *et al.* Isothermal titration calorimetry with micelles: thermodynamics of inhibitor binding to carnitine palmitoyltransferase 2 membrane protein. *FEBS Open Bio* **3**, 204-211, doi:http://dx.doi.org/10.1016/j.fob.2013.04.003 (2013).

157   Heerklotz, H. & Seelig, J. Titration calorimetry of surfactant–membrane partitioning and membrane solubilization. *Biochimica et Biophysica Acta (BBA) - Biomembranes* **1508**, 69-85, doi:http://dx.doi.org/10.1016/S0304-4157(00)00009-5 (2000).

158   Heerklotz, H. The microcalorimetry of lipid membranes. *Journal of Physics: Condensed Matter* **16**, R441 (2004).

159   Ball, V. & Maechling, C. Isothermal microcalorimetry to investigate non specific interactions in biophysical chemistry. *International Journal of Molecular Sciences* **10**, 3283 (2009).

160   Draczkowski, P., Matosiuk, D. & Jozwiak, K. Isothermal titration calorimetry in membrane protein research. *Journal of Pharmaceutical and Biomedical Analysis* **87**, 313-325, doi:http://dx.doi.org/10.1016/j.jpba.2013.09.003 (2014).

161   Ghai, R., Falconer, R. J. & Collins, B. M. Applications of isothermal titration calorimetry in pure and applied research—survey of the literature from 2010. *Journal of Molecular Recognition* **25**, 32-52, doi:10.1002/jmr.1167 (2012).

162   Deleu, M., Crowet, J.-M., Nasir, M. N. & Lins, L. Complementary biophysical tools to investigate lipid specificity in the interaction between bioactive molecules and the plasma membrane: a review. *Biochimica et Biophysica Acta (BBA) - Biomembranes* **1838**, 3171-3190, doi:http://dx.doi.org/10.1016/j.bbamem.2014.08.023 (2014).

163   Talling, J. F. ORIGIN OF STRATIFICATION IN AN AFRICAN RIFT LAKE. *Limnology and Oceanography* **8**, 68-78 (1963).

164   Lichtenberg, D. & Barenholz, Y. in *Methods of Biochemical Analysis*   337-462 (John Wiley & Sons, Inc., 2006).

165   Caffarri, S., Tibiletti, T., Jennings, R. C. & Santabarbara, S. A comparison between plant photosystem I and photosystem II architecture and functioning. *Current Protein & Peptide Science* **15**, 296-331 (2014).

166   Yang, Z. L., Su, X. H., Wu, F., Gong, Y. D. & Kuang, T. Y. Effect of phosphatidylglycerol on molecular organization of photosystem I. *Biophysical Chemistry* **115**, 19-27, doi:10.1016/j.bpc.2005.01.004 (2005).

167   Gobets, B., van Stokkum, I. H. M., van Mourik, F., Dekker, J. P. & van Grondelle, R. Excitation wavelength dependence of the fluorescence kinetics in Photosystem I particles from Synechocystis PCC 6803 and Synechococcus elongatus. *Biophysical Journal* **85**, 3883-3898, doi:10.1016/s0006-3495(03)74803-6 (2003).

168   Palsson, L. O., Dekker, J. P., Schlodder, E., Monshouwer, R. & vanGrondelle, R. Polarized site-selective fluorescence spectroscopy of the long-wavelength emitting chlorophylls in isolated photosystem I particles of Synechococcus elongatus. *Photosynth Res* **48**, 239-246, doi:10.1007/bf00041014 (1996).

169   Karapetyan, N. V., Dorra, D., Schweitzer, G., Bezsmertnaya, I. N. & Holzwarth, A. R. Fluorescence spectroscopy of the longwave chlorophylls in trimeric and monomeric photosystem I core complexes from the cyanobacterium Spirulina platensis. *Biochemistry* **36**, 13830-13837, doi:10.1021/bi970386z (1997).

170   Kruip, J., Karapetyan, N. V., Terekhova, I. V. & Rogner, M. In vitro oligomerization of a membrane protein complex - liposome-based reconstitution of trimeric photosystem I from isolated monomers. *Journal of Biological Chemistry* **274**, 18181-18188, doi:10.1074/jbc.274.26.18181 (1999).

171   Papageorgiou, G. C. & Govindjee. *Chlorophyll a Fluorescence: A Signature of Photosynthesis*. Vol. 19 (Springer, 2004).

172 Franck, F., Juneau, P. & Popovic, R. Resolution of the photosystem I and photosystem II contributions to chlorophyll fluorescence of intact leaves at room temperature. *Biochimica et Biophysica Acta (BBA) - Bioenergetics* **1556**, 239-246, doi:http://dx.doi.org/10.1016/S0005-2728(02)00366-3 (2002).

173 Galka, P. *et al.* Functional analyses of the plant photosystem I–light-harvesting complex II supercomplex reveal that light-harvesting complex II loosely bound to photosystem II Is a very efficient antenna for photosystem I in state II. *The Plant Cell* **24**, 2963-2978, doi:10.1105/tpc.112.100339 (2012).

174 Badura, A., Kothe, T., Schuhmann, W. & Rogner, M. Wiring photosynthetic enzymes to electrodes. *Energy & Environmental Science* **4**, 3263-3274, doi:10.1039/C1EE01285A (2011).

175 LeBlanc, G., Chen, G., Gizzie, E. A., Jennings, G. K. & Cliffel, D. E. Enhanced Photocurrents of Photosystem I Films on p-Doped Silicon. *Adv. Mater.* **24**, 5959-+, doi:10.1002/adma.201202794 (2012).

176 Frolov, L., Rosenwaks, Y., Carmeli, C. & Carmeli, I. Fabrication of a photoelectronic device by direct chemical binding of the photosynthetic reaction center protein to metal surfaces. *Adv. Mater.* **17**, 2434-2437, doi:DOI 10.1002/adma.200500295 (2005).

177 Kern, J. *et al.* Purification, characterisation and crystallisation of photosystem II from Thermosynechococcus elongatus cultivated in a new type of photobioreactor. *Biochimica et Biophysica Acta (BBA) - Bioenergetics* **1706**, 147-157, doi:http://dx.doi.org/10.1016/j.bbabio.2004.10.007 (2005).

178 Heerklotz, H., Tsamaloukas, A. D. & Keller, S. Monitoring detergent-mediated solubilization and reconstitution of lipid membranes by isothermal titration calorimetry. *Nat. Protocols* **4**, 686-697 (2009).

APPENDIX

APPENDIX I

Addition of TX-100 to multilamellar DPhPC vesicles mimics the *trans*-membrane solubilization mechanism. TX-100 monomers penetrate into the outer monolayer of bilayer and t*rans*-membrane equilibration of detergent monomers between the two monolayers results in permeabilization of the membrane that occurs via open vesicular intermediates. Open vesicular intermediates are accompanied by spherical mixed micelles. Upon further addition of detergent the whole bilayer transit into spherical mixed micelles. Different steps of this transition are shown in Figures S1a-d.
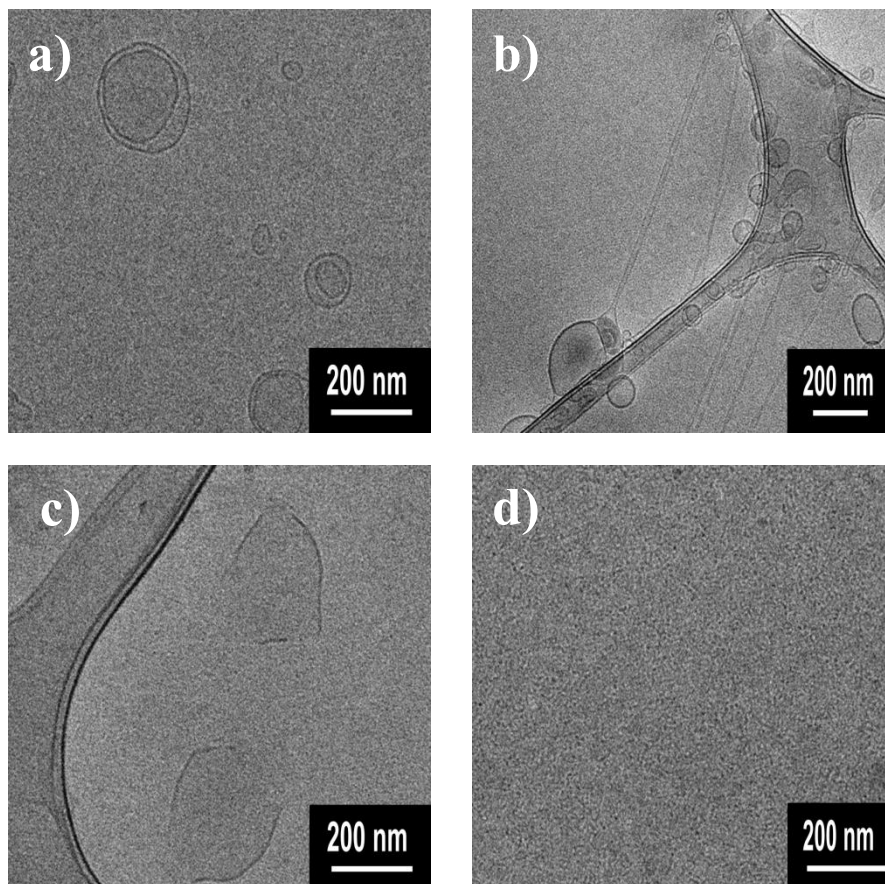
Cryo-TEM micrographs of DPhPC liposomes when treated with TX-100 indicating: (a) detergent incorporation in swelled multilamellar liposomes at $C_{Trit} = 2.5$ mM; (b) solubilization of outer layer of multilamellar liposomes upon addition at $C_{Trit} = 3.6$ mM; (c) open vesicular structures of liposome treated with detergent concentration above R_{sat} ($C_{Trit} = 6.2$ mM), and (d) lipid-TX-100 micelles above R_{sol} ($C_{Trit} = 8.4$ mM).

APPENDIX II

The mixed micelle formation as a result of detergent association (i.e., stage II of the solubilization process with TX-100) is also depicted by stained TEM images, shown in Figures S2a &b for C_{Trit} ~ 1.2 and 1.5 mM respectively, which clearly indicate the onset of mixed micelle formation as a result of the rupturing of detergent-lipid micelles from vesicles.
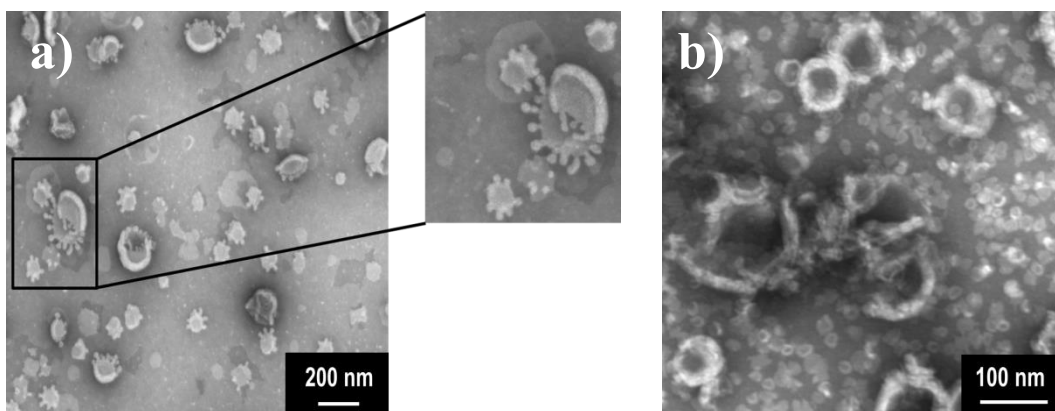
Stained TEM images of DPhPC liposomes when treated with TX-100 indicating: (a) onset of mixed micelle formation at C_{Trit} = 1.2 mM, and (b) increase of micellar structure over vesicular structure at C_{Trit} = 1.5 mM during stage II of the solubilization process.

APPENDIX III

Mixed vesicle-mixed micelle structures with sizes domains ranging from < 20 nm up to > 90 nm are observed in Figure (a) at $C_{DDM} \sim 2.3$ mM, while Figure (b) represents mixed micelle formation upon complete solubilization of liposomes by detergent molecules at $C_{DDM} \sim 7.5$ mM. These observations concur extremely well with our earlier turbidity, DLS as well as cryo-TEM analyses. As also mentioned earlier, it is noted that a few liposome structures are maintained even at the later stage III of the solubilization process.
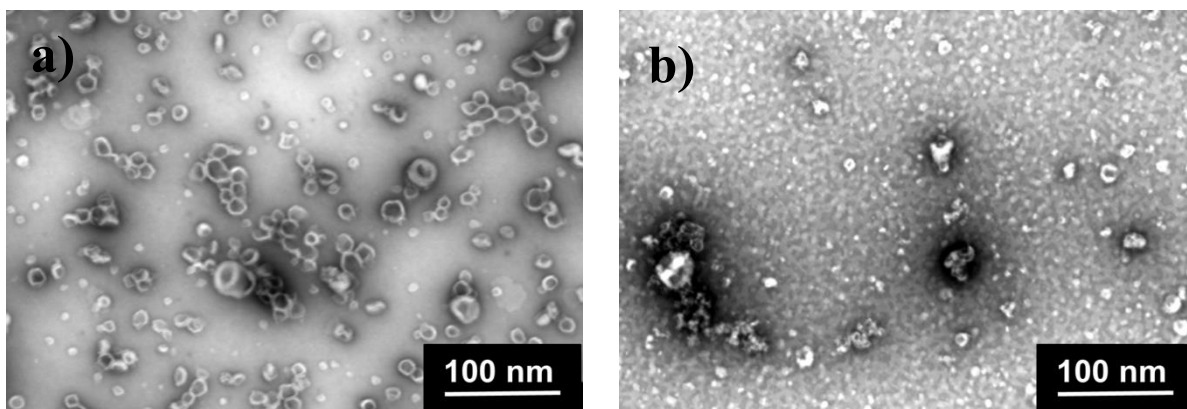
Stained TEM images of DPhPC liposomes when treated with DDM indicating: (a) mixture of DPhPC vesicles and mixed micelles at $C_{DDM} = 2.3$ mM, and (b) mixed micelles formation upon full solubilization of liposomes by detergent molecules during stage III of solubilization process ($C_{DDM} = 7.5$ mM). Some vesicles still remain intact in (b).
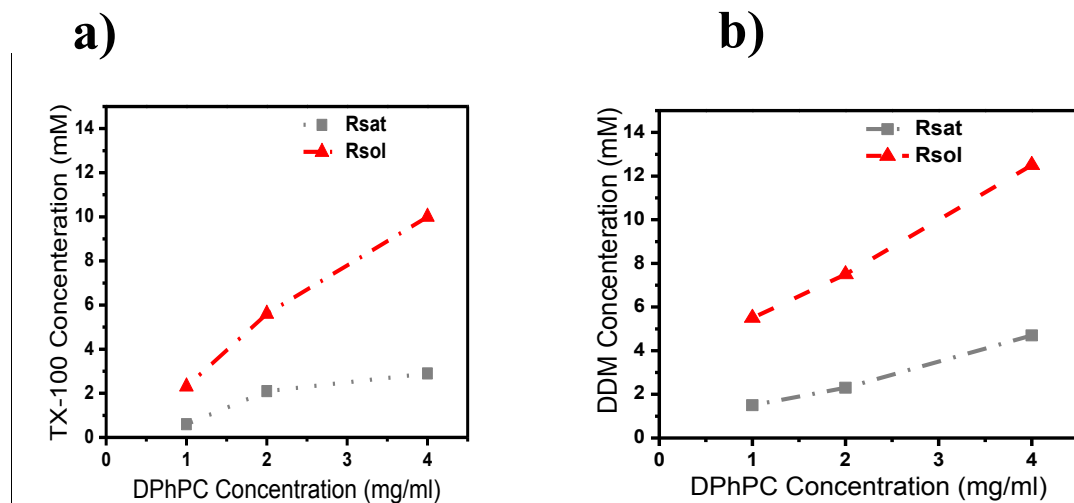
APPENDIX IV

Role of kinetics and/or thermodynamics in the formation of complex structures is investigated via monitoring the structural arrangement above and below the transition temperature of DPPG. DLS data and cryo-TEM images show micron-size structure found at 25°C that turn intosmaller structures (17 – 210 nm) at 50°C.
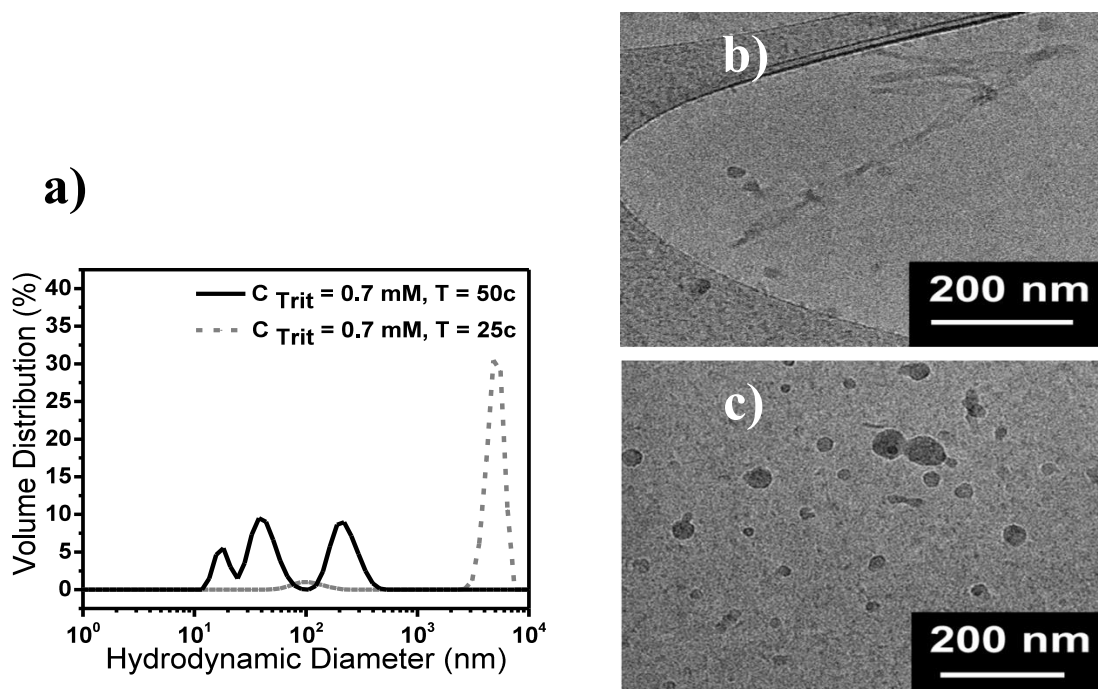
The effect of temperature-change on the morphological arrangement of DPPG/TX-100 mixture at C_{Trit} =0.7 mM, represented by: (a) number distribution (%) from dynamic light scattering measurements at 25°C and 50°C; and cryo-TEM micrographs indicating: (b) twisted dendritic structures at 25°C, (c) packed vesicles and mixed micelles at 50°C.

APPENDIX V

DDM-destabilized DPhPC liposomes provide wider detergent concentration range over stage II for protein insertion than the DPhPC/TX-100 system. Such effects are also observed for solubilizations with different lipid concentrations.

Dependence of R_{sat} and R_{sol} on the choice of detergent and lipid concentration as observed with turbidity measurements optimized for liposome adsorption at 540 nm on: (a) DPhPC/TX-100 mixture and, (b) DPhPC/DDM mixture.

APPENDIX VI

Monitoring TX100-mediated solubilization of DPhPG with isothermal titration calorimetry (ITC).

TX100-mediated solubilization of DPhPG was monitored by following the protocol pioneered by Heerklotz et al.[178] The detailed procedure is as follow:

For the first solubilization experiment, the 1 mM lipid suspension and the 77 mM detergent solution were brought to a temperature slightly below the desired experimental temperature (23–24 °C) and degassed by stirring the open vials under reduced pressure for ~10 min. The calorimeter cell was filled with the lipid suspension and the syringe with the detergent solution. The net volumes are ~1.4 ml for the cell and ~300 μl for the syringe. In the driver software of the calorimeter, the experimental parameters such as temperature, concentrations, stirring speed, reference power, feedback mode, number of injections, injection volumes, injection speeds, spacings, etc were specified. **35 injections were performed with spacing of 30-40 minutes. A sequence 5 × 2.0, 1.5, 1.5, 2.0, 2.0, 3.0, 3.0, 4.0, 8.0, 5.0, 6.0, 7.0, 7.0, 5.6, 8.3, 8.9, 9.7, 10.5, 11.3, 12.3, 13.3, 14.3, 14.3, 15.0, 15.0, 15.0, 16.5, 20.0, 20.0, 10.0 and 20.0 μl** volumes **in the course of the titration was used.**

For the second solubilization experiment, the 4 mM lipid suspension and the 154 mM detergent solution were brought to a temperature slightly below the desired experimental temperature (23–24 °C) and degassed by stirring the open vials under reduced pressure for ~10 min. The calorimeter cell was filled with the lipid suspension and the syringe with the detergent solution. The net volumes are ~1.4 ml for the cell and ~300 μl for the syringe. **41 injections were performed with spacing of 30-40 minutes. A sequence 2.0, 4 × 3.0, 4.0, 2.0, 3.0, 3.0, 2.0, 4 × 4.0, 2.0, 3.0, 4.0, 3.0, 4.0, 3 × 3.0, 7.0, 4.0, 5.0, 5.0, 6.0, 4.0, 6.0, 4.0, 7.0, 6.0, 5.0, 7.0, 13.0, 10.0, 20.0, 22.0, 25.0, 25.0, 30.0 μl** volumes **in the course of the titration was used.**

APPENDIX VII

Phase diagram explanation.

The phase diagram is established based on two series of solubilization experiments starting at different lipid concentrations (1 mg ml^{-1} and 4 mg ml^{-1}).

As the phase boundaries obey, in the ideal case, linear fits of the two boundaries based on the equations

$$C_D^{SAT}(C_L) = R_e^{SAT} C_L + C_D^{aq,SAT} = R_e^{SAT}(C_L + \frac{1}{KR}) \tag{1}$$

and

$$C_D^{SOL}(C_L) = R_e^{SOL} C_L + C_D^{aq,SOL} = R_e^{SOL}(C_L + \frac{CMC}{1+ReSOL}) \tag{2}$$

would provide the maximal detergent-to-lipid mole ration in membranes (onset of solubilization), R_e^{SAT}, the minimal detergent-to-lipid mole ratio in micelles (completion of solubilization), R_e^{SOL} and the free detergent concentration on solubilization.

Intercept of the linear fits of the two boundaries give

$$C_D^{SAT}(C_L) = 0.67 C_L + 1.05$$

and

$$C_D^{SOL}(C_L) = 3.17 C_L + 1.05$$

where $C_D^{aq,SAT} = C_D^{aq,SOL} = 1.05$ mM, the CMC of the pure TX-100 is 1.38 mM and the membrane–water partition coefficient (K_R) is 0.64 mM^{-1}.

VITA

Seyedeh Hanieh Niroomand was born in Shiraz, Iran in 1985 to Zahra MohammadiZadeh and Seyed AhmadReza Niroomand. In 2008, she received her Bachelor of Science degree in chemical engineering from Shiraz University, Shiraz, Iran. Later, she attended the University of Tennessee, Department of Chemical and Biomolecular Engineering and joined Prof. Bamin Khomami's research group in 2009 to pursue her doctoral degree in chemical engineering. Her doctoral research has mainly focused on utilizing the cyanobacterial Photosystem I (PSI) for integration into organic/inorganic interfaces that mediate photo-electrochemical energy conversions for electricity and/or solar fuel production. Her doctoral research work has resulted in five published and submitted papers. She also received her M.Sc. in chemical engineering in 2013.